Aalborg University Esbjerg

Master Thesis

10-09-14

Master Thesis

Modeling of nonlinear structural response from explosion loads on offshore structures

By Bjarke Bendiksen

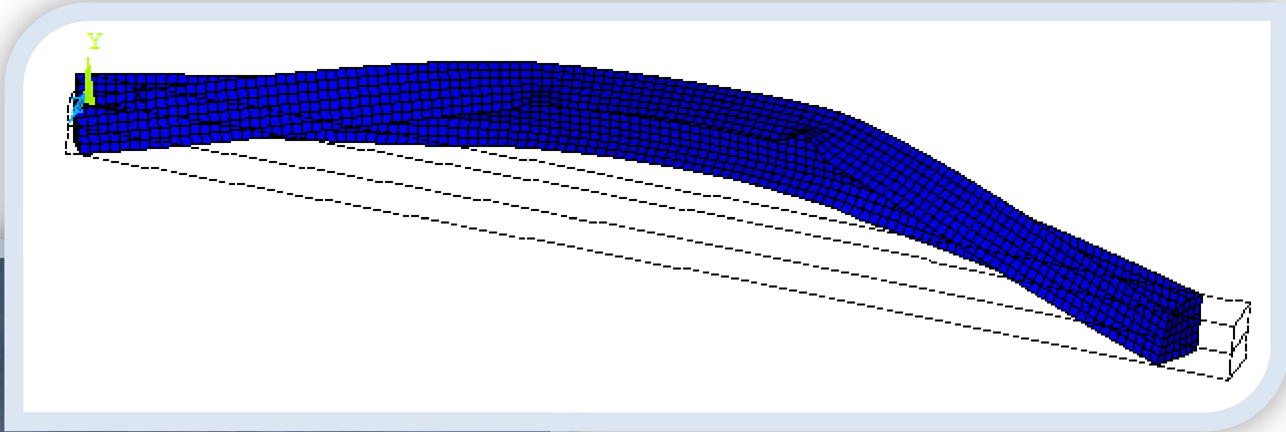

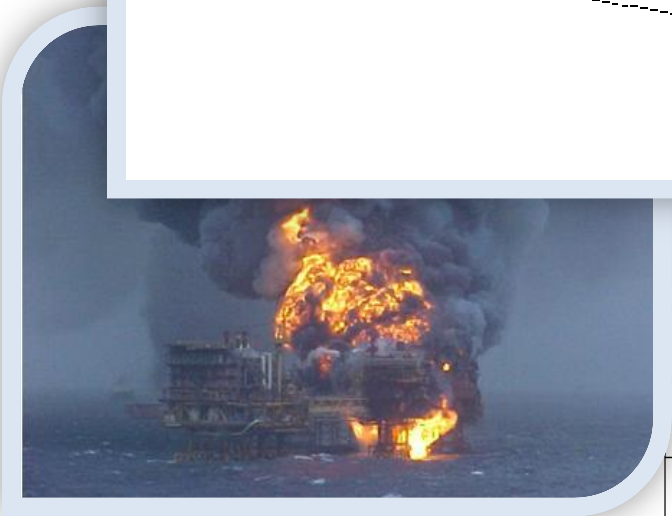

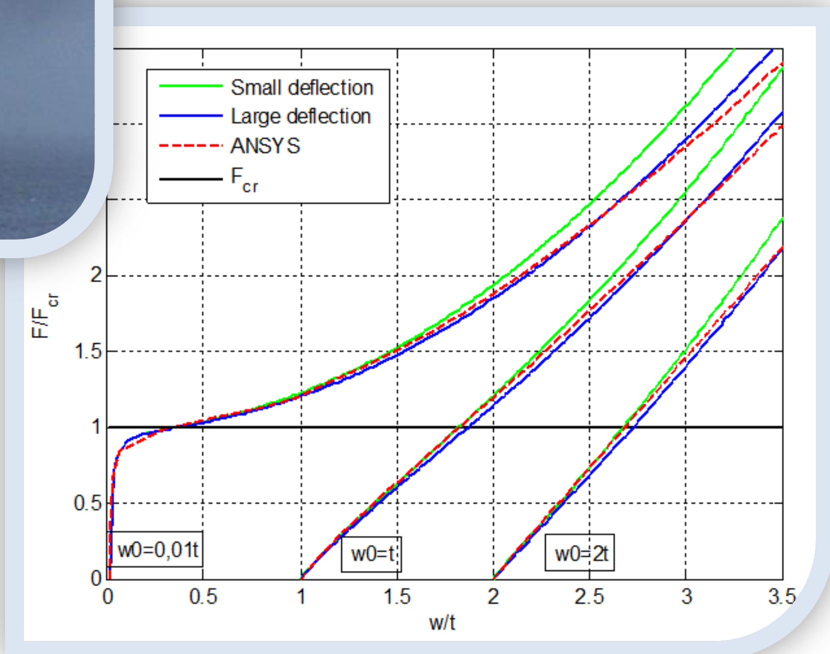

Title sheet

Theme:	Modeling of nonlinear structural response from explosion loads on offshore structures.
Title:	Master Thesis
Period:	02.03.14 – 10.09.14
University:	Aalborg University campus Esbjerg, Denmark
Department:	Civil Engineering
Faculty:	Structural and Civil Engineering
Author:	Bjarke Bendiksen
Supervisors:	**Lars Damkilde** **–** Aalborg University campus Esbjerg **Ulf Tyge Tygesen** **–** Ramboll Oil & Gas Esbjerg
Page count:	77
No. printed copies:	3

Writer

Bjarke Bendiksen

Synopsis

This master thesis investigates the structural response of an offshore module subjected to explosion loads with focus on material- and geometric nonlinearities.

The mechanical behavior of an offshore module under explosion loads is evaluated and representative models are proposed.

The process of modeling full nonlinear dynamics models with the Finite Element software ANSYS, and its subset ANSYS LS-DYNA, is presented and verified. It is found that the inclusion of nonlinearities is essential, as the maximum response of the models is greatly increased.

Strain rate effects are included, using the recommended Cowper-Symonds model, to examine how much structural strength there is to be gained from the effects. It was found that strain rate effects greatly reduce the effects of plasticity, particularly for the full nonlinear model, where the response is almost halved at higher loads.

Local strains in ANSYS and norms are compared. ANSYS results are found to be the least conservative as it has the lowest plastic strains. A convergence method for plastic strain in shell elements was investigated and found to be unreliable.

Various semi analytical methods for modeling post buckling behavior of flat plates are reviewed and it is determined that they match ANSYS results up to two times the critical load. Methods for dynamic buckling are also reviewed and are found to have similar levels of accuracy.

PREFACE

This master thesis has been submitted as part of the M.sc. in Structural and Civil Engineering at Aalborg University Esbjerg.

Gratitude goes towards project supervisor Lars Damkilde (Aalborg University Esbjerg) for supervision and guidance during the project. Gratitude is also given to Ulf Tyge Tygesen (Ramboll Oil & Gas Esbjerg) for providing information and material on the subject matter in the offshore industry.

The thesis assumes that the reader has basic knowledge on the Finite Element method, instability, plasticity and structural dynamics. It is primarily intended to engineers working within the offshore industry, as well as researchers and students seeking to research the subject matter further.

Throughout the report equation numbers are stated as e.g. (1.1) directly after the equations. Its first number refers to the chapter number and second number is the equation number in the chapter. In the text references are then made by inserting the relevant equation number.

At the end of the report a list of references is provided. Throughout the report references is given to this list by numbering [Lxx] or [Wxx] which refers to the corresponding number in the table of references.

The attached DVD includes the thesis in PDF format as well as the following:

ANSYS files:

- APDL scripts:
  - Nonlinear static model of I-profile
  - Nonlinear dynamic model of I-profile
  - Nonlinear static model of plate (displacement controlled analysis)
  - Nonlinear static model of plate (force controlled analysis)
- Workbench projects
  - Nonlinear dynamic model of I-profile with strain rate effects (LS-DYNA)

Table of content

1 INTRODUCTION

When designing offshore platforms, there are a number of accidental loads that can occur. These include ship impacts, dropped objects, fire and explosions. Among these, explosions, as illustrated on Figure 1-1, are particularly challenging, because there are many complexities involved in the design process.

Figure 1-1: Gas explosion on an offshore platform [W1]

Among these complexities are the large load levels, which are likely to induce plasticity in the platform, and thus create permanent deformations. Additionally the load levels can create instabilities in the shape of lateral- or local buckling.

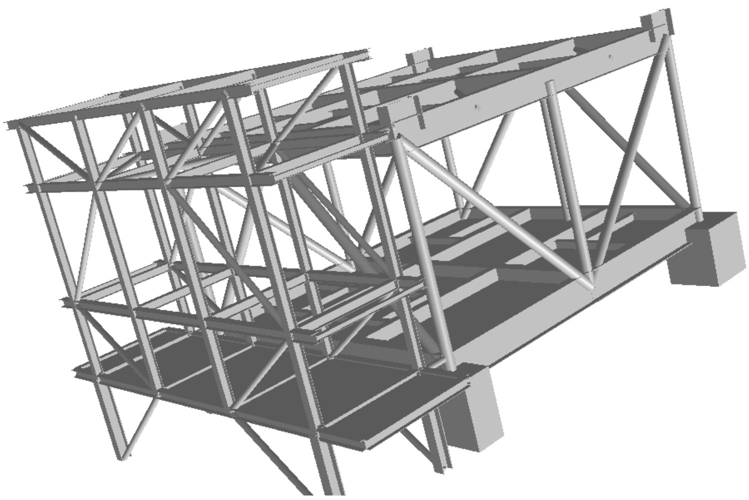

Figure 1-2: Model of a typical Offshore Module in the program ROSAP

An explosion typically has a duration time of less than a second, meaning that the loading is very time dependent, so structural dynamics is essential in modeling an explosion load. This also includes strain rate effects which influence the strength of the structure.

Outside of the structural analysis, there is also the modeling and prediction of the explosion itself, which is a fluid dynamics problem. This includes prediction of the load level, distribution and duration time, as well as the temperature differences.

In the offshore industry it is common to, instead of a full nonlinear FEM model, use simpler variants with mainly beam elements to reduce design time as depicted on Figure 1-2. These beam element formulations do not include the ability to model post buckling behavior when local buckling occurs, so they are forced to consider the element capacity to be empty when they reach the critical load. Similarly, plate formulations face the same problems. Because of this, there is interest in producing methods to model the post buckling state that does not include a full scale FEM model.

Beside insufficient post buckling formulations, there is also interest in ensuring accurate rupture models, including the development of plastic strain and determining the ultimate plastic strain.

1.1 Previous work

Previous work on the subject of explosion analysis includes a Master Thesis done by Hans Jákup Hansen, where the simulation of gas explosions and the resulting structural response is investigated [L11]. These methods are then compared with full scale experiments on an offshore module. Here the author highlights the necessity of a nonlinear structural model, and suggests the implementation of strain rates and rupture models as further work.

Ramboll Oil&Gas Esbjerg has also conducted two studies where the modeling of plastic strain [L13] and strain rate effects [L14] are investigated, respectively.

1.2 Available software

1.2.1 ANSYS

ANSYS is a general purpose Finite Element software which can do static and dynamic analyses as well as modal and linear buckling analyses. It covers the whole process from creation of the geometry to post processing of the results.

1.2.2 LS-DYNA

ANSYS has a subset called ANSYS LS-DYNA where the explicit solver LS-DYNA is integrated into the ANSYS package.

LS-DYNA is an advanced Finite Element package software which specializes in highly nonlinear transient analyses using an explicit solver.

1.2.3 Key differences

The main difference is that ANSYS uses an implicit solver, while LS-DYNA uses an explicit solver.

The implicit time integration is unconditionally stable as long as proper integration parameters are chosen. To get an accurate analysis, sufficiently small time steps are needed, but stability is not at risk.

The explicit time integration is potentially faster since it requires fewer matrix operations per time step, but its explicit nature makes it only conditionally stable with a critical time step size defined as:

$$\Delta t = \frac{2}{\omega_{max}} \tag{1-1}$$

Where ω_{max} is the highest natural frequency in the model.

This critical time step size results in the explicit solver generally requiring many more time steps than the implicit solver.

An additional difference is that ANSYS can perform both static and transient analyses, while LS-DYNA is restricted to transient analyses only.

1.3 Primary effects

The primary effects focused on and investigated in this thesis, beside standard linear elasticity, are:

- Dynamic load and response
- Geometric nonlinearity
- Plasticity
- Strain rate effects

Other potentially important effects, not included in this thesis, are temperature differences and their influence on the material behavior as well as the contact problem of structural interaction where different parts of a larger structure hit each other.

As this thesis focuses on the structural response, effects related to the modeling of the explosion itself such as the exact load distribution and load interaction where the structural response changes the fluid behavior of the explosion and vice versa.

Nonlinearities are often tackled by applying loads in increments as the nonlinear behavior is dependent on the load history. Other solution methods include the common Newton-Raphson iteration scheme.

For the standard linear approach, small displacements and strains are assumed and the strength of the structure is dependent only on strength of the undeformed structure. When geometric nonlinearities, often also called large deflection theory, are included, the structural strength is updated for each load increment to reflect the change in stiffness because of the deformations.

One important phenomenon that can be modeled through geometric nonlinearity is stress stiffening, where membrane forces causes by the deformations increase the stiffness of the structure.

Another phenomenon, which is one of the primary focuses of this thesis, is instability, where a small increase in load cause a large increase in deformation. Instability occurs when the specimen is subjected to compressive forces, and these forces reach a critical load. Instability is often accompanied by a softening effect which, in contrast to stress stiffening, is a result of the structural integrity weakening in the new deformed state.

Plasticity is a nonlinear material behavior that occurs when the structure starts to yield. When plasticity occur the deformations and strains increase drastically until the material ruptures, with Figure 1-3 showing the stress strain curve for typical structural steel. For materials like concrete, the plasticity region (the region from first yield to rupture) is so small it is negligible, while for metals like structural steel the region is fairly large and simply setting first yield as maximum bearing capacity equals ignoring a significant part of the bearing capacity.

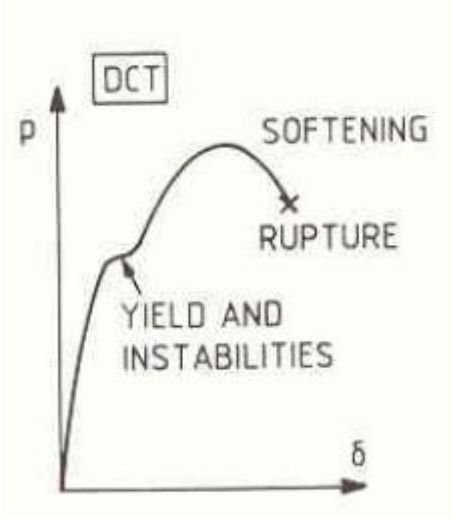

Figure 1-3: Typical stress strain curve of structural steel [L11]

Unlike elastic deformation, plastic deformations (and the subsequent plastic strains) are permanent.

1.4 Objective of Thesis

This thesis will focus purely on the structural response aspect of the analysis, where the explosions loads will be borrowed from previous analyses that are representative of a typical offshore module.

The objective of this thesis is threefold: Investigation of strain rate effects on nonlinear dynamic models, investigation of rupture models in beams and testing analytical solutions for modeling static and dynamic buckling.

For this purpose 2 representative simple models will be developed in ANSYS. The models will consist of an I-profile and a rectangular plate.

The strain rate effects will be examined by testing nonlinear dynamic models of the I-profile and documenting the impact when the strain rate effects are included.

Rupture models will be looked into by investigating the development of plastic strain in the I-profile and holding it up against methods in standards. Here, the aim is to test the assumptions in standards, and how they compare to ANSYS results.

Simplified solutions for modeling buckling will be tested by comparing the deflection response with the results given by the ANSYS models.

1.5 Structure of report

The report consists of two parts. The first part is the modeling of the structures on ANSYS, were models relevant for examining plasticity and instability are introduced, modeled in ANSYS and verified to ensure accurate results. Additionally a study of the strain rate effects in ANSYS models is included in this part. The ANSYS modeling part includes Chapter 2-5.

The second part consists of taking known simplified results from norms and research papers and comparing them with the numerical results. This spans development of plastic strains and local buckling of flat plates. It includes Chapter 6-7.

The structure of the report is as follows:

Chapter 2: Introduction of the representative models and the load profiles of the explosion load.

Chapter 3-4: Documentation and verification of the FEM models.

Chapter 5: Investigation of the impact of strain rate effects on I-profile model.

Chapter 6: Investigation of the development of plastic strain in I-profile model.

Chapter 7: Comparison of the FEM plate model with analytical methods for describing the instability.

Chapter 8: Concluding remarks on the project findings, and suggestions for further work beyond that of this project.

2 MODEL SETUPS

The thesis will focus on two models, a beam and a plate. As mentioned in Chapter 1, the offshore industry faces challenges when they model individual beam and plate elements. While formulations for both types exist, there are several phenomena that they cannot simulate. Most notable is instabilities such as local buckling which therefore require a complex Finite Element model in order to obtain sufficient results. Additionally, while current beam formulation can simulate plasticity and plastic strain, these formulations include a series of assumptions that may not make them as accurate as a Finite Element model.

Because of these limitations, there is interest in comparing the existing approaches within instability and plasticity to a complex Finite Element model. Said Finite Element models will thus be individual beam and plate model so they can be compared directly to existing methods.

Chosen models are a beam and a plate that are representative of the typical boundary conditions on an offshore module. Specifically, models where stability can occur because of compressive forces are chosen.

Both models share the same material properties, so these will be covered here. The properties chosen are standard for steel structures in the North Sea, and are all listed in Table 2-2.

The shear modulus is calculated based on the Young's modulus and the Poisson's ratio through the following expression:

$$G = \frac{E}{2(1+\nu)} \tag{2-1}$$

For plasticity a bilinear isotropic hardening model is used with yield strength of 355MPa. The hardening parameter is chosen according to the recommendation for accidental loads from DNV-RP-C204 as shown in Table 2-1.

Table 3-4 Proposed values for ε_{cr} and H for different steel grades

Steel grade	ε_{cr}	*H*
S 235	20 %	0.0022
S 355	15 %	0.0034
S 460	10 %	0.0034

Table 2-1: Table from DNV-RP-C204 [L7]

Where the relation between the hardening parameter H, and the tangential modulus is given by:

$$H = \frac{E_t}{E} \Leftrightarrow E_t = H \cdot E \tag{2-2}$$

The material parameters used in this thesis is thus as listed in Table 2-2.

Description	Symbol	Unit	Value
Young's Modulus	E	MPa	210000
Poisson's ratio	ν	-	0.3
Shear Modulus	G	MPa	80770
Density	ρ	$\frac{kg}{m^3}$	7850
Yield strength	f_y	MPa	355
Tangent Modulus	E_t	MPa	714

Table 2-2: Table of material properties

This gives a material model curve as shown on Figure 2-1.

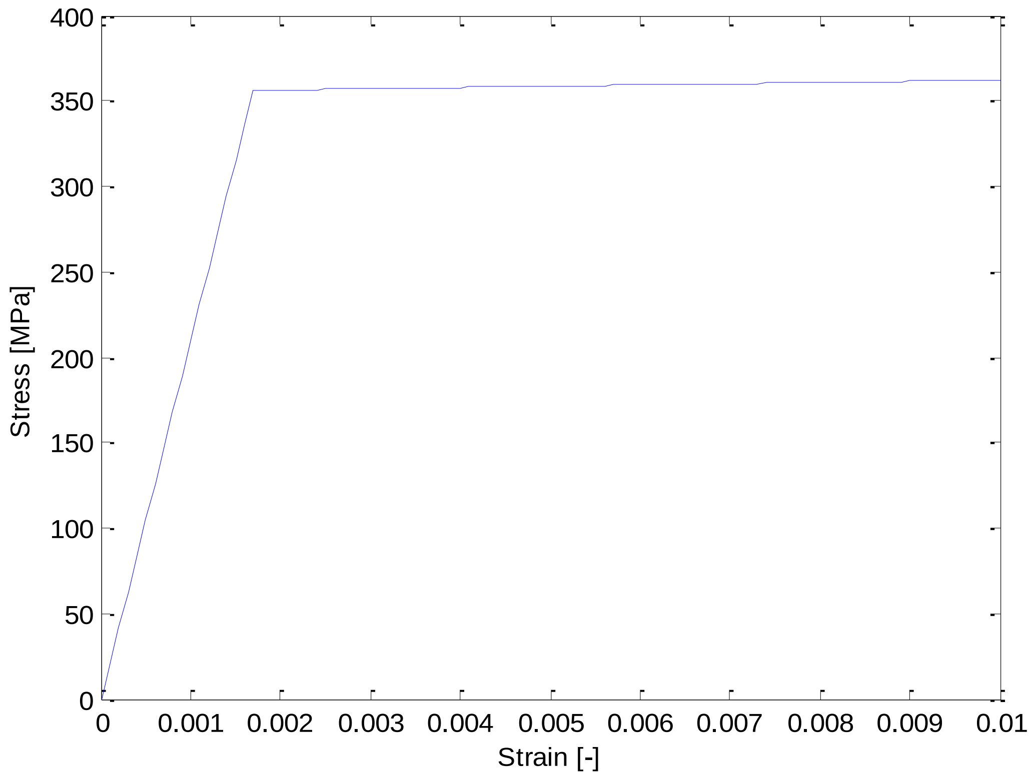

Figure 2-1: Material model.

2.1 Beam

The beam model is chosen based on the I-profiles carrying the plates exposed to the explosion load, as illustrated in Figure 2-2. A uniformly distributed explosion pressure is assumed, with the beam taking half the pressure from each plate section.

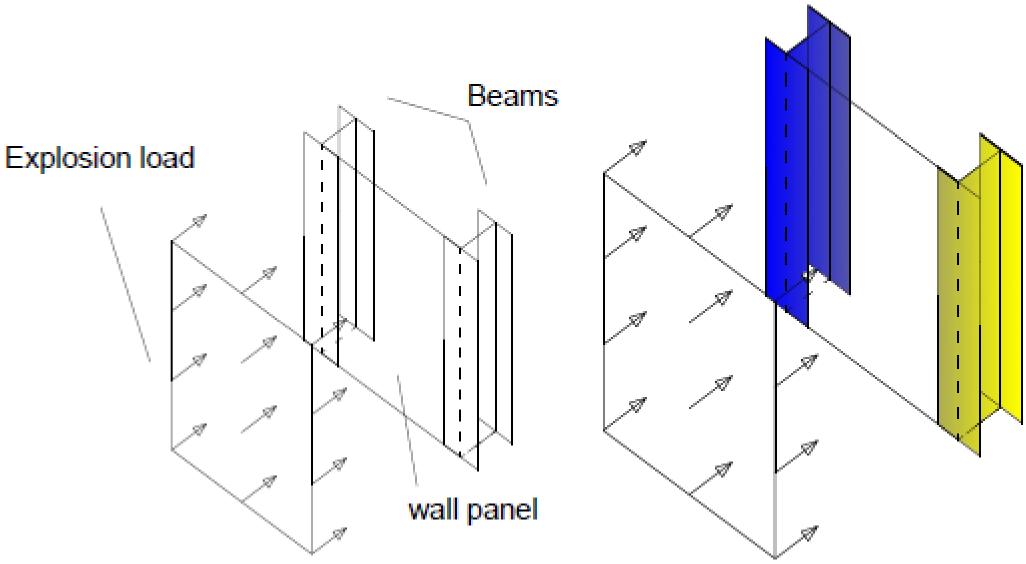

Figure 2-2: Left: Sketch of the context of the beams. Right: Highlight of the beams.

This gives a static system for the individual plates that can be simplified to a simply supported beam with a uniformly distributed load, as shown in Figure 2-3.

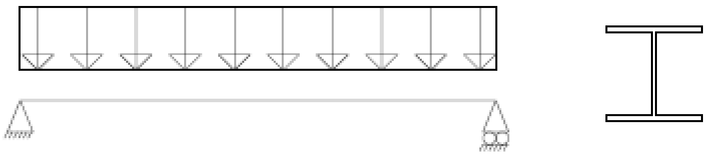

Figure 2-3: Boundary conditions and cross section of beam model

2.1.1 Computation of basic structural information for beam model

The chosen geometry of the cross section is listed in Table 2-3, and is based on the profiles typically used in offshore modules.

Description	Symbol	Value
Web thickness	t_{web}	10
Web height	h_{web}	270
Flange thickness	t_{flange}	15
Width	b	300
Total height	h_{tot}	300

Table 2-3: Cross sectional geometry parameters. Everything is in mm.

General cross sectional parameters will be computed in this chapter for use in later chapters.

The cross sectional area is:

$$A_c = 2t_f b + t_{web} h_{web} \tag{2-3}$$

The second moment of inertia around y-axis (strong axis) is:

$$I_y = \frac{1}{12} t_{web} h_{web}{}^3 + \frac{1}{6} b t_{flange}{}^3 + 2t_{flange} b \left(\frac{h_{tot}}{2} - \frac{t_{flange}}{2}\right)^2 \tag{2-4}$$

The torsional moment of inertia is given by:

$$I_v = \frac{2}{3} t_{flange}{}^3 b + \frac{1}{3} t_{web}{}^3 h_{web} \tag{2-5}$$

For the inertial moments regarding the weak axis, the second moment of area of the flange is introduced:

$$I_f = \frac{1}{12} t_{flange} b^3 \tag{2-6}$$

With this the second moment of inertia around z-axis (weak axis) can be found by:

$$I_z = 2I_f \tag{2-7}$$

And the warping moment of inertia by:

$$I_w = 2I_f \left(\frac{h_{web} + t_{flange}}{2} \right)^2 \tag{2-8}$$

Finally, the section modulus for both the elastic and plastic case is computed.

Elastic:

$$W_{el} = \frac{I_y}{z} = \frac{I_y}{\frac{h_{tot}}{2}} \tag{2-9}$$

Plastic:

$$W_{pl} = b t_{flange} \left(h_{tot} - t_{flange} \right) + 0.25 t_{web} h_{web}{}^2 \tag{2-10}$$

The results are given in Table 2-4.

Description	Symbol	Unit	Value
Area	A	mm^2	$1.17 \cdot 10^4$
Second moment of area around y-axis	I_y	mm^4	$1.99 \cdot 10^8$
Second moment of area around z-axis	I_z	mm^4	$6.75 \cdot 10^7$
Torsional moment of inertia	I_v	mm^4	$7.65 \cdot 10^5$
Warping moment of inertia	I_w	mm^6	$1.37 \cdot 10^{12}$
Elastic section modulus	W_{el}	mm^3	$1.33 \cdot 10^6$
Plastic section modulus	W_{pl}	mm^3	$1.47 \cdot 10^6$

Table 2-4: Cross sectional parameters

2.2 Plate

Following up on the system sketched in Figure 2-2, plates in the offshore module can be exposed to compressive forces from the beams and panels as sketched in Figure 2-4.

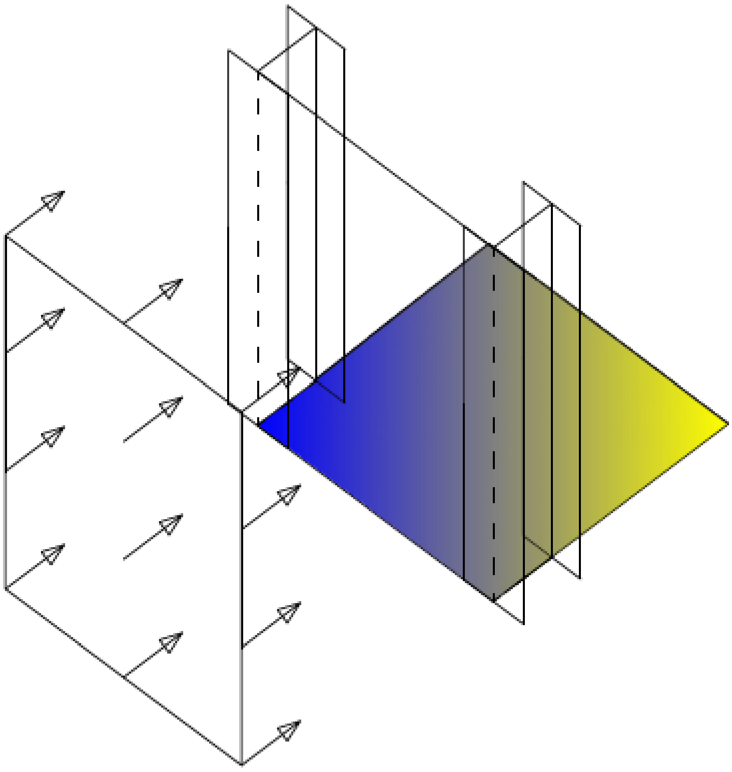

Figure 2-4: Sketch of the context of the plate model. Plate is the highlighted part.

From this context a representative model with the loads being compressive forces as sketched in Figure 2-5 is chosen the project. Technically, shear forces are also involved, but this project focuses on the case of pure compression.

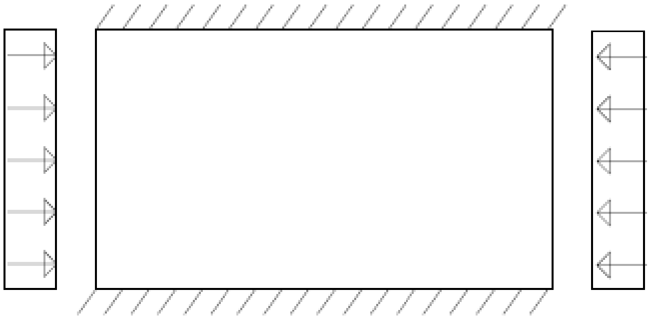

Figure 2-5: Boundary conditions of plate model

Plate geometry is as shown in Table 2-5.

Description	Symbol	Value
Plate thickness	t_p	10
Plate width	a	2000
Plate height	b	1000

Table 2-5: Plate geometry. Everything is in mm.

2.2.1 Computation of basic structural information for plate model

Unlike the beam model, the plate only has one relevant structural constant for analytical solutions. That is the flexural rigidity which determines the plate's resistance to bending out of plane, and it's given by:

$$D = \frac{Et^3}{12(1-\nu^2)} = \frac{210000MPa \cdot (10mm)^3}{12 \cdot (1-0.3^2)} = 1.923 \cdot 10^7 Nmm = 19.23kNm \tag{2-11}$$

2.3 Loading

An explosion is an impulse load that is characterized by a high peak pressure and a short duration time (less than a second). Usually a Computational Fluids Dynamics (CFD) tool is used to simulate the explosion, including its movement in the 3D space, variation over time and peak pressure levels. As a CFD simulation is an extensive task in itself, and is sensitive to variations in the initial parameters according to [L11], the load will just be estimated based on representative values for explosion loads on offshore modules.

In reality the pressure distribution will be uneven, but for this project it will be assumed to be uniformly distributed.

The load-time curve is actually uneven, but this project will linearize it into a triangular load-time curve as illustrated on Figure 2-6, which is a common approximation used in the industry.

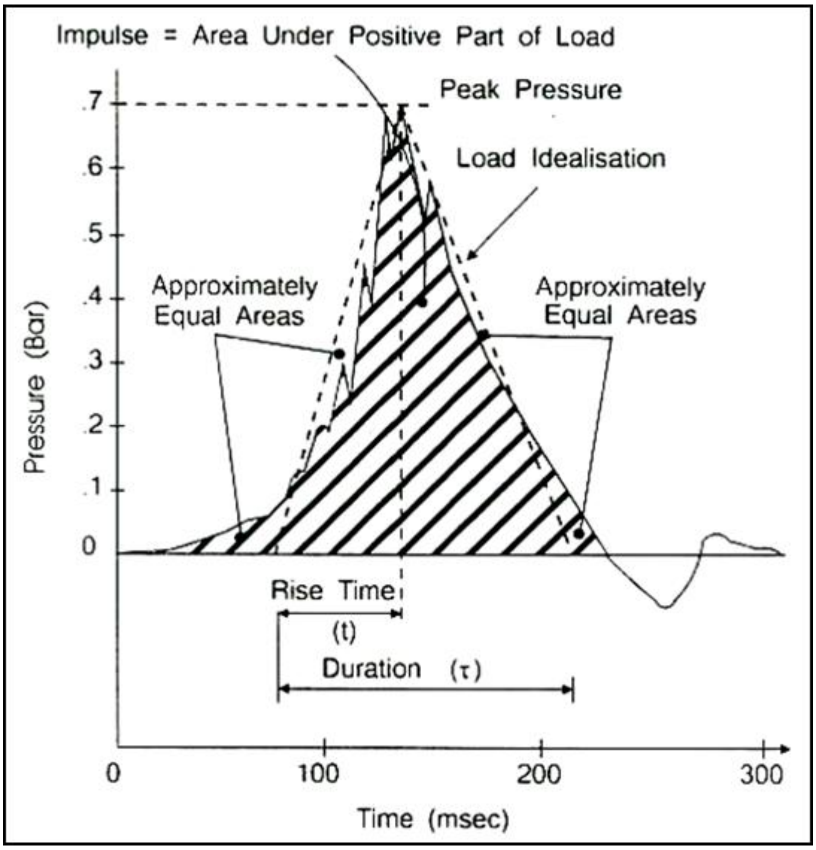

Figure 2-6: Example of a pressure-time curve. The curve is idealized into a triangular shape [L14].

The pressure-time curve used is representative of the load levels occurring during gas explosions on offshore platforms. With a peak pressure of 0.42 MPa and a duration time of 100 miliseconds, the linearized form is illustrated on Figure 2-7.

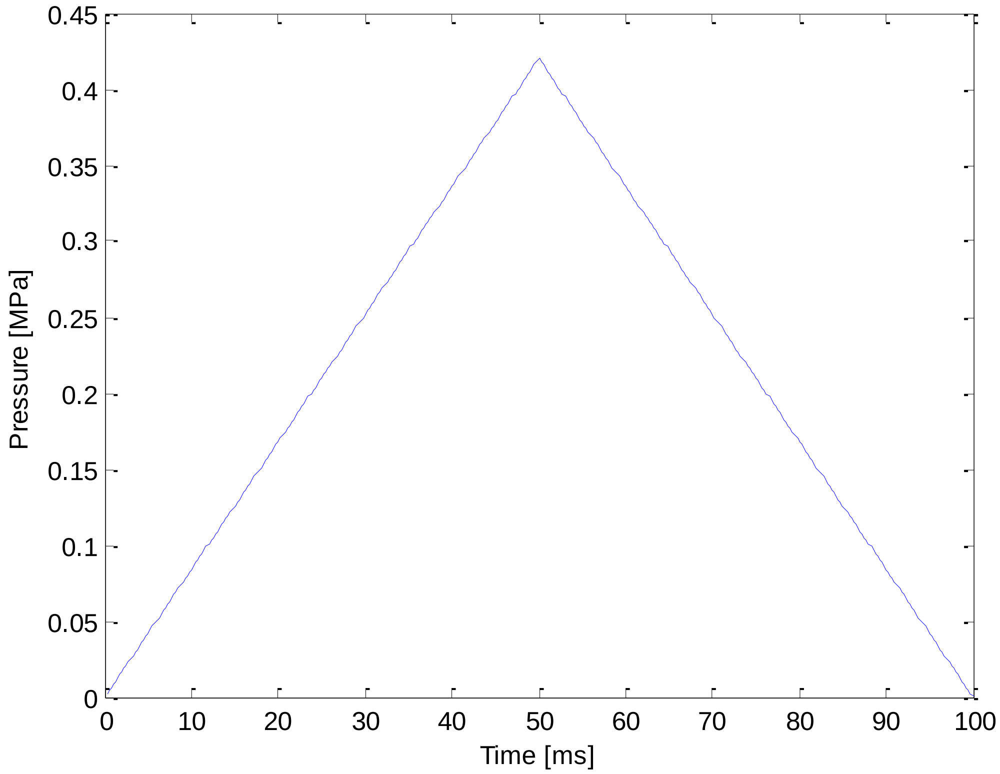

Figure 2-7: Linearized pressure-time curve

The pressure load is chosen as 0.42 MPa because it yields the best results in terms of displaying both plasticity and instability in the chosen model.

The load-time curve for the plate model is more difficult to estimate, as it's only indirectly exposed to the explosion load. Instead, a load level that is sufficient to induce instability will be used. The duration time will still be 100 milliseconds and the load-time curve will be linearized in the same manner as the one in Figure 2-7.

2.4 Partial conclusion

Using recommended values from offshore standards a bilinear isotropic hardening model is chosen to model the nonlinear material behavior when the material starts to yield.

A simple static system for an I-profile that is representative of the loading conditions of an offshore platform is determined. Additionally a plate model with simple boundary conditions that can be assumed to occur on offshore platforms is established. Both models have been chosen so that they are exposed to the compressive forces that can cause instability.

For the time dependent loading, a linearized triangular impulse load has been chosen to approximately model the load profile of an explosive pressure.

3 MODELLING OF INSTABILITIES

3.1 Types of instabilities

Instabilities are characterized by a small increase in load leading to a large increase in deformations. They can occur when a structure is exposed to compressive forces.

The key types investigated in this thesis are lateral- and local buckling. A sketch of lateral buckling of a simply supported beam is depicted in Figure 3-1.

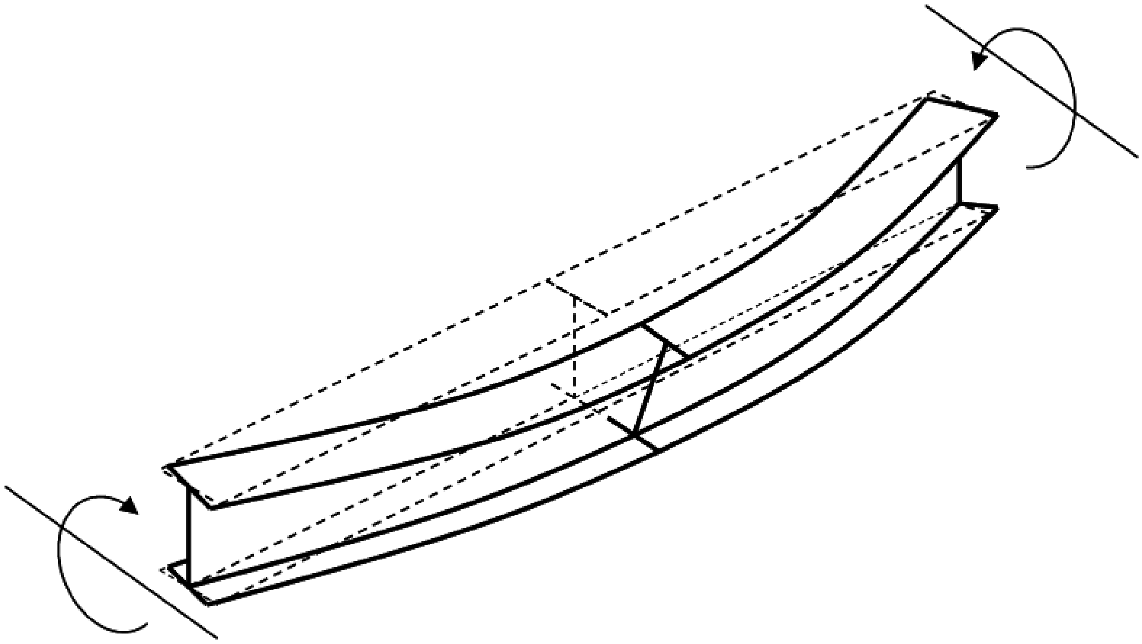

Figure 3-1: Sketch of lateral buckling [W2]

And local buckling in a plate is sketched in Figure 3-2.

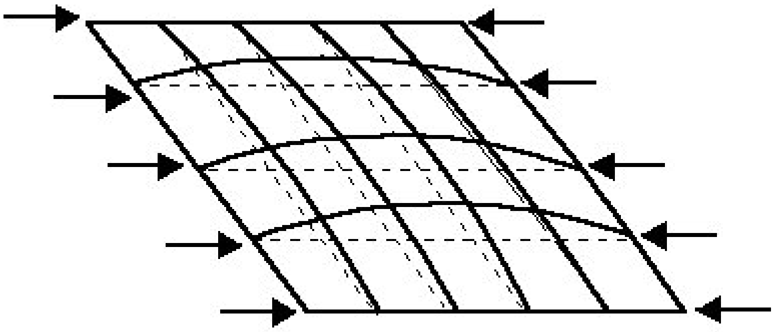

Figure 3-2: Sketch of local plate buckling

This chapter is dedicated to documenting and verifying the static ANSYS models of the I-profile and plate respectively. The documentation for both models is done with focus on their ability to model the instabilities.

3.2 Instability in beam model

3.2.1 Boundary conditions of beam

This subsection will go through the setup of the boundary conditions for the I-profile, coupled with linear elastic analyses.

The I-profile model will be modeled through the use of shell elements, as the structure consists of plates. The elements used will be the SHELL281 elements in ANSYS, which are

8noded shell elements, with 6 degrees of freedom in each node, using Mindlin-Reisner theory. The SHELL281 element is illustrated on Figure 3-3.

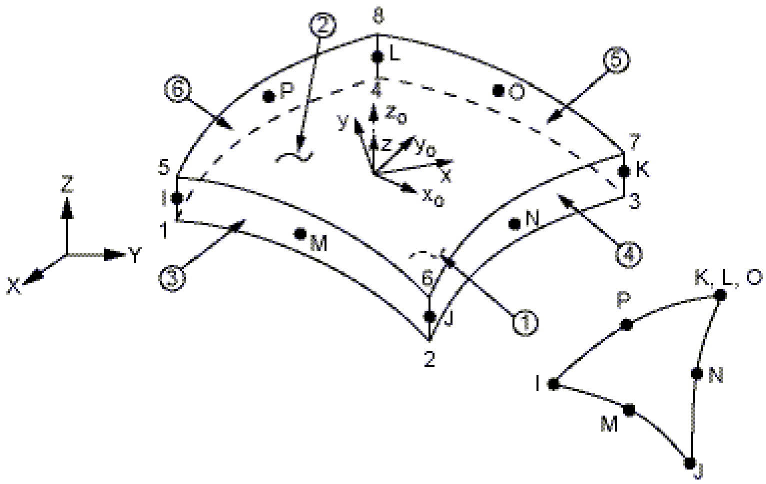

Figure 3-3: The SHELL281 element used in ANSYS [L12]

The simple supports are modeled as nodal supports at the centerline ends. However, including only the nodal supports create stress singularities, so plate stiffeners are included at the ends along with rotational support so that the profile will not simply spin around the beam axis. The placement of these supports are illustrated on Figure 3-4, where the image to the left depicts the theoretical concept of these rotational supports and the image to the right shows the finite element approach.

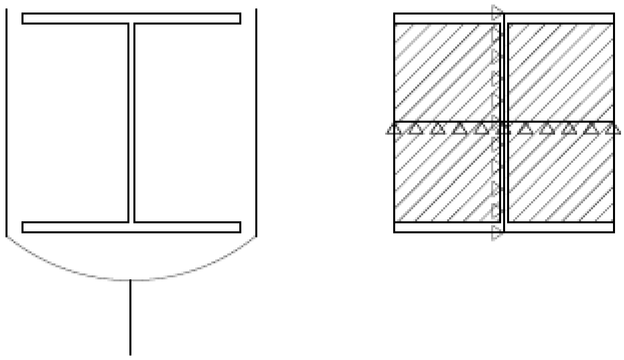

Figure 3-4: Left: Theoretical support. Right: Supports in ANSYS.

Doing a convergence study based on the global deformation an element size of 50mm is found to be sufficient for the I-profile model. This gives the mesh shown in Figure 3-5. Additionally ANSYS results regarding deformations and stresses are found to match closely with hand calculation based on classic Bernoulli-Euler theory.

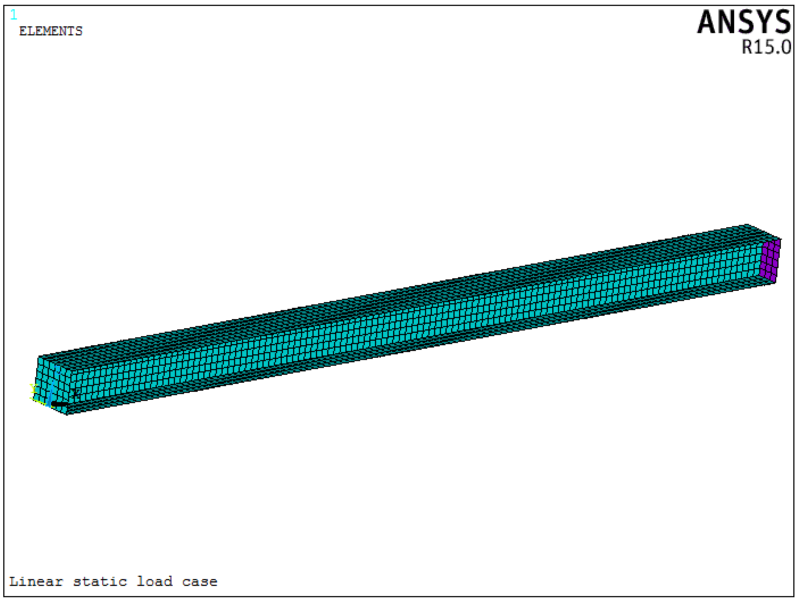

Figure 3-5: Mesh of I-profile.

3.2.2 Buckling analysis of beam

In standards, a common method to determine whether a beam will have local stability problems is through the use of cross section classes. These classes determine whether the capacity of the structure will be impacted by instability before or after yielding occurs, and are explained in detail in Chapter 5.5.2 in [L2].

For comparison the plastic moment capacity is determined, and when it is known, the yield load can be found similarly as shown in the following:

$$M_{pl} = \frac{1}{8} p_Y l^2 \Leftrightarrow p_Y = 8 \frac{M_{pl}}{l^2} = 8 \cdot \frac{520kNm}{(6m)^2} = 115.5 \frac{kN}{m} \tag{3-1}$$

Where $M_{pl} = f_y W_{pl}$

This gives a yield pressure of $115.5 \frac{kN}{m} * \frac{1}{300mm} = 0.385MPa.$

The cross section class will be determined as shown in Figure 3-6.

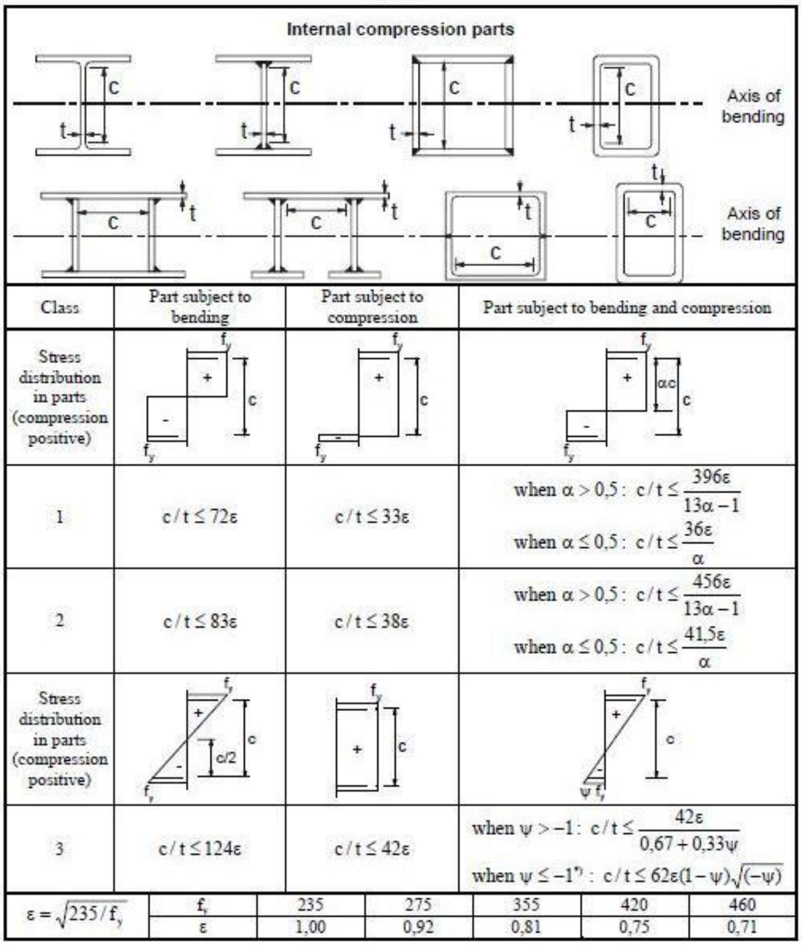

Class	Part subject to bending	Part subject to compression	Part subject to bending and compression
Stress distribution in parts (compression positive)			
1	$c/t \le 72\varepsilon$	$c/t \le 33\varepsilon$	when $\alpha > 0{,}5$: $c/t \le \frac{396\varepsilon}{13\alpha - 1}$ when $\alpha \le 0{,}5$: $c/t \le \frac{36\varepsilon}{\alpha}$
2	$c/t \le 83\varepsilon$	$c/t \le 38\varepsilon$	when $\alpha > 0{,}5$: $c/t \le \frac{456\varepsilon}{13\alpha - 1}$ when $\alpha \le 0{,}5$: $c/t \le \frac{41{,}5\varepsilon}{\alpha}$
Stress distribution in parts (compression positive)			
3	$c/t \le 124\varepsilon$	$c/t \le 42\varepsilon$	when $\psi > -1$: $c/t \le \frac{42\varepsilon}{0{,}67 + 0{,}33\psi}$ when $\psi \le -1^{*)}$: $c/t \le 62\varepsilon(1-\psi)\sqrt{(-\psi)}$

$\varepsilon = \sqrt{235/f_y}$	f_y	235	275	355	420	460
	ε	1,00	0,92	0,81	0,75	0,71

Figure 3-6: Determination of cross section class in Eurocode 1993-1-1 [L2].

The top flange, which is exposed to compressive forces, has a c/t ratio of:

$$\frac{c}{t} = \frac{300mm}{15mm} = 20 < 33\varepsilon = 26.8$$

Where $\varepsilon = \sqrt{\frac{235MPa}{f_y}} = \sqrt{\frac{235MPa}{355MPa}} = 0.81$

The web which is exposed to bending has a c/t ratio of:

$$\frac{c}{t} = \frac{270mm}{10mm} = 27 < 72\varepsilon = 58.5$$

So both the flange and the web is Class 1, and thus shouldn't have local stability problems before yielding. Class 1 means that both plastic stress distribution and resistance is allowed for hand calculations.

However, cross section classes are only a generalized method, and Finite Element results or further hand calculations might tell otherwise.

A linear buckling analysis is performed where, similarly to the modal analysis, mode shapes are found with a corresponding Eigen value. For the linear buckling analysis, the Eigen value is the load factor needed to reach the critical Euler load. This load is the load were buckling will occur if the structure is ideal and without imperfections (i.e. a Euler structure).

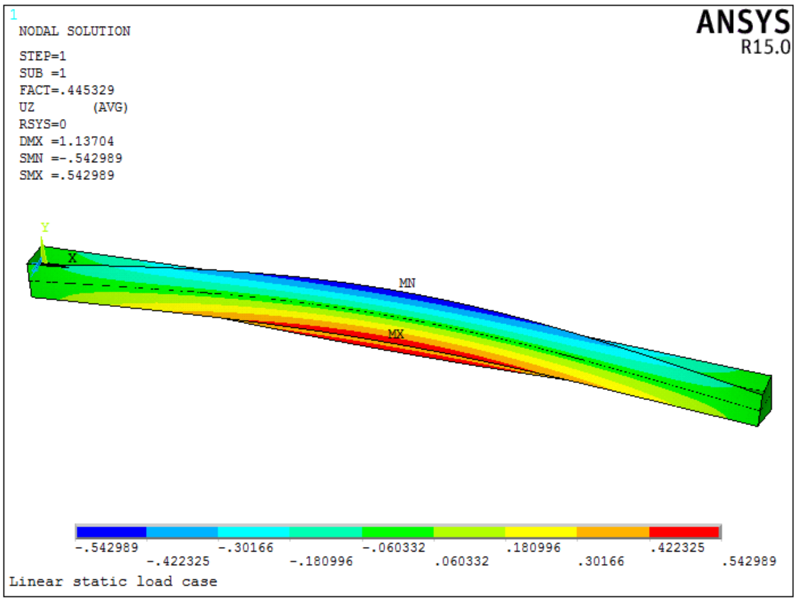

Figure 3-7: 1st buckling mode

The result of the first buckling mode is pictured on Figure 3-7, where it is clear that lateral buckling is the critical instability for this beam, at a pressure of 0.445MPa. The other mode shapes are at much higher loads, and all depict variants of local buckling in the top flange.

To make sure that the model has converged, another convergence study is made in Figure 3-8 based on the critical pressure.

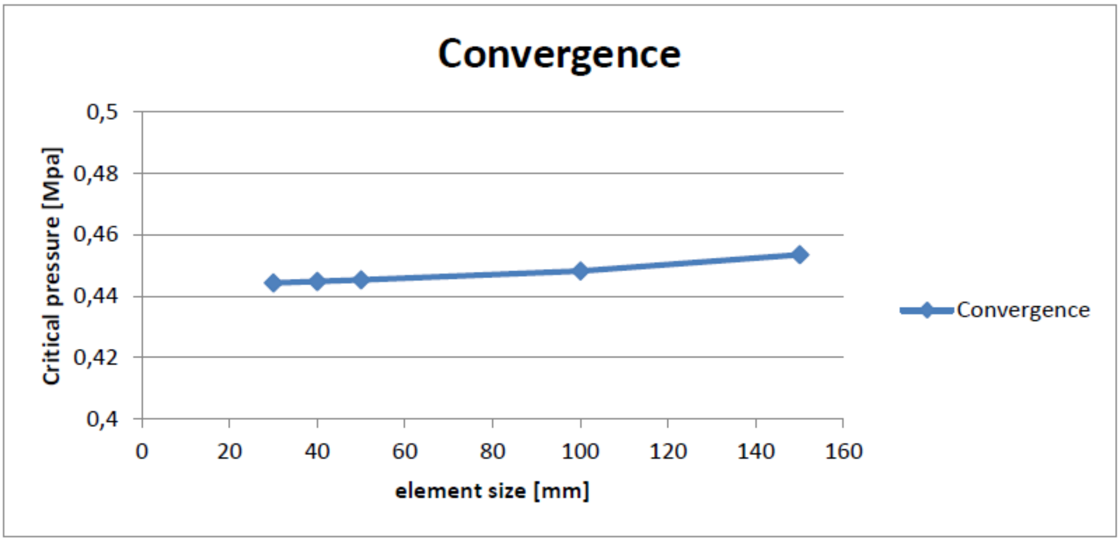

Figure 3-8: Convergence for linear buckling analysis

It is clear that an edge length of 50mm is still sufficient.

As lateral buckling is the critical instability, hand calculations following the standard are made to compare with the ANSYS results. For this, the dimensionless factor 'kl' is needed:

$$kl = \sqrt{\frac{GI_v l}{EI_w}} = 2.7 \tag{3-2}$$

The general approaches is looking at the 8 basic load cases shown in Figure 3-9, and pick the one that is most similar, to the beam that is being examined for lateral buckling.

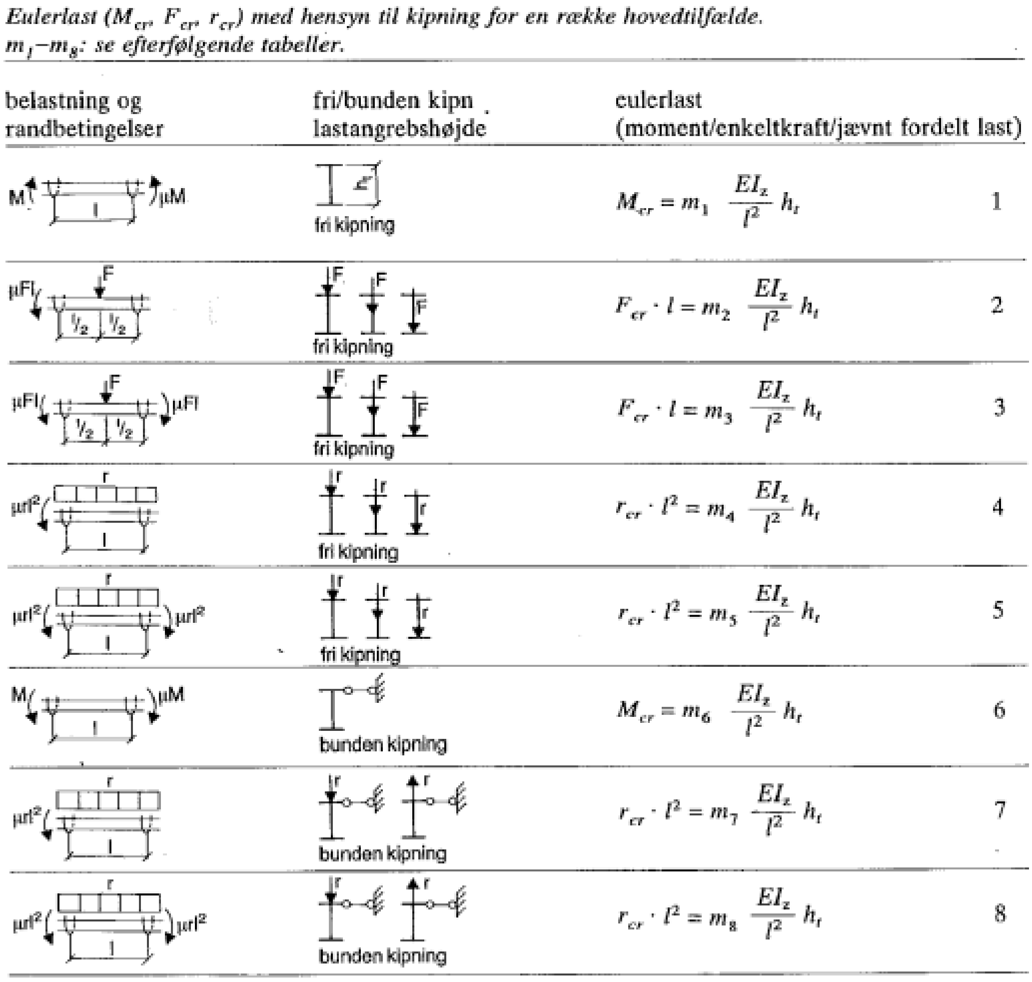
Eulerlast (M_{cr}, F_{cr}, r_{cr}) med hensyn til kipning for en række hovedtilfælde.
$m_1 - m_8$: se efterfølgende tabeller.

belastning og randbetingelser	fri/bunden kipn lastangrebshøjde	eulerlast (moment/enkeltkraft/jævnt fordelt last)	
M, l, μM	fri kipning	$M_{cr} = m_1 \frac{EI_z}{l^2} h_t$	1
μFl, F, l/2, l/2	F, F, F, fri kipning	$F_{cr} \cdot l = m_2 \frac{EI_z}{l^2} h_t$	2
μFl, F, l/2, l/2, μFl	F, F, F, fri kipning	$F_{cr} \cdot l = m_3 \frac{EI_z}{l^2} h_t$	3
μrl², r, l	r, r, r, fri kipning	$r_{cr} \cdot l^2 = m_4 \frac{EI_z}{l^2} h_t$	4
μrl², r, l, μrl²	r, r, r, fri kipning	$r_{cr} \cdot l^2 = m_5 \frac{EI_z}{l^2} h_t$	5
M, l, μM	bunden kipning	$M_{cr} = m_6 \frac{EI_z}{l^2} h_t$	6
μrl², r, l	r, r, bunden kipning	$r_{cr} \cdot l^2 = m_7 \frac{EI_z}{l^2} h_t$	7
μrl², r, l, μrl²	r, r, bunden kipning	$r_{cr} \cdot l^2 = m_8 \frac{EI_z}{l^2} h_t$	8

Figure 3-9: Basic load cases for determining the critical load [L1]

As the model is a simply supported beam with uniformly distributed load, it is clear that load case 5 is the most fitting. Here μ is equal to zero as the moment at the supports are zero.

M_5 is through interpolation in between the tabular values, found to be 44. Thus the critical load is:

$$r_{cr} * l^2 = m_5 \frac{EI_z}{l^2} h_t \Leftrightarrow r_{cr} = \frac{m_5 \frac{EI_z}{l^2} h_t}{l^2} = 144.3 \frac{kN}{m} \tag{3-3}$$

This gives a critical pressure of $144.3 \frac{kN}{m} * \frac{1}{300mm} = 0.481MPa$.

An analytical solution to the same problem exists with the following equation [L15]:

$$F_{cr} = \gamma_4 \frac{\sqrt{EI_z C}}{l^2} \tag{3-4}$$

Where C is the torsional rigidity given by: $C = GI_v$

To find γ_4, the book has a table of solutions based on the dimensionless parameter:

$$\frac{l^2 C}{C_1} \tag{3-5}$$

Where C_1 is the warping rigidity given by : $C_1 = EI_w$

The parameter is found to be 7.72, which gives a γ_4 of 30.5. Thus the total critical load is:

$$F_{cr} = \gamma_4 \frac{\sqrt{EI_zC}}{l^2} = 30.5 \cdot \frac{\sqrt{210000MPa \cdot I_z \cdot C}}{(6000mm)^2} = 792.8kN$$

This gives a critical pressure of: $\frac{792.8kN}{6000mm \cdot 300mm} = 0.441MPa$

All 3 critical pressures are listed in Table 3-1 lie close to each other, so the ANSYS solution is assumed to be correct.

Method	Critical pressure [MPa]
Shell model	0.445
Eurocode	0.481
Analytical solution	0.441

Table 3-1: Critical pressures.

Linear buckling analysis and the analytical solutions only gives the critical load, however they assume ideal structures, and thus imperfections need to be taken into account. Additionally, the linear analysis gives no information on the post buckling state, which is one of the main focuses of this project. Thus a nonlinear buckling analysis needs to be used.

A nonlinear buckling analysis is basically a nonlinear static analysis, where large deflections are taking into account, and the geometry updated in between each load step. Imperfections are normally added by using the mode shapes from the linear buckling analysis, to update the initial mesh.

An initial nonlinear buckling analysis is performed, where imperfections are added as the first mode shape times a scaling factor of 50, giving a mesh as shown in Figure 3-10.

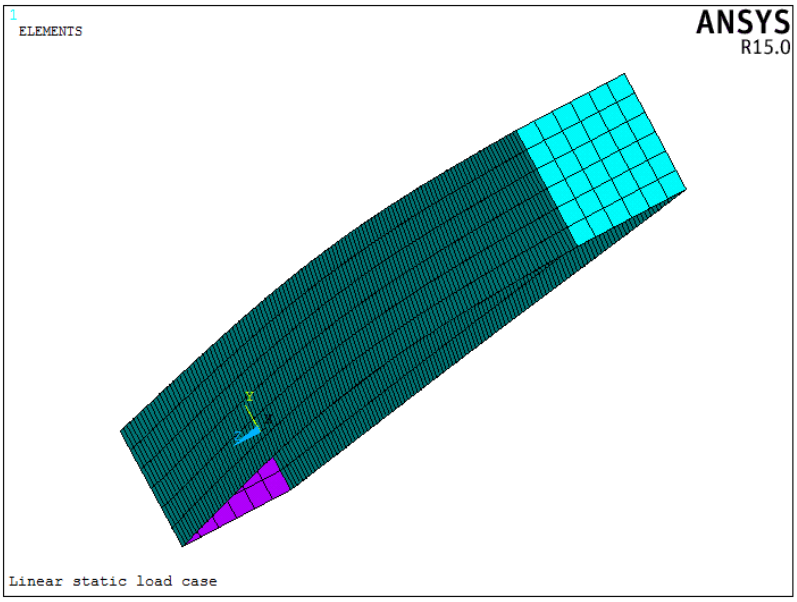

Figure 3-10: Geometry updated with imperfections for a scaling factor of 50

The resulting load-deformation curve is shown in Figure 3-11. Here it can be seen, that for this level of imperfection, instability occurs at 0.21MPa, which is before reaching the yield load.

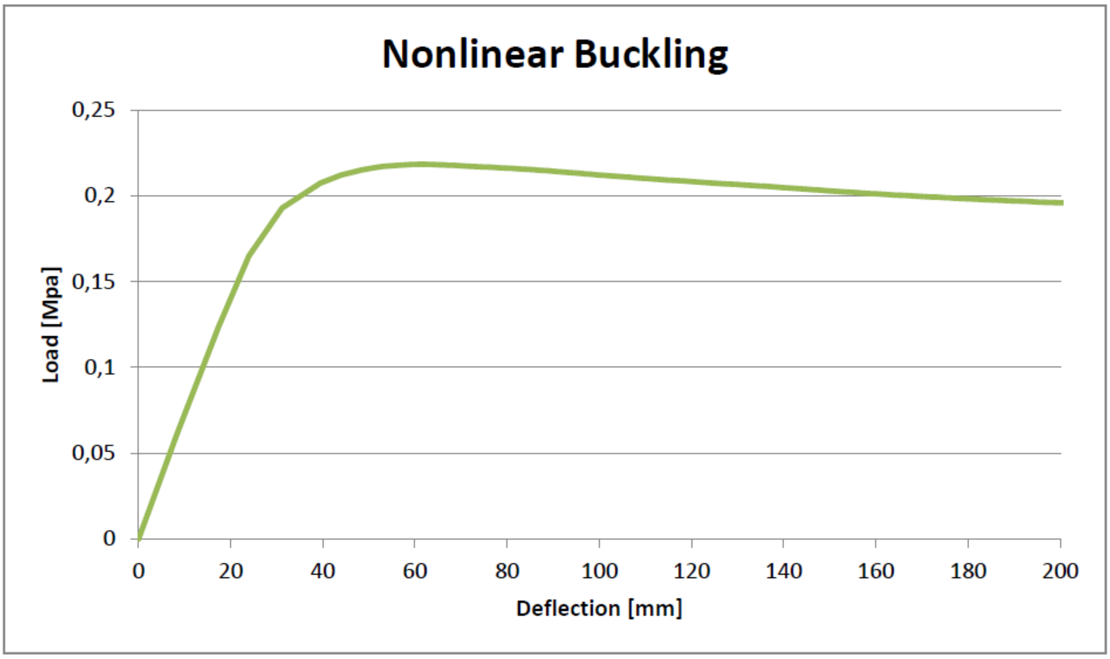

Figure 3-11: Load-deformation curve for a scaling factor of 50

The corresponding deformed structure after buckling occurs can be seen in Figure 3-12.

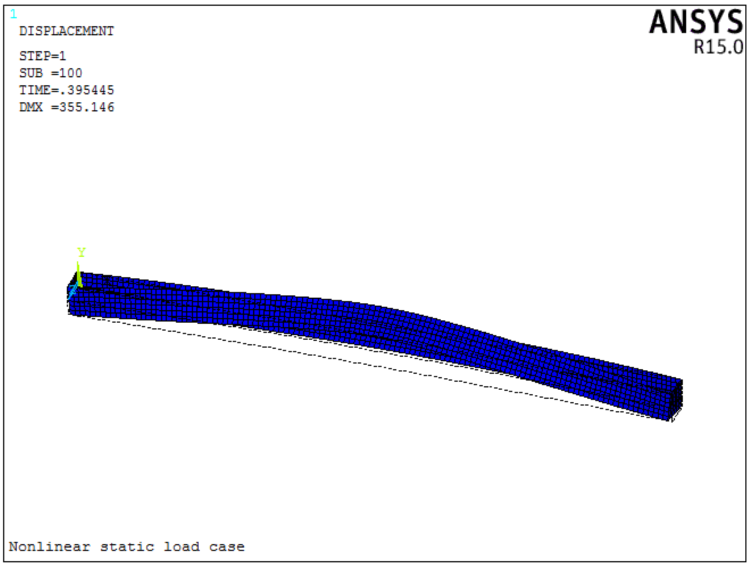

Figure 3-12: Model deformed by lateral buckling

The magnitude of the imperfection is crucial to the analysis, as it decides the capacity of the structure. Standards commonly recommend calibrating the imperfection until you get a peak value comparable to known solutions.

The Eurocode presents a method, where based on the critical load and cross section, a moment reduction factor is determined, leading to a reduced maximum moment. By using some algebra, the corresponding load can be found and then used for calibrating the ANSYS model.

The reduced slenderness ratio is:

$$\lambda = \sqrt{\frac{W f_y}{M_{cr}}} = \sqrt{\frac{mm^3 \cdot 355MPa}{\frac{1}{8} \cdot 144 \frac{N}{mm} \cdot (6000m)^2}} = 0.805$$

Additionally an imperfection factor α is needed. As the ratio $\frac{h_{tot}}{b} = \frac{300mm}{300mm} = 1$, imperfection case c is used, assuming a welded cross section, according to [L1]. This gives an imperfection factor $\alpha = 0.49$. Then this value for determining the reduction factor can be found:

$$\varphi = 0.5(1 + \alpha(\lambda - 0.2) + \lambda^2) = 0.5 \cdot (1 + 0.49 \cdot (0.895 - 0.2) + 0.895^2) = 1.07 \tag{3-6}$$

Then the moment reduction factor is given as:

$$\chi_{LT} = \frac{1}{\varphi + \sqrt{\varphi^2 - \lambda^2}} = \frac{1}{1.07 + \sqrt{1.07^2 - 0.895^2}} = 0.603 \tag{3-7}$$

The reduced moment capacity is then found as

$$M_{LT} = M_Y \chi_{LT} = 355MPa \cdot 1.47 \cdot 10^6 mm^3 \cdot 10^{-6} \cdot 0.603 = 313.6kNm \tag{3-8}$$

This gives a distributed load of

$$M_{LT} = \frac{1}{8} p_{LT} l^2 \Leftrightarrow p_{LT} = 8 \frac{M_{LT}}{l^2} = 8 \cdot \frac{313.6kNm}{(6m)^2} = 69.7 \frac{kN}{m} \tag{3-9}$$

Or a pressure of: $69.7 \frac{kN}{m} \cdot \frac{1}{300mm} = 0.232MPa$

Here it can be seen that the Eurocode method predicts lateral buckling occurring before yielding as well. To calibrate to this, the scaling factor is altered iteratively until the peak is reasonably close to 0.232MPa. The resulting load deformation curves are shown in Figure 3-13.

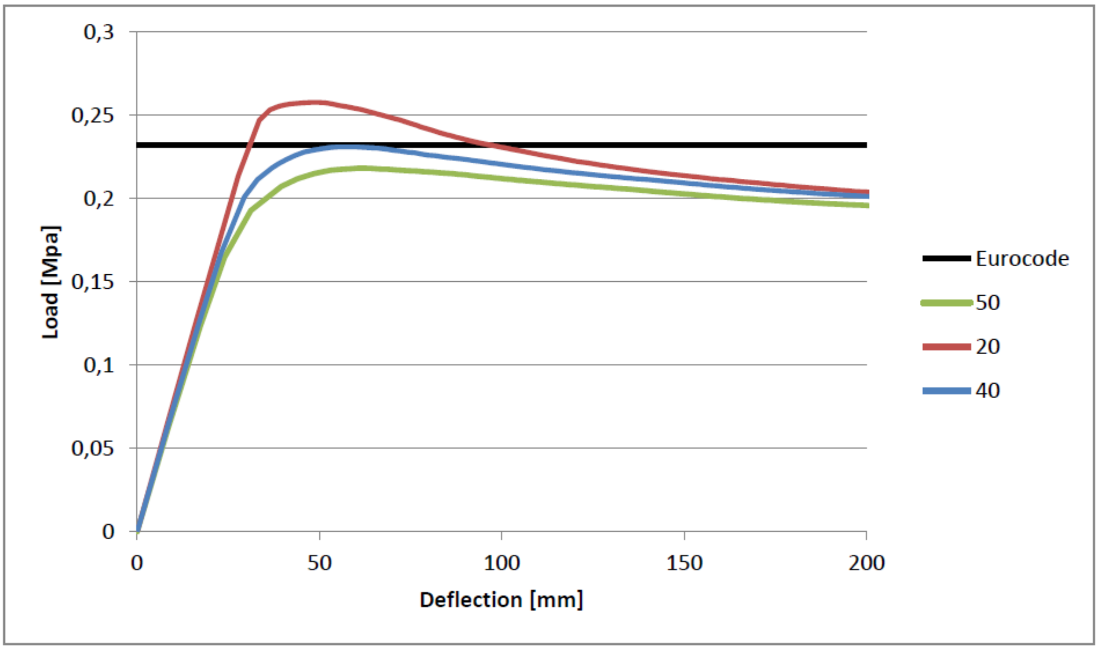

Figure 3-13: Iterated load deformation curves

A scaling factor of 40 matches the Eurocode solution, and since the linear buckling shapes the imperfection is based on is normalized to 1mm, this gives an imperfection of 40mm for the beam.

To get an overview of the significance of the buckling the load-deformation curve is plotted together with the critical pressure, and solutions that are linear elastic and Elasto-Plastic, but disregards buckling. This graph is shown on Figure 3-14.

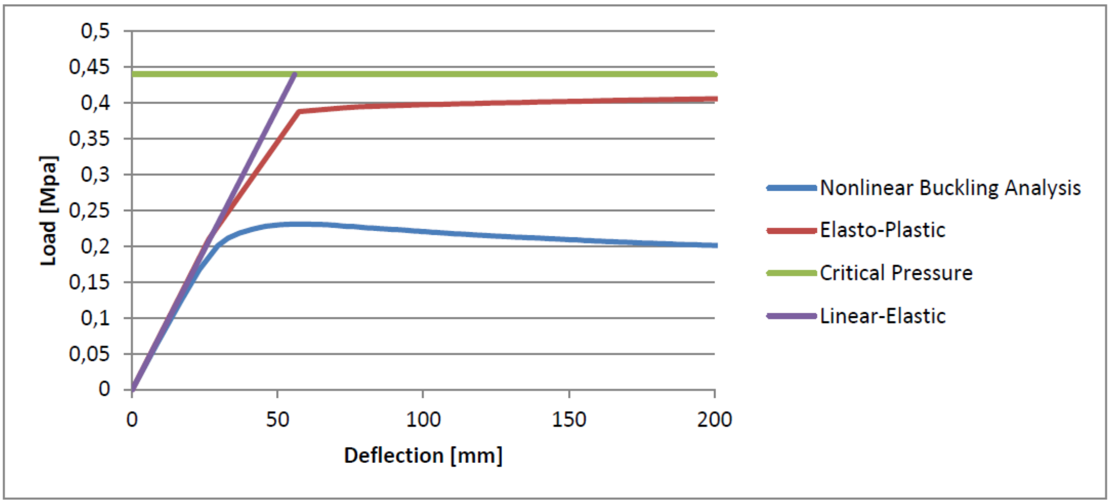

Figure 3-14: Load Deformation For increasingly complex static models.

3.3 Instability in plate model

3.3.1 Boundary conditions of plate

Like the I-profile, the plate model will also be modeled using shell elements. Because issues appeared with using the SHELL281 element and the force controlled analysis introduced in Chapter 3.3.2, the plate model will instead use the 4noded SHELL181 element sketched on Figure 3-15, which is the 4noded equivalent of SHELL281.

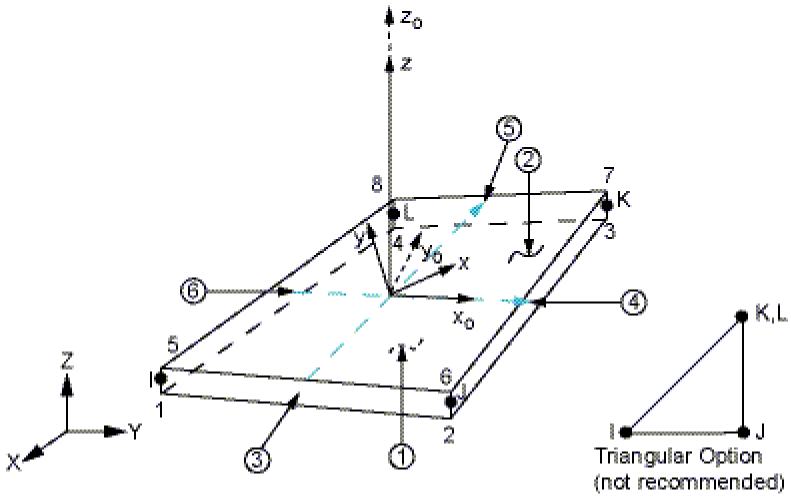

Figure 3-15: The SHELL181 element used in ANSYS [L12]

The SHELL181 is still capable of modeling the nonlinear effects like the SHELL281 element, but it might need some more elements for convergence.

The plate model is simply supported along all 4 edges and the in plane supports are sketched in Figure 3-16. It is only loaded on one edge, but thanks to the reaction force in the supports on the left edge, the end result will be equivalent to that of Figure 2-5.

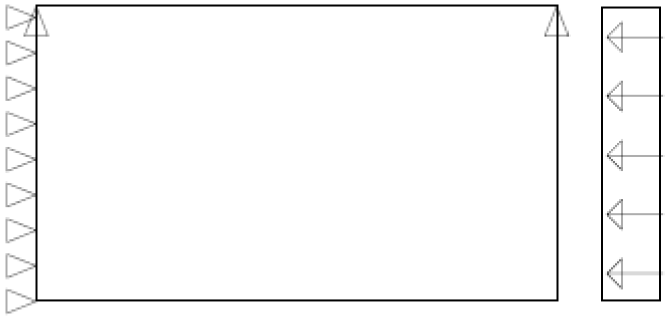

Figure 3-16: In plane supports of plate model.

The relevant deformations of the plate model only happen when it buckles out of plane, and the linear elastic model cannot capture that deformation, and thus cannot be verified.

To compensate for that a slightly different load case is setup, where the entire plate is loaded with an out of plane pressure. A convergence study of this setup shows that an element size of 25mm is sufficient for modeling the out of plane deformations. The resulting mesh is depicted on Figure 3-17.

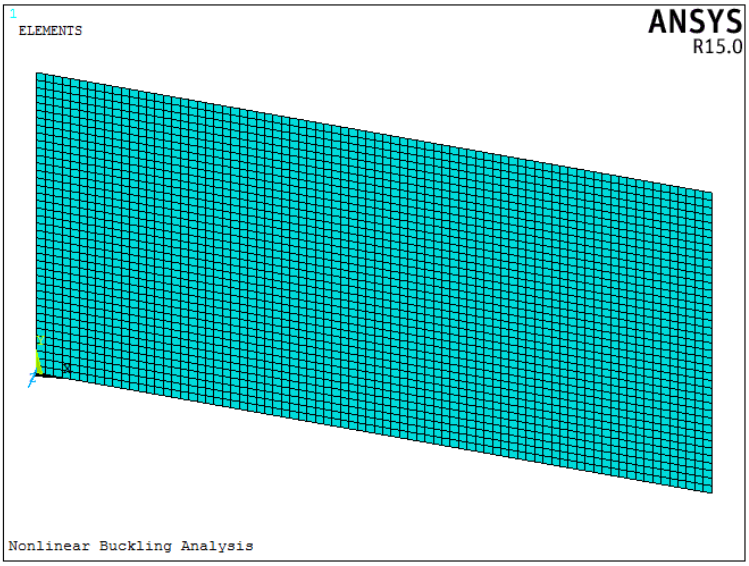

Figure 3-17: Mesh of plate model

3.3.2 Buckling analysis of plate

The general procedure in doing a full nonlinear buckling analysis is the same as for the model of the beam:

- Do linear buckling analysis
- Compare with analytical solutions
- Add imperfection based on linear buckling modes
- Do a nonlinear static analysis

Based on the geometry and the boundary conditions, the buckling shape of the plate model is expected to be similar to the sketch in Figure 3-18.

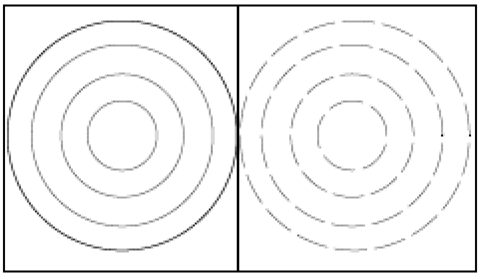

Figure 3-18: Expected buckling shape

In [L15] an analytical solution for the critical buckling load of the given boundary conditions is given with the following expression:

$$N_{cr} = \frac{\pi^2 D}{a^2}\left(m + \frac{1}{m}\frac{a^2}{b^2}\right)^2 \tag{3-10}$$

Where

m is the number of half waves.

a is the width of the plate

b is the height of the plate

D is the flexural rigidity

For plates, the bearing capacity is not necessarily emptied at the initial buckling load. This is because the stresses are redistributed because of the deformation giving an uneven stress distribution along the edge as depicted on Figure 3-19.

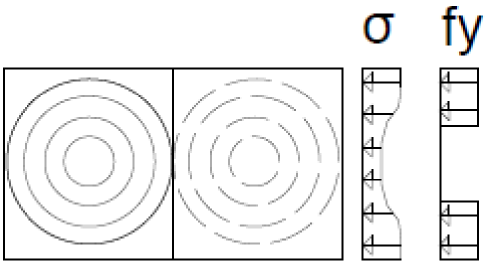

Figure 3-19: Effective width

In standards this is normally approached by utilizing the effective width method as illustrated on Figure 3-19. By calculating when this will result in the yield stress a post critical bearing capacity can be obtained. The procedure for this is as follows:

First the slenderness is computed by:

$$\lambda = \sqrt{\frac{f_y}{\sigma_{cr}}} \tag{3-11}$$

Where

f_y is the yield stress

σ_{cr} is the critical stress given by $\sigma_{cr} = \frac{N_{cr}}{t}$

Then the ratio ρ is found by:

$$\rho = \begin{cases} 1 & for\ \lambda \leq 0.673 \\ \dfrac{\lambda - 0.055 \cdot (3 + \psi)}{\lambda^2} & for\ \lambda \geq 0.673 \end{cases} \tag{3-12}$$

Where

ψ is the ratio between ratio between the stresses at the edges and is 1 for the case of pure compression

Then the effective width is determined by:

$$b_{eff} = \rho \cdot b \tag{3-13}$$

Which then can be translated into a post critical capacity by:

$$F_{pcr} = f_y \cdot b_{eff} \cdot t \tag{3-14}$$

Performing a linear buckling analysis with boundary conditions as shown in Figure 3-16 gives the first buckling mode as shown on Figure 3-20.

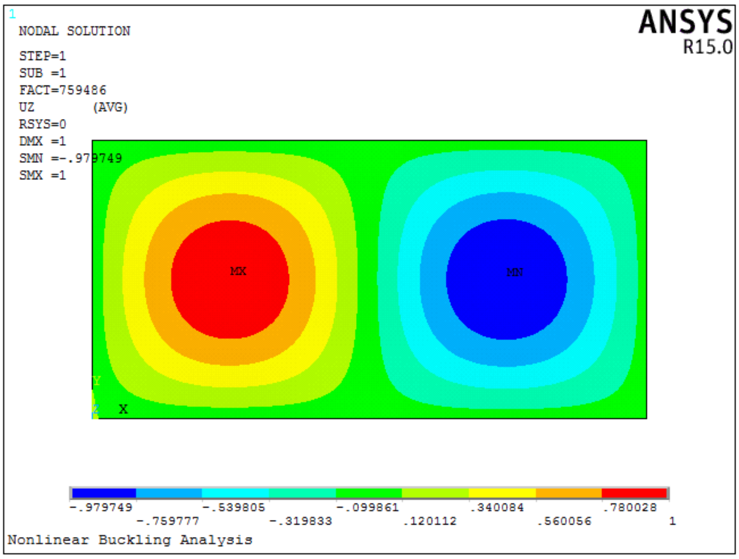

Figure 3-20: 1st buckling mode

As seen on the figure this gives a critical buckling load of $759586N{\sim}760kN$

Using Equation (3-10) an analytical load of $759\,\frac{kN}{m}$ is obtained, making the total critical load $759\,\frac{kN}{m} \cdot b = 759kN$. The results are seen to be very close.

Additionally the post critical strength is found to be 1475 kN, so it is expected to occur after the buckling load.

With the linear buckling analysis successful, the next step is determining an appropriate level of imperfection. The Eurocode have several different suggestions for the imperfection depending on the context, but since the plate model is a very simple structure it is sufficient to use the equivalent geometric imperfections as shown in Figure 3-21.

Table C.2: Equivalent geometric imperfections

Type of imperfection	Component	Shape	Magnitude
global	member with length ℓ	bow	see EN 1993-1-1, Table 5.1
global	longitudinal stiffener with length a	bow	min (a/400, b/400)
local	panel or subpanel with short span a or b	buckling shape	min (a/200, b/200)
local	stiffener or flange subject to twist	bow twist	1 / 50

Figure 3-21: Equivalent geometric imperfections [L3]

The imperfection is local and the shape is that of a buckling mode so the magnitude should be min(a/200 , b/200). b is the smallest at 1000mm giving an imperfection of:

$$\mathrm{e} = \frac{b}{200} = \frac{1000mm}{200} = 5mm$$

In theory, when the imperfection is zero, buckling occurs at the critical load level where it abruptly changes equilibrium path. In practice where an imperfection is present, the change in equilibrium is more gradual, and the buckling load can be hard to determine. Because of this, analyses using different levels of imperfections beside 5mm are also performed.

The context of the plate model is that it is part of a plate field within an offshore module. This means that the edges are assumed to remain straight. This is done by applying the load as a displacement, rather than a force. The corresponding force is found by taking the reaction force in the supports at the left edge.

In Figure 3-22 results for the displacement controlled nonlinear buckling analysis for varying levels of imperfection is depicted. It can be seen that a low level of imperfection gives a more visible change in equilibrium path, and also a buckling load that is close to the Euler load.

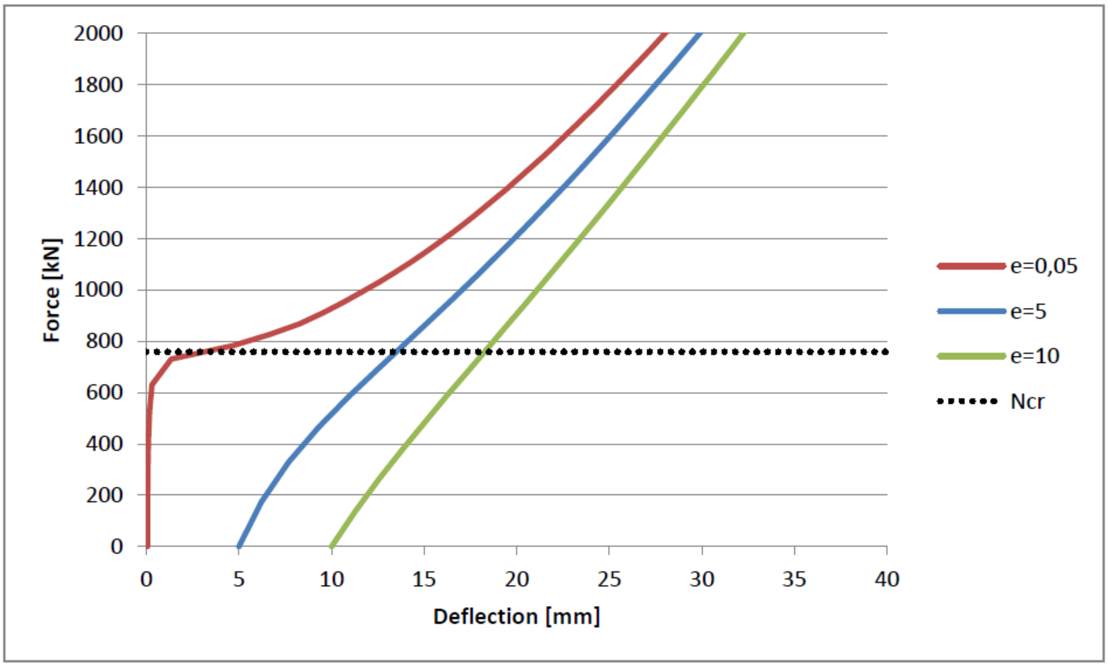

Figure 3-22: Nonlinear elastic buckling analysis results

Examining the out of plate deformation of the nonlinear buckling on Figure 3-23 shows buckling shapes matching what was expected.

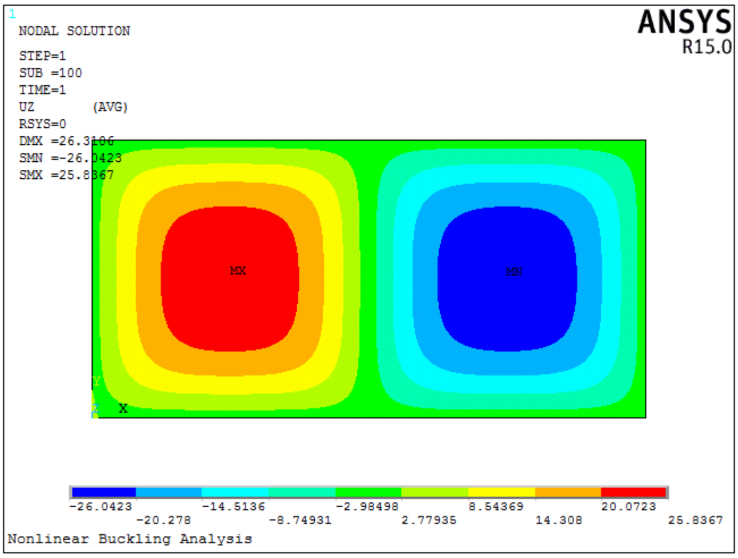

Figure 3-23: Out of plane deformation at load of 200kN and e=5mm

The Von Mise stress distribution for the same analysis is depicted in Figure 3-24. Here it is seen that the uneven stress distribution assumed in Figure 3-19 is present.

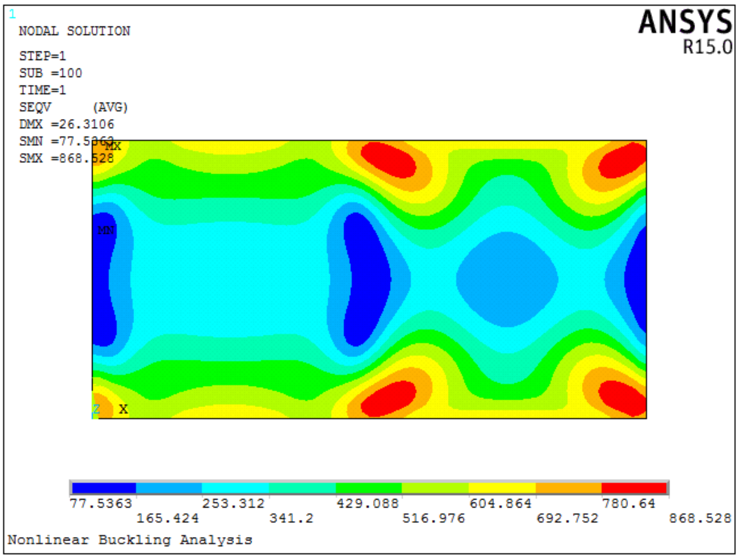

Figure 3-24: Von Mise stress distribution for displacement controlled analysis

Including plasticity in the displacement controlled analysis gives the results shown in Figure 3-25. Here it can be seen that the analyses gives a peak load capacity, after which it gradually lessens. This peak is the post critical bearing capacity as given by the FEM model.

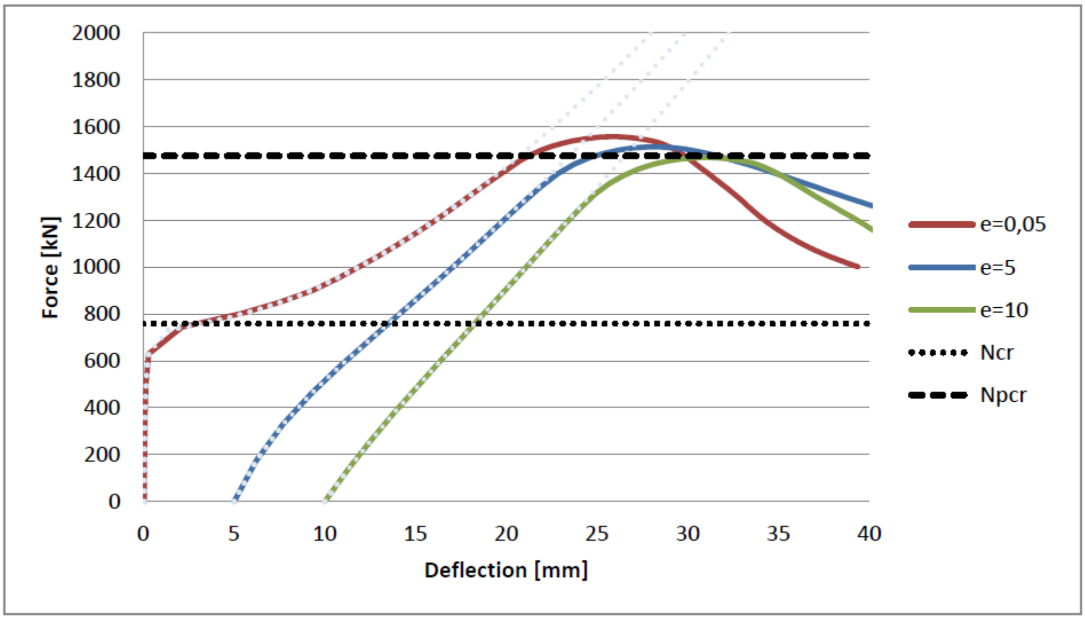

Figure 3-25: Nonlinear elasto-plastic buckling analysis results. White dotted lines are elastic results.

Illustrated by a thick black dotted line, the analytical post critical capacity (named 'Npcr' on the figure) is depicted together with the FEM results. Here it can be seen that the results are relatively close, but still lower than the FEM results. This is due to the influence of the slenderness as was shown in [L16]. In the thesis the author produces Figure 3-26, which shows how the results vary as a function of the slenderness. Here 'Ultimate load (Winter)' is equivalent to the Eurocode approach for the case of pure compression. 'NEN 6771' is a dutch standard not used in the current project.

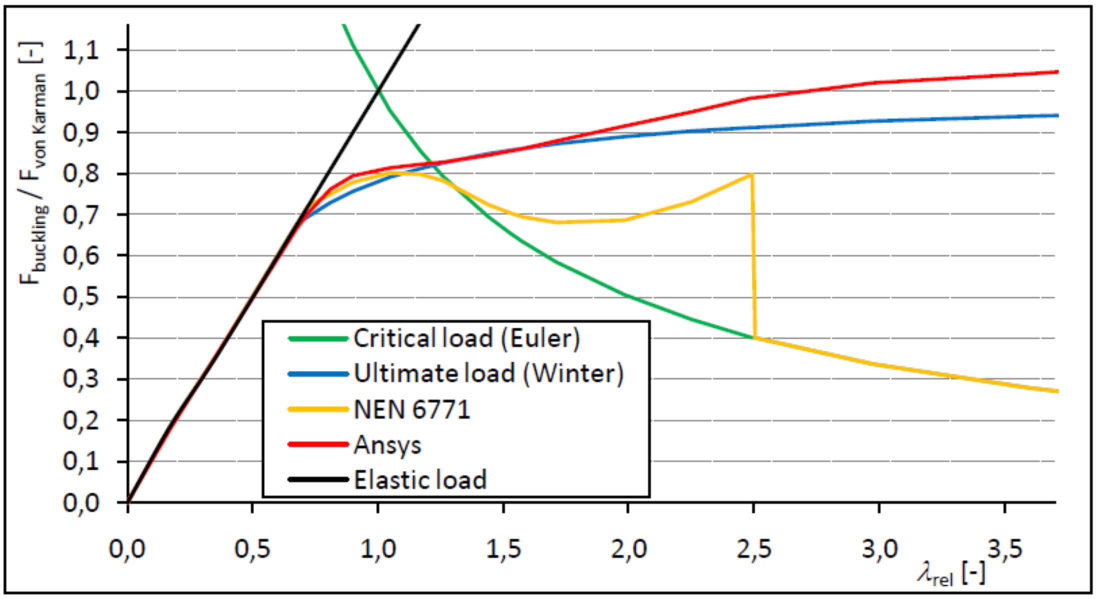

Figure 3-26: Influence of slenderness on different loads [L16]

Displacement controlled analyses are impractical for transient analysis, as the force has to be determined indirectly, so a force based alternative is set up.

However, for a force-controlled analysis, extra measures need to be implemented in order to assure that the loaded edge remains straight.

This is done by adding beam elements of relatively high stiffness to the loaded edge.

To confirm the accuracy of this approach a geometric nonlinear analysis is executed like shown earlier in Figure 3-23. This is compared to the displacement controlled equivalent in Figure 3-27, where the black dotted lines are the displacement controlled analysis results.

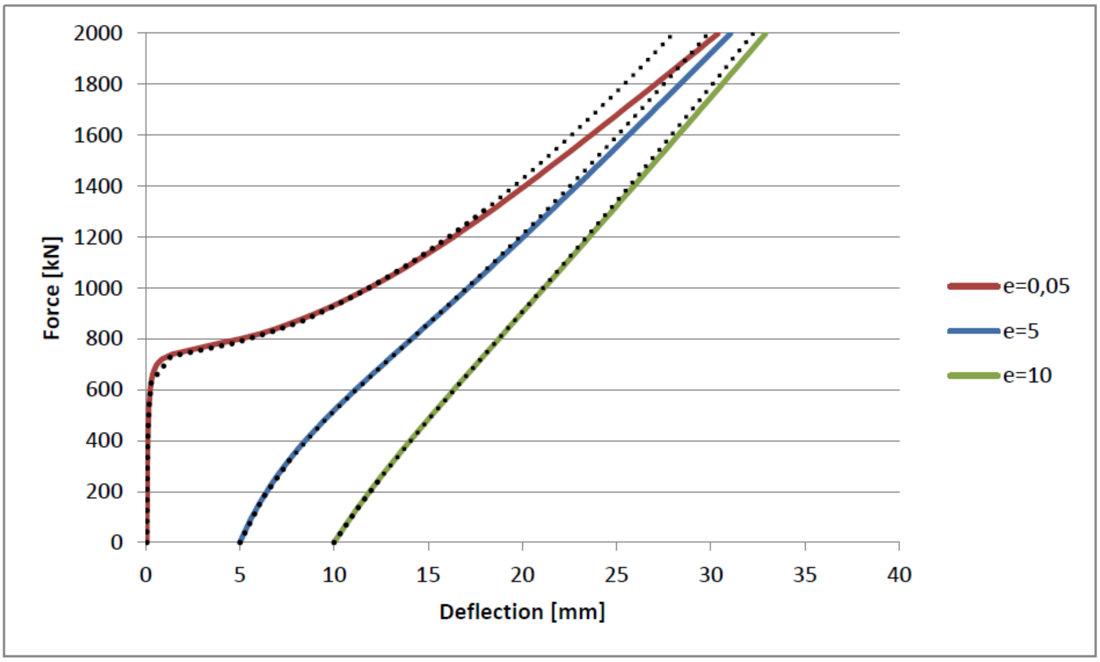

Figure 3-27: Nonlinear elastic buckling results for force controlled analysis.

There are some deviations at higher loads for the case of very small imperfections, but since that case was only included for demonstrative purposes, the results are deemed acceptable.

To further examine the force controlled model, a Von Mise stress distribution is included in Figure 3-28.

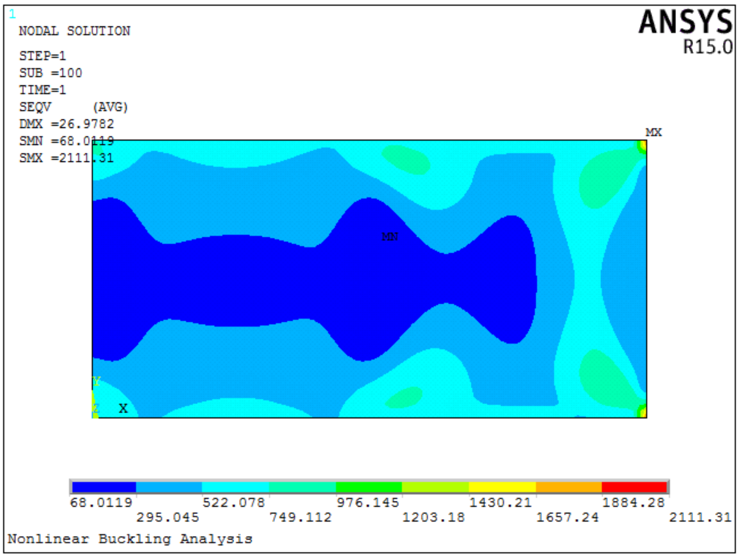

Figure 3-28: Von Mise stress distribution for force controlled analysis

As depicted on Figure 3-28, the force controlled contains stress singularities, which makes it unusable for modeling material nonlinearities. The focus of this thesis is on investigating the buckling that occurs before plasticity, so it is accepted for the transient analyses, as the material model can remain elastic.

3.4 Partial conclusion

The I-profile and plate model was modeled with shell elements, and linear static and linear buckling results were compared with analytical and norm solutions. The results were found to match well to the known solutions. The nonlinear buckling analysis of the I-profile was carried out using an imperfection based on its lateral buckling mode and the imperfection size was calibrated to maximum load capacity as given by the Eurocode. Imperfections in the plate model were chosen according to recommended values in the Eurocode. It was found that a displacement controlled analysis was optimal for the static analysis of the plate model, and a force controlled model was developed for use in dynamic analyses.

4 DYNAMIC RESPONSE

In this chapter, the dynamic response, as modeled in ANSYS, will be documented and held up against hand calculations and static analysis results when possible. The chapter will include natural frequency analyses, linear response as well as geometric and material nonlinearities. Additionally the explicit solver LS-DYNA will be held up against the implicit solver in ANSYS to determine the most efficient approach for the analyses in this thesis.

4.1 Natural frequency analysis

As the I-profile model is relatively simple, a reasonable estimate of the first Eigen frequency can be found through a SDOF analogy, where the point mass is assumed to be in the center of the beam as illustrated in Figure 4-1. This leads to an assumed parabolic mode shape, as also shown in Figure 4-1.

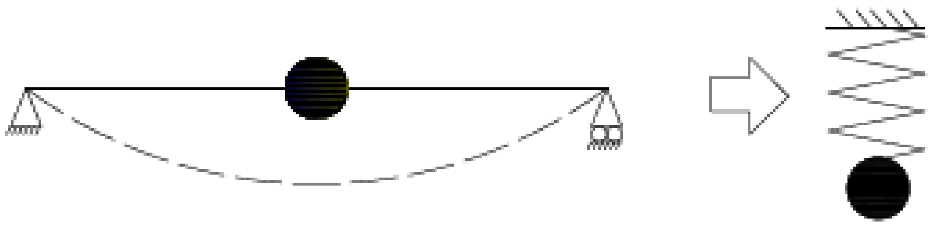

Figure 4-1: Sketch of SDOF analogy.

Here the total mass is:

$$m_1 = \frac{\rho \cdot A \cdot l}{2} = \frac{7850\frac{kg}{m^3} \cdot 1.17 \cdot 10^4 \cdot 10^{-6} m^2 \cdot 6m}{2} = 275kg$$

The stiffness is given by:

$$k_1 = \frac{48EI_y}{l^3} = \frac{48 \cdot 210000MPa \cdot 1.99 \cdot 10^8 mm^4}{(6000mm)^3} = 9302\frac{N}{mm}$$

Then the Eigen frequency is found by:

$$\omega_1 = \sqrt{\frac{k_1}{m_1}} = 183\frac{rad}{s} \quad ; \quad f_1 = \frac{1}{2\pi\omega_1} = 29.2\frac{1}{s} \tag{4-1}$$

The corresponding period is then found to be:

$$T = \frac{1}{f_1} = 0.034s = 34ms$$

A modal analysis is performed in ANSYS in order to obtain the lowest Eigen frequencies and the corresponding Eigen modes. The results from the first 5 modes are listed in Table 4-1.

Mode	Angular Eigen frequency	Eigen frequency	Eigen period
	$\frac{rad}{s}$	$\frac{1}{s}$	ms
1	106.2	16.9	59.2
2	130.1	20.7	48.3
3	179.1	28.6	34.9
4	419.1	66.7	14.9
5	429.1	68.3	14.6

Table 4-1: Eigen frequency results for beam model

The first 2 are far from the hand calculations, and inspecting the Eigen modes in Figure 4-2 reveals that they are different from the one assumed in the hand calculations. The first one is similar to the hand calculations, but on a different axis and the second is reminiscent of lateral buckling.

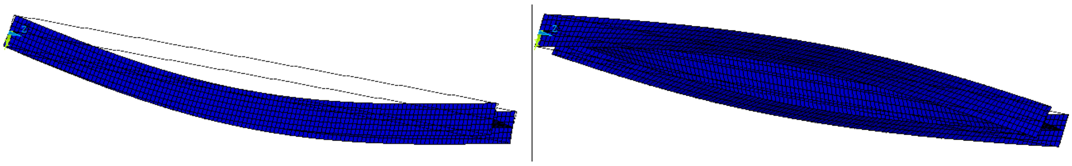

Figure 4-2: Left: 1st Eigen mode. Right: 2nd Eigen mode

The 3rd Eigen mode however, matches closely with the hand calculations period of 34ms, having an Eigen period of 0.035s=35ms.

By looking at the mode shape for this mode (Figure 4-3), it is seen that it matches, the assumed mode shape in the hand calculations.

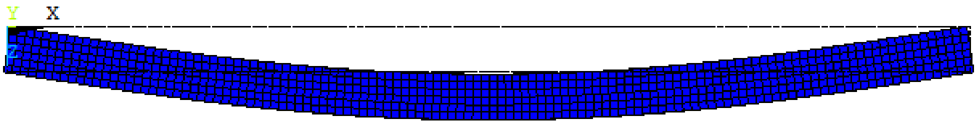

Figure 4-3: 3rd Eigen mode as depicted in ANSYS

To test the first Eigen frequency, hand calculations are redone, but with the second moment of area of the weak axis and thus the assumption that the mode shape is like in Figure 4-2 (Left).

The mass is unchanged, and the stiffness is given by:

$$k_1 = \frac{48EI_z}{l^3} = \frac{48 \cdot 210000MPa \cdot 6.75 \cdot 10^7 mm^4}{(6000mm)^3} = 3150\frac{N}{mm}$$

Then the angular eigen frequency is found by:

$$\omega_1 = \sqrt{\frac{k_1}{m_1}} = 107\frac{rad}{s} \quad ; \quad f_1 = \frac{1}{2\pi\omega_1} = 17.01\frac{1}{s}$$

The corresponding period is then found to be:

$$T = \frac{1}{f_1} = 0.059s = 59ms$$

The results are seen to be close to the ANSYS results.

For the plate model, the first 5 Eigen frequencies are listed in Table 4-2.

Mode	Angular Eigen frequency	Eigen frequency	Eigen period
	$\frac{rad}{s}$	$\frac{1}{s}$	ms
1	192.9	30.7	32.6
2	308.5	49.1	20.4
3	502.0	79.9	12.5
4	657.9	104.7	9.5
5	772.2	122.9	8.1

Table 4-2: Eigen frequency results for plate model

With the first 2 Eigen modes depicted in Figure 4-4.

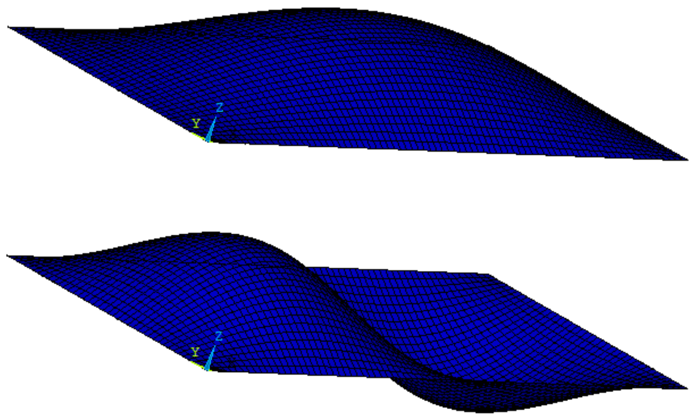

Figure 4-4: Top: 1st Eigen mode. Bottom: 2nd Eigenmode

4.2 Damping

For the impulse loading used for this model, damping is generally less important since the important response lies in the initial load duration, rather than the post loading response.

The structural damping is modeled using the Rayleigh damping model. Rayleigh damping assumes that the damping can be described as a combination of the mass and stiffness matrix like in Equation (4-2):

$$C = \alpha M + \beta K \tag{4-2}$$

Where

C is the damping matrix

M is the mass matrix

K is the stiffness matrix

α is the mass coefficient

β is the stiffness coefficient

To determine the damping coefficients the following equations are used, where damping is found based on a chosen frequency span:

$$\alpha = \frac{2\omega_1\omega_2(\zeta_1\omega_2 - \zeta_2\omega_1)}{{\omega_2}^2 - {\omega_1}^2} \tag{4-3}$$

$$\beta = \frac{2(\zeta_2\omega_2 - \zeta_1\omega_1)}{{\omega_2}^2 - {\omega_1}^2} \tag{4-4}$$

Where

$\omega_1$is the lowest angular Eigen frequency of the span

$\omega_2$is the highest angular Eigen frequency of the span

ζ_1 is the damping ratio corresponding to ω_1

ζ_2 is the damping ratio corresponding to ω_2

The chosen span is the from the 1st Eigen frequency the 3rd Eigen frequency, in order to cover the Eigen modes relevant to the loading used on this model. Ideally damping ratios would be determined by doing measurement on an experimental specimen, but when experimental data is unavailable standards suggest a structural damping of 0.15% for both frequencies. This gives the following damping coefficients:

$$\alpha = \frac{2 \cdot 106.2\frac{rad}{s} \cdot 179.1\frac{rad}{s} \cdot \left(0.0015 \cdot 179.1\frac{rad}{s} - 0.0015 \cdot 106.2\frac{rad}{s}\right)}{\left(179.1\frac{rad}{s}\right)^2 - \left(106.2\frac{rad}{s}\right)^2} = 0.201s^{-1}$$

$$\beta = \frac{2 \cdot \left(0.0015 \cdot 179.1\frac{rad}{s} - 0.0015 \cdot 106.2\frac{rad}{s}\right)}{\left(179.1\frac{rad}{s}\right)^2 - \left(106.2\frac{rad}{s}\right)^2} = 1.048 \cdot 10^{-5}s$$

Depending on the frequency, the damping is either dominated by the mass or the stiffness. Figure 4-5 shows the damping as a function of the frequency, for the previously computed mass- and stiffness coefficients. Generally, mass is dominant at the lower frequencies and stiffness at higher frequencies which is clearly observable in Figure 4-5. For the relevant frequency span, as illustrated by the black Eigen frequency lines on Figure 4-5, it can be seen that neither mass nor stiffness dominates the damping.

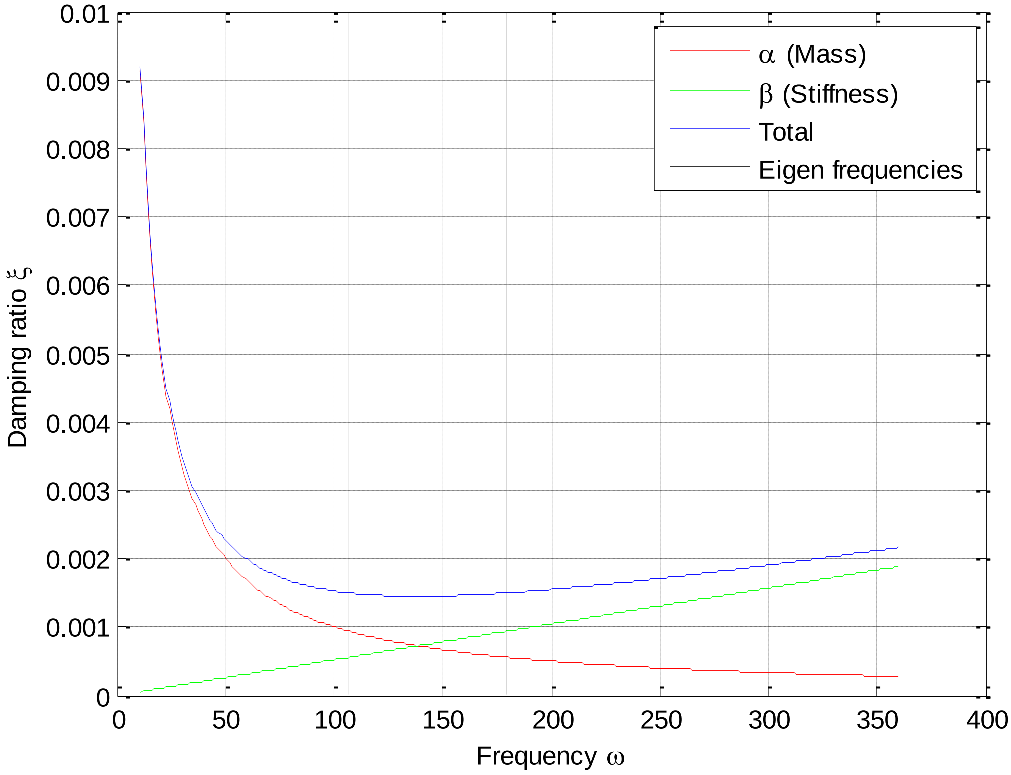

Figure 4-5: Damping ratios for Rayleigh damping

4.3 Linear elastic dynamic analysis

Doing a linear dynamics analysis for an impulse loading of 1 MPa and a duration time of 100ms gives the response shown in Figure 4-6.

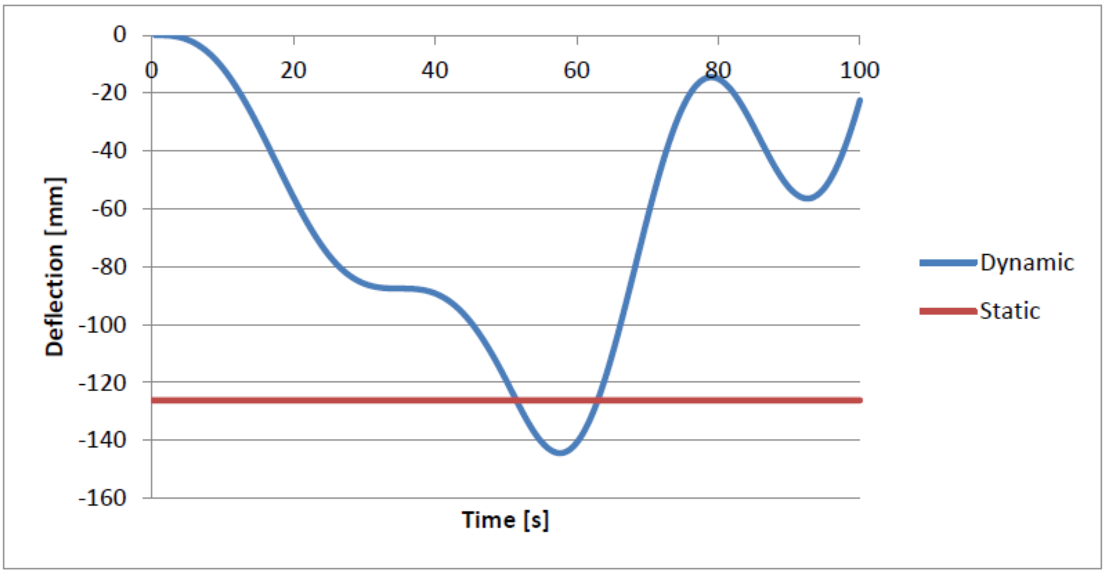

Figure 4-6: Deflection for linear dynamic analysis versus a linear static analysis

Here it can be seen that the peak response is significantly above the static solution showing the inertial effects and the dynamic amplification.

With a maximum deflection of 144.9mm this gives a dynamic amplification factor of:

$$DAF = \frac{x_{dyn}}{x_{static}} = \frac{-144.9mm}{-127.8mm} = 1.134$$

3rd mode should be activated due to the load bending the beam into that shape, but the response will be examined to determine the Eigen modes activated by the impulse load. To do this an additional simulation is executed, where the beam is allowed to freely oscillate for while after the loading. The resulting deflection response is shown on Figure 4-7, where free oscillations occur between 100 and 800 milliseconds.

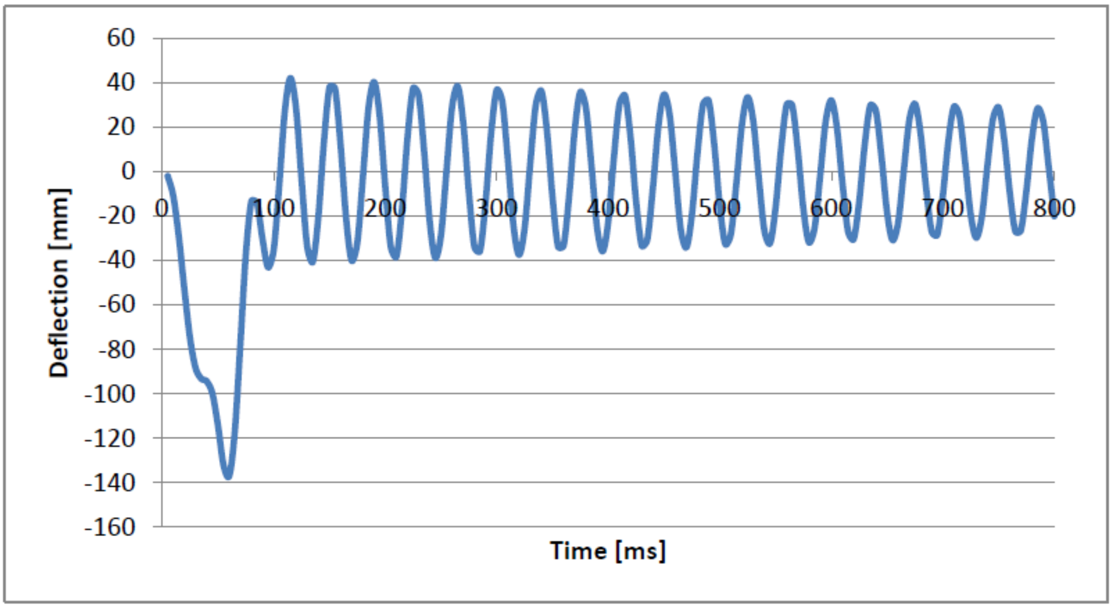

Figure 4-7: Deflection with free oscillation after loading.

Closer inspection of the animation show that it oscillates with the 3rd mode shape.

To determine the Eigen frequency, a Fast Fourier Transform (FFT) is performed on the free oscillations. The results are displayed in Figure 4-8.

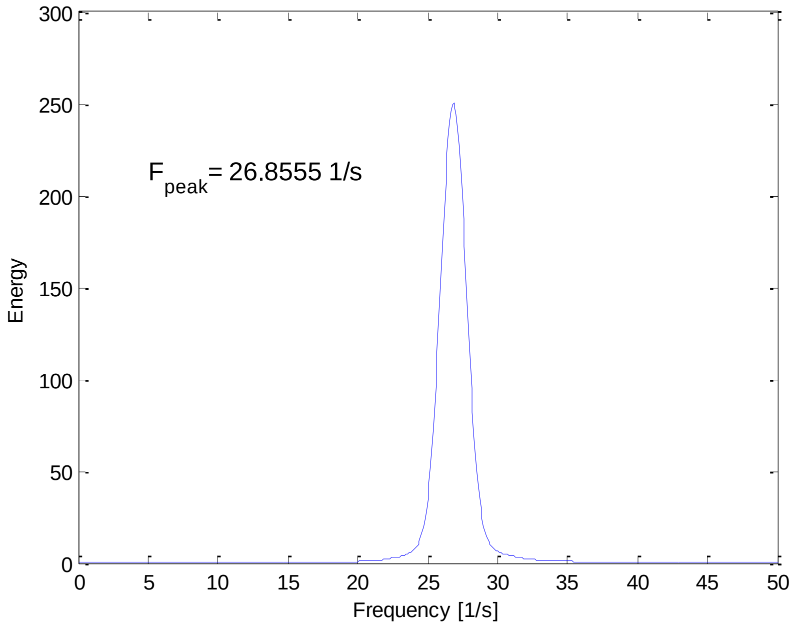

Figure 4-8: Fast Fourier Transform (FFT) of free oscillations.

The frequency is seen to match closely with the 3rd Eigen frequency of 28.6 1/s.

As shown in Figure 4-6, notable dynamic amplification is present, making it necessary to investigate the response further. For this purpose a number of analyses with different duration times, and thus different load frequencies are performed, in order to map the dynamic response in the frequency spectrum. The structural responses of these analyses are shown in Figure 4-9.

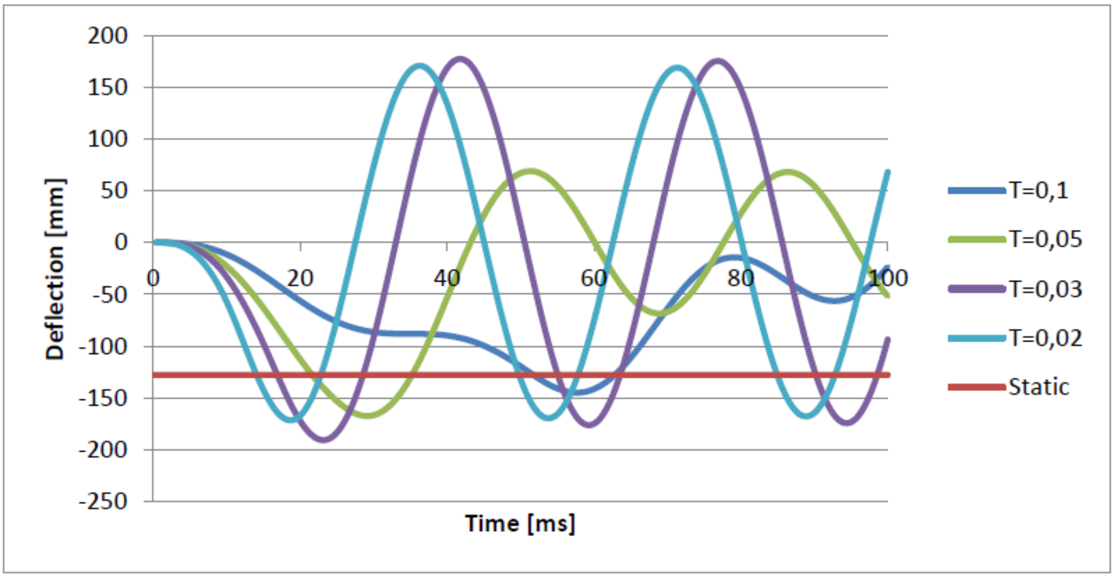

Figure 4-9: Deflection results for loads with varying frequencies. Periods are in seconds.

The plot shows that while all responses show dynamic amplification, the magnitude of the amplification varies. Calculation of the DAF for each response is listed in Table 4-3.

Duration time [ms]	Maximum Deflection [mm]	DAF [-]
20	-171.0	1.35
30	-189.7	1.50
50	-166.4	1.31
100	-144.4	1.14

Table 4-3: Dynamic amplification for different duration times.

To get a visual overview of the dynamic amplification, the DAF's are plotted as a function of the duration time in Figure 4-10.

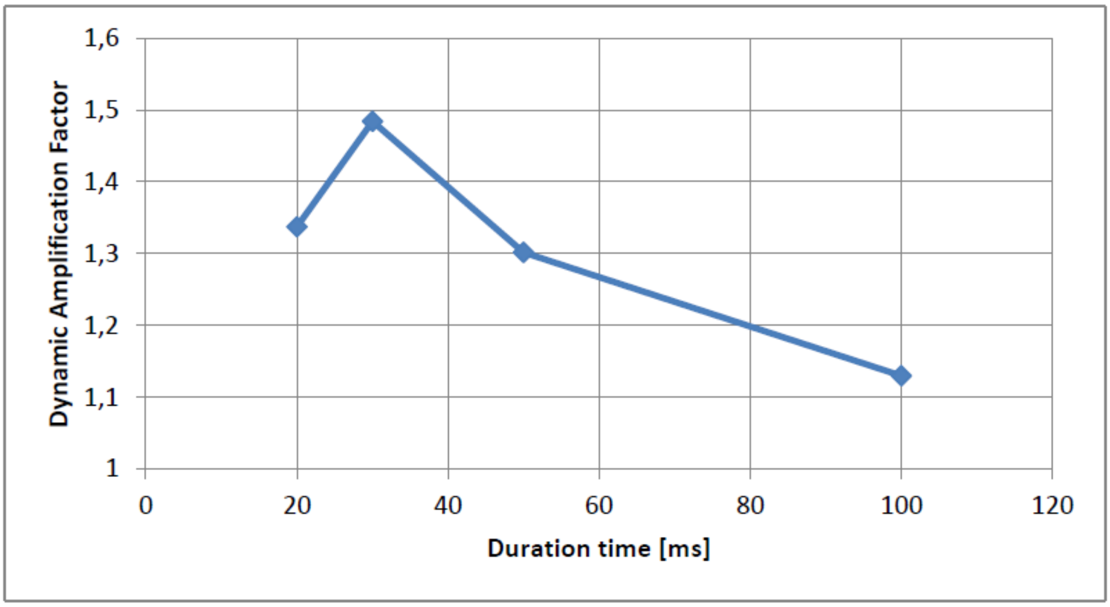

Figure 4-10: Dynamic Amplification factors for the deflections plots.

The results show a clear peak in the response at a duration time of 30 milliseconds which is close to the 3rd Eigen period of 35 milliseconds.

As the plate model is dependent on the geometric nonlinearity to obtain a proper response, no linear dynamics analysis will be performed of the plate.

4.4 Nonlinear dynamic analysis

4.4.1 Geometric nonlinear dynamic analysis

A load of 0.42 MPa is used for the I-profile, and while it could be higher the permanent deformations from lateral buckling in the material nonlinear case becomes so large that it is no longer feasible to talk about post buckling strength. Thus to have comparable load cases 0.42 MPa is used.

Like in the static nonlinear buckling analysis, buckling is enabled by activating large deflections and thus geometric nonlinearity, and giving the model an imperfection based on linear buckling modes. Calibration of the static analysis gave an imperfection of 40mm, which will also be used in the dynamic analysis. Computing the nonlinear model with the initial imperfections, give the response shown in Figure 4-11.

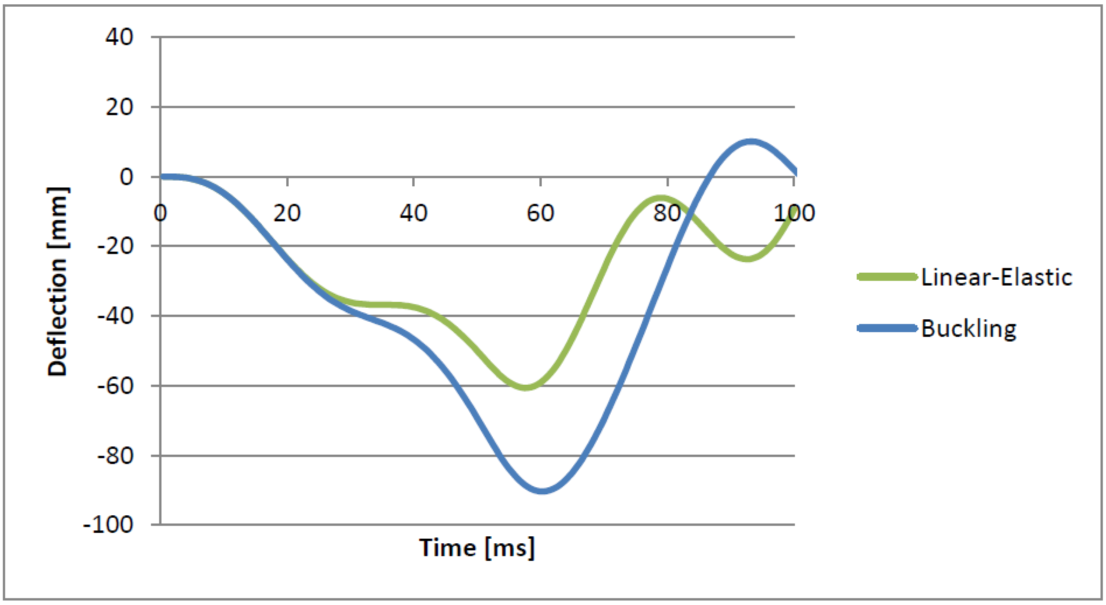

Figure 4-11: Nonlinear dynamic with and without imperfection

Doing a nonlinear dynamics analysis of the plate model gives the response shown in Figure 4-12. The static case depicted for comparison is from the nonlinear buckling results in Figure 3-27. Dynamic amplification can be observed, but since the plate's Eigen frequencies and the impulse load frequency are relatively far apart, the amplification is small.

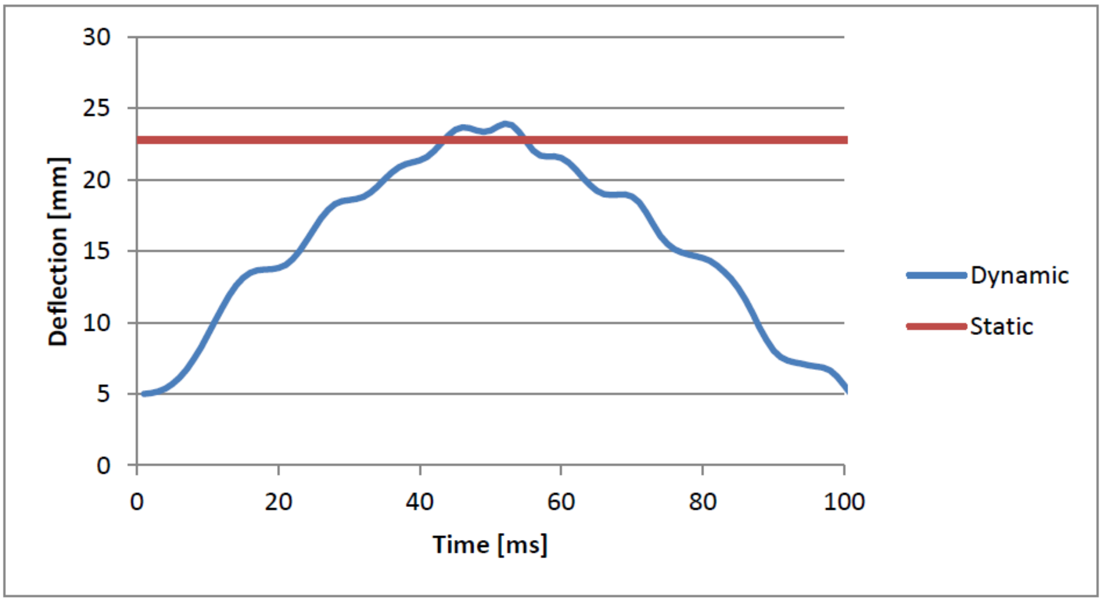

Figure 4-12: Dynamic plate buckling

4.4.2 Material nonlinear dynamic analysis

Like for the static nonlinear analyses, the bilinear isotropic hardening model from Figure 2-1 is also used for modeling plasticity in the dynamic analyses.

To determine the effects of including hardening the linear and material nonlinear structural response is plotted together in Figure 4-13.

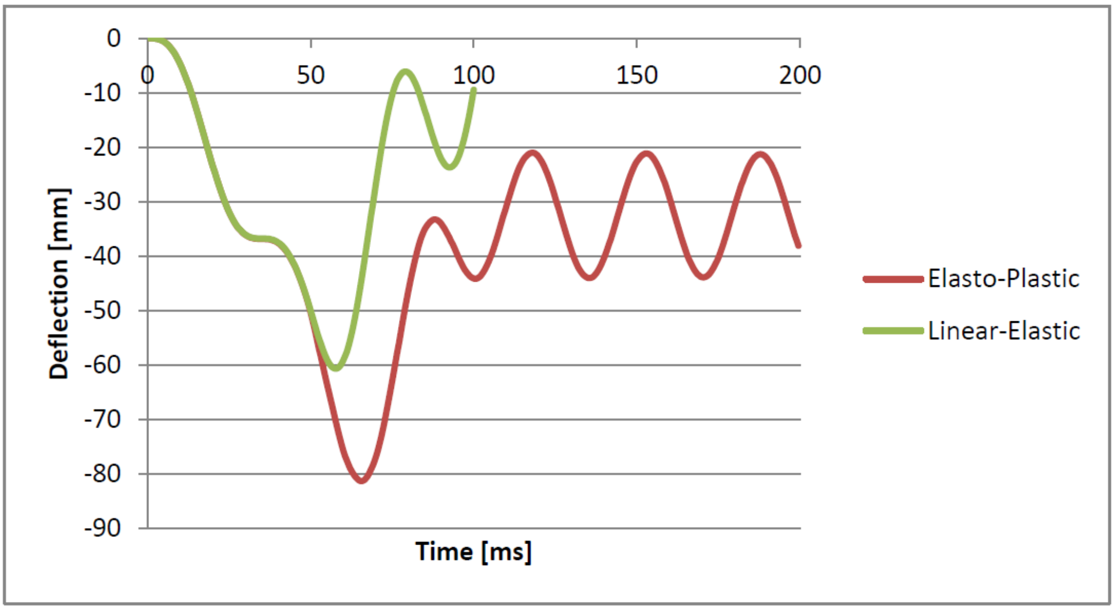

Figure 4-13: Linear and nonlinear dynamic response for a pressure of 0.42MPa.

Here a clear increase in the maximum deflection is observed yielding an increase from the linear response of approximately 30%. Additionally it can be seen that the plastic response starts to oscillate around a permanent deformation of ~30mm, thus confirming that plasticity has occurred.

While the above response shows significant differences when plasticity is included, it doesn't give an accurate idea of how much of an impact plasticity can have on the response. For this purpose, an analysis with a pressure load of 0.5MPa is performed giving the response as shown on Figure 4-14.

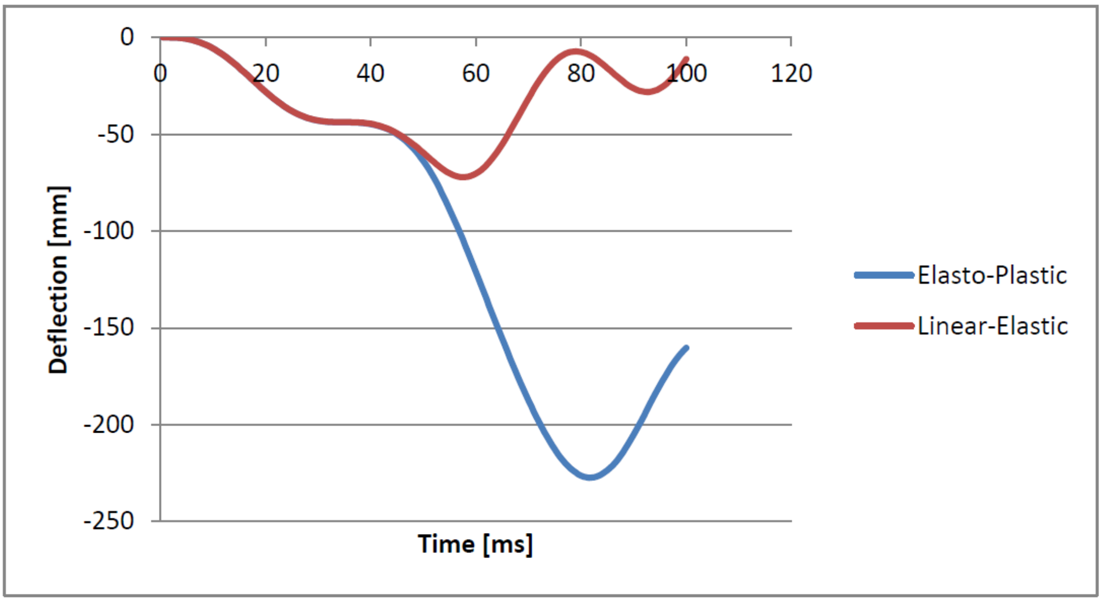

Figure 4-14: Linear and nonlinear dynamic response for a pressure of 0.5MPa.

Here the increased deflection because of plasticity is far more pronounced giving an increase of more than 300%.

4.4.3 Full nonlinear dynamic analysis

Including the initial imperfection of 40mm, thus allowing for dynamic buckling coupled with plasticity, gives the response in Figure 4-15.

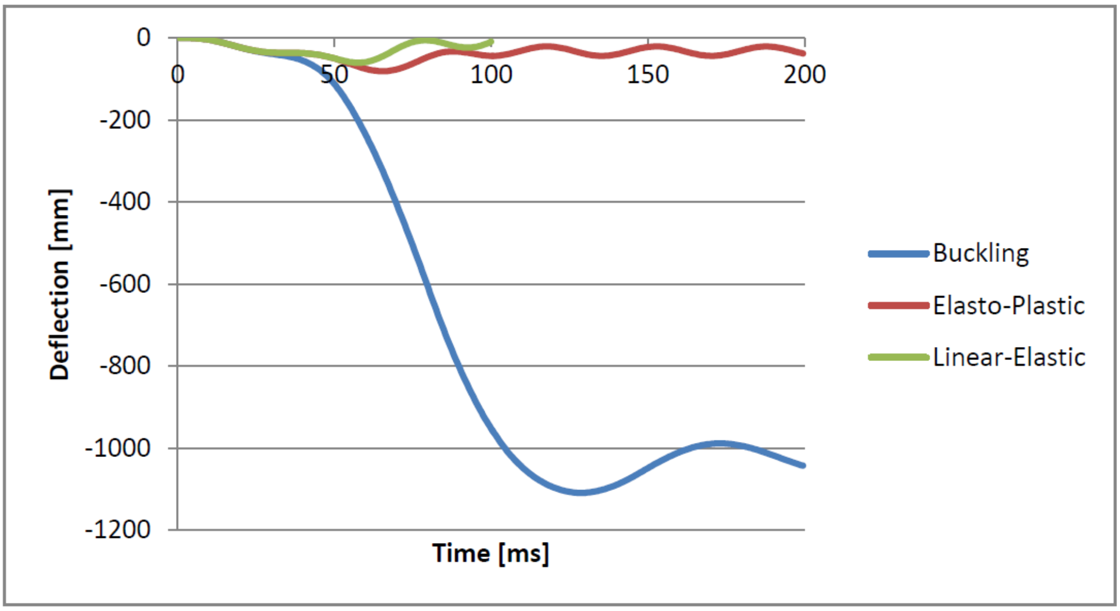

Figure 4-15: Response with and without imperfections.

Here it is clear that the inclusion of buckling gives an extreme deflection in comparison to the other analyses, highlighting just how important stability is.

The resulting deformed model is depicted in Figure 4-16. Doing a closer inspection of the deformed shape reveals that the deformation comes from the lateral buckling phenomenon and it has also started to develop local buckling modes near the center of the beam.

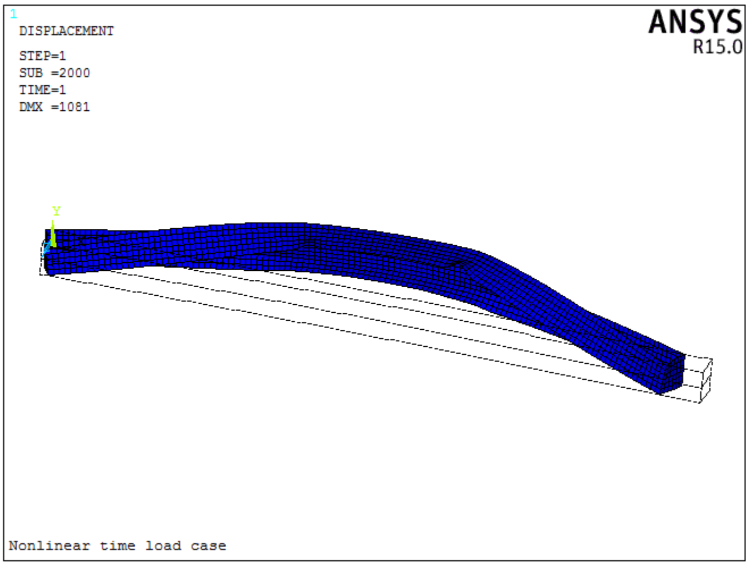

Figure 4-16: Model deformed by instability

4.5 Implicit vs explicit time integration

When doing transient structural analyses, time integration is generally the preferred method. As mentioned in Chapter 1.2.3, time integration is divided into two over all approaches; implicit and explicit time integration. The purpose of this section is to determine which one is preferable for the explosion analyses, by comparing the structural responses.

The LS-DYNA analyses used in this thesis are made in ANSYS Workbench using an LS-DYNA extension available on the ANSYS home page [W3] that creates a Workbench interface for LS-DYNA.

As ANSYS LS-DYNA use lumped matrices, it cannot employ an equivalent to the 8noded SHELL281 (Figure 3-3), and must instead use a 4noded shell element which is shown in Figure 4-17.

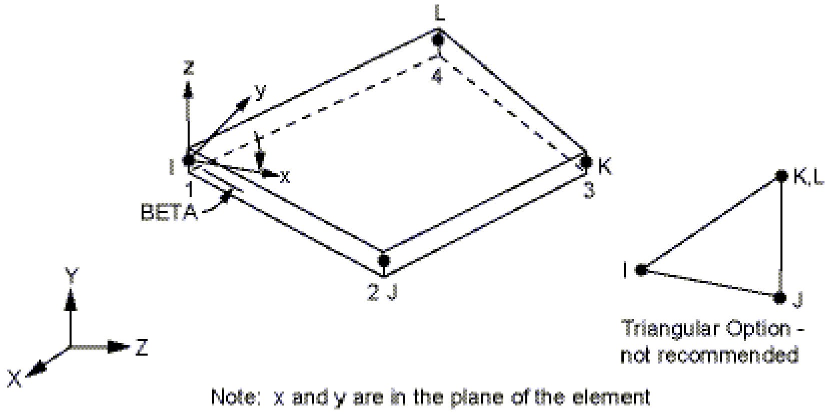

Figure 4-17: 4noded SHELL163 element

The SHELL163 element has 12 degrees of freedom in each node making for a total of 48 degrees of freedom per element. These degrees included translations and rotations, but also velocities and acceleration in the x-y and z directions.

Computing the theoretical critical time step from Chapter 1.2.3 would require ANSYS LS-DYNA to do a modal analysis each time it solves, in order to obtain the highest Eigen frequency, so the program uses another approach.

The time step size is instead computed by the following expression:

$$\Delta t = 0.9 \frac{l}{c} \tag{4-5}$$

Where 0.9 is a safety factor that decreases the time step size in order to ensure stability.

l is the characteristic length of an element determined by:

$$l = \frac{A}{\max\left(l_1, l_2, l_3, l_4\right)} \tag{4-6}$$

c is the wave propagation velocity found by:

$$c = \sqrt{\frac{E}{\rho}} \tag{4-7}$$

The shell model used consists of quadratic shell elements with 50mm sides, resulting in a time step size of:

$$c = \sqrt{\frac{E}{\rho}} = \sqrt{\frac{210000MPa}{7850\ kg/m^3}} = 5172 \frac{m}{s}$$

$$l = \frac{A}{\max\left(l_1, l_2, l_3, l_4\right)} = \frac{50mm \cdot 50mm}{\max\left(50mm, 50mm, 50mm, 50mm\right)} = 50mm$$

$$\Delta t = 0.9 \frac{l}{c} = 0.9 \cdot \frac{50mm}{5172 \frac{m}{s}} = 8.7 \cdot 10^{-6} s = 8.7 \cdot 10^{-3} ms$$

First, a linear dynamic analysis is performed in ANSYS LS-DYNA, in order to compare the results with the implicit solver in ANSYS. The results are shown on Figure 4-18. The pressure load is 0.42 MPa.

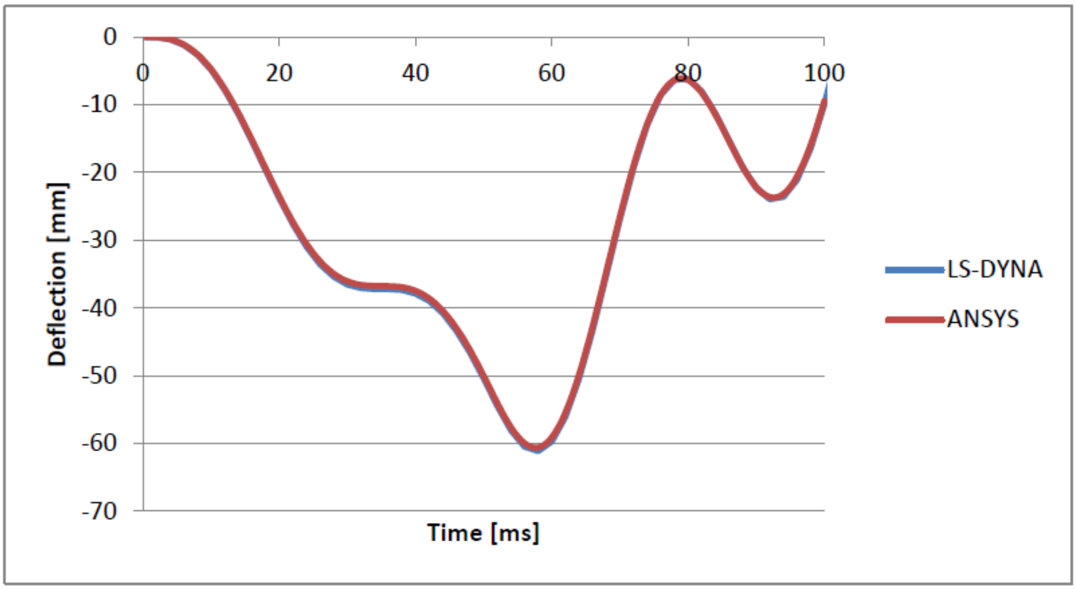

Figure 4-18: Linear dynamics comparison

The results match almost exactly, proving that LS-DYNA is usable in terms of the linear analysis.

Then a nonlinear analysis with plasticity is executed with the same pressure load. The results are depicted on Figure 4-19.

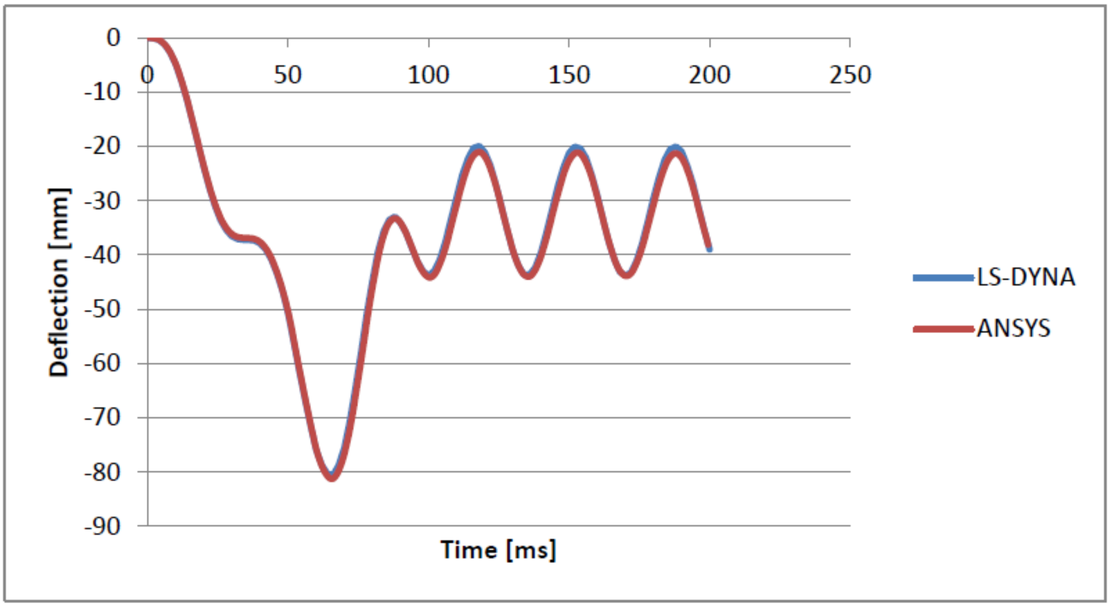

Figure 4-19: Nonlinear dynamics comparison

Like with the linear dynamics analysis, the results are almost exactly the same confirming that ANSYS LS-DYNA can model plasticity. Additionally the computation time was significantly reduced.

Because of these similarities and faster solver, the remaining analyses are carried out in ANSYS LS-DYNA.

4.6 Partial conclusion

The natural frequency analysis done in ANSYS was compared to hand calculations and found to be accurate and have mode shapes identical to the ones assumed in hand calculations. Linear dynamics results confirmed the presence of dynamic amplification of the response and the deflection matches the expected deflection shape. Nonlinear dynamics analyses for geometric and material nonlinearity were performed, and it was found that individually dynamic buckling and plasticity have significant impact on the maximum response and must be included in an explosion analysis. Combining the two nonlinearities resulted in a deflection many times the linear elastic response. Implicit and explicit solvers were compared and the results were found to be close, while the explicit solver needed computation time many times less than the implicit solver. Because of this, the explicit solver was chosen for further analyses.

5 STRAIN RATE EFFECTS

When a structure is subjected to short duration loads such as dropped objects or explosion impulses it is significantly influenced by the so called strain rate effects. Strain rate effects occur when the load rate undergo sudden changes, which subsequently affects the corresponding material response. The strain rate effects generally include increased strength of the material, as illustrated on Figure 5-1, and increased brittleness.

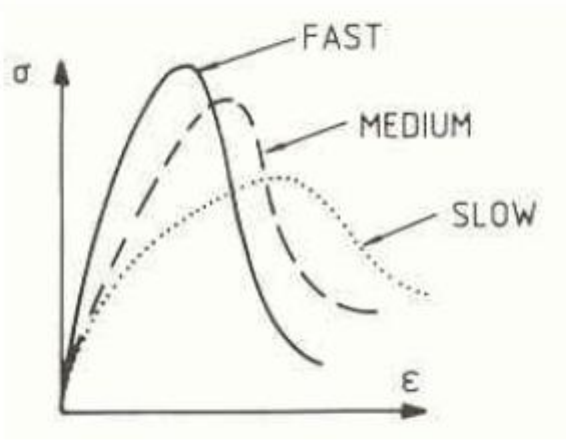

Figure 5-1: Strain rate effects on material response curves [L11].

The increase in brittleness, while accompanied by an increase in material strength, also cause fracture to occur at lower strain levels, as shown in Figure 5-2. Another way to express this is that the fracture energy, the strain energy needed to cause fracture, lowers when brittleness increases. For the example on Figure 5-2, the fracture energy would be determined by computing the area under the graph.

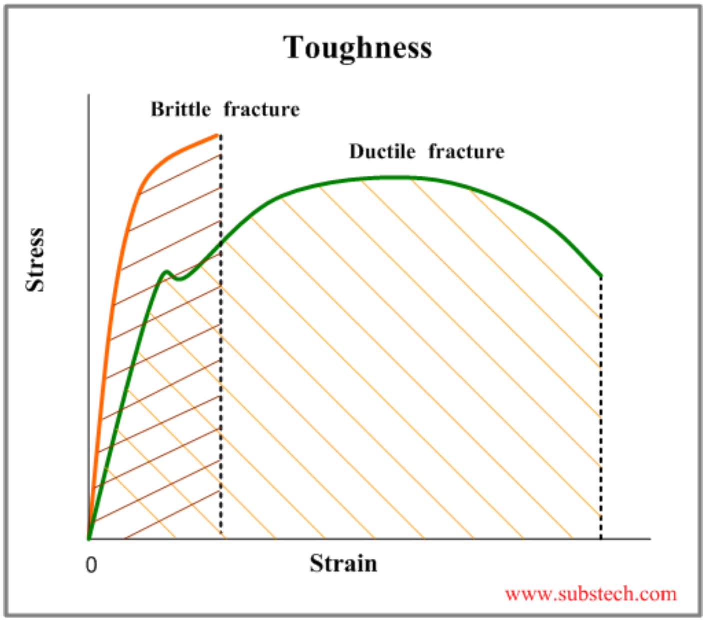

Figure 5-2: Brittle vs ductile fracture [W4].

When conducting experiments to achieve the fracture energy of a material, a common test setup is the Charpy impact test, which is a standardized test proposed by George Charpy in 1901. A sketch of the basic setup of the Charpy impact test is depicted on Figure 5-3.

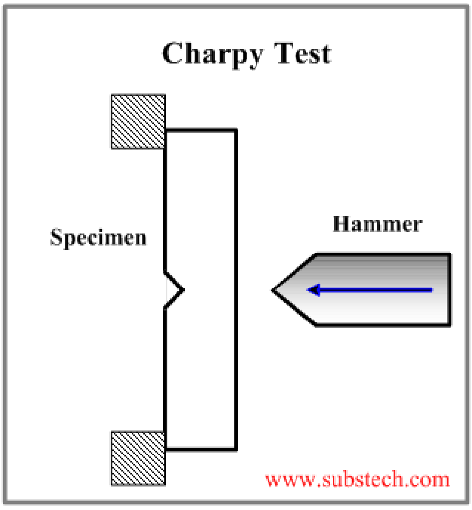

Figure 5-3: Sketch of the Charpy test [W4].

An explosion on an offshore module is characterized by a short duration time and a high pressure. The duration time is also often close to the natural period of the structure. Because of this explosion loads often induce plasticity and large permanent deformations. With the possibility of instabilities like lateral or local buckling these deformations will only increase.

As mentioned in Chapter 1, it is necessary to take nonlinear effects like material nonlinearity in the form of plasticity and geometrical nonlinearities like buckling to obtain a response that is representative for the true response. By neglecting any of these, one risk underestimating the deformations which are fatal to the design process and is thus not an acceptable approach.

However, because of the short duration time, other dynamic effects such as strain rates have a real and measurable influence on the response. Strain rates effects make the structure more brittle and increase the material strength, so including it will yield a beneficial effect on the response and in the pursuit of optimized design procedures, it is worth including when reasonable.

This section is dedicated to investigating just how much of an effect strain rates will have on the response and how they can be included most efficiently.

5.1 Cowper-Symonds equation

There exist many strain rates model, but based on experiments and experience, the Cowper-Symonds model has been found to be one of the most suitable for offshore structures. The Cowper-Symonds equation is as follows:

$$\frac{\sigma_d}{\sigma_s} = 1 + \left(\frac{\dot{\varepsilon}}{D}\right)^{\frac{1}{q}} \tag{5-1}$$

Where

σ_s is the static yield stress [MPa]

σ_d is the dynamic yield stress [MPa]

$\dot{\varepsilon}$ is the strain rate [s^{-1}]

D [s^{-1}] and q [-] are strain rate parameters

The basic principle of the Cowper-Symonds model is the introduction of the dynamic yield stress which is higher than the static yield stress. The higher yield stress result in larger bearing capacity of the structure as the effects of plasticity is reduced.

ANSYS LS-DYNA uses a slightly modified and expanded variant as shown in Equation (5-1):

$$\sigma_d = \left[1 + \left(\frac{\acute{\varepsilon}}{D}\right)^{\frac{1}{q}}\right]\left(\sigma_s + \beta E_p \varepsilon_p^{eff}\right) \tag{5-2}$$

Where

β is a hardening parameter going from 0 to 1, determining the rate of isotropic and kinematic hardening in the Finite Element model. $\beta = 1$ is pure isotropic hardening and $\beta = 0$ is pure kinematic hardening

E_p is the plastic hardening modulus given by:

$$E_p = \frac{E_{tan}E}{E - E_{tan}}$$

ε_p^{eff} is the effective plastic strain

According to [L14] the strain rate can be estimated based on the cross section class as listed in Table 5-1.

Criteria	Strain rate [s^{-1}]
Class 1 and 2 cross sections with deflection in the plastic range	1
Class 1 and 2 cross sections with deflection in the elastic range	0.2
Class 3 and 4 cross sections	0.02

Table 5-1: Recommended strain rates

If further experimental data to determine the strain rate parameters is unavailable, the DNV-RP-C208 standard suggests the strain rate parameters listed in Table 5-2.

Strain rate parameter	Value
D	4000 [s^{-1}]
q	5 [-]

Table 5-2: Recommended strain rate parameters

The model used in this report is a profile with class 1, plastic deflection and isotropic hardening and no further data is available on the strain rate parameter, so the parameters used for the strain rate model for the structure is as shown in Table 5-3.

Parameter	Value
Yield stress	355 [MPa]
Plastic hardening modulus	716 [MPa]
β	1 [-]
Strain rate	1 [s^{-1}]
D	4000 [s^{-1}]
q	5 [-]

Table 5-3: Chosen parameters for strain rate model

Aside from investigating the strain rate effects by using the full strain rate model, a modified plasticity model will also be introduced as an alternative approach to modeling the strain rate effects. The idea behind the modified plasticity model is that rather than using the static yield stress as input, instead the dynamic yield stress computed based on Equation (5-1) is used. It is a simplified manner of modeling the strain rate effects, but it will be examined whether it is a feasible alternative to the full model, as well as whether the strain rates in Table 5-1 are valid.

The dynamic yield stress is determined by isolating the term in Equation (5-1) as shown below:

$$\frac{\sigma_d}{\sigma_s} = 1 + \left(\frac{\dot{\varepsilon}}{D}\right)^{\frac{1}{q}} \iff \sigma_d = \sigma_s\left(1 + \left(\frac{\dot{\varepsilon}}{D}\right)^{\frac{1}{q}}\right)$$

This gives the results as shown in Table 5-4.

Strain rate $\dot{\varepsilon}$ [s^{-1}]	Dynamic yield stress σ_d [MPa]	Increase in yield stress [%]
1	422.5	19
0.2	404	13.8
0.02	386	8.7

Table 5-4: Dynamic yield stresses

5.2 Strain rate effects on Elasto-Plastic response

Using the strain rate parameters chosen in Table 5-3 and the pressure load of 0.42 MPa gives the deflection history shown in Figure 5-4. Here it is compared with the same model, but without strain rate effects.

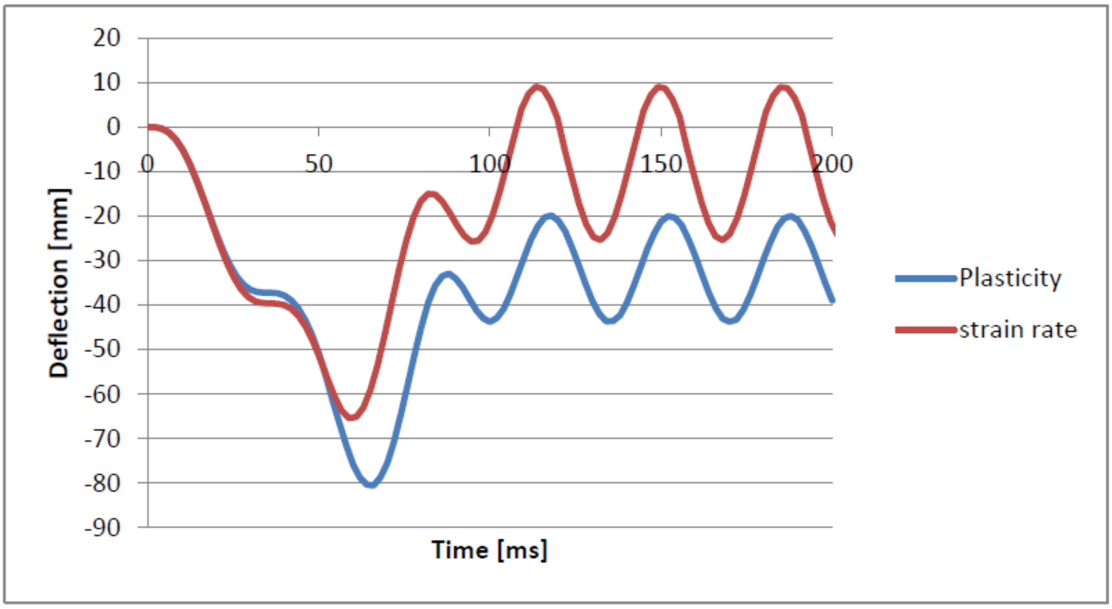

Figure 5-4: Deflection with strain rate effects taken into account

It can be seen that the maximum deflection with strain rates taken into account is not much larger than the linear dynamics response. This indicates that the structure may only have experienced limited plasticity.

To investigate this further, the maximum Von Mise stress over time for the strain rate model is plotted in Figure 5-5.

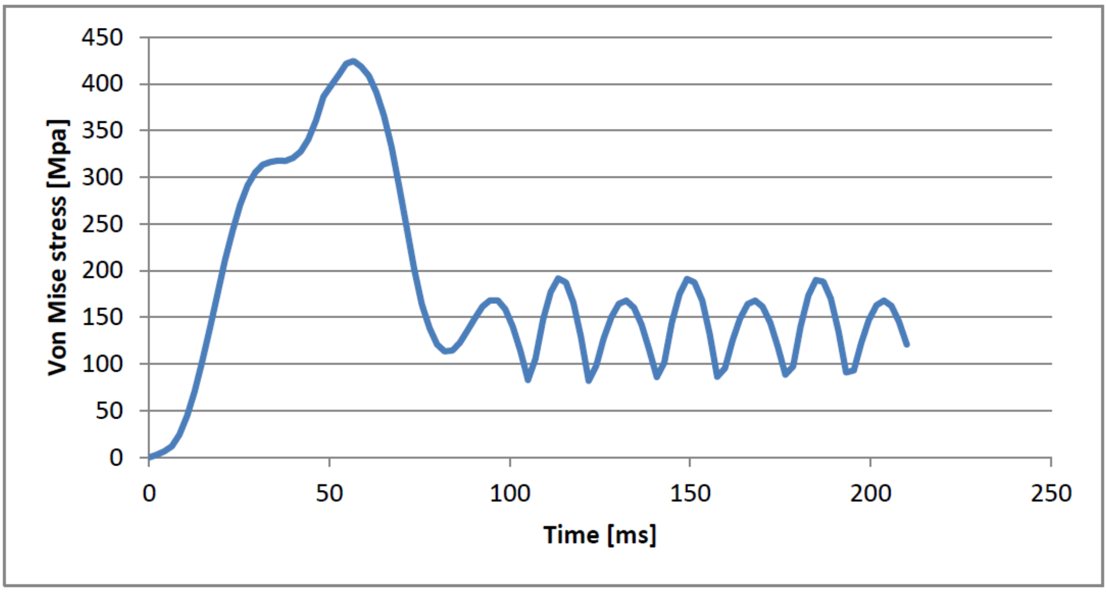

Figure 5-5: Von Mise stress with strain rate effects

It can be observed that the Von Mise stress reaches a maximum of ~420MPa, which is significantly larger than the yield stress of 355 MPa. However this is not the case if you look at the dynamic yield stress from the Cowper-Symonds equation which gives 422.5 MPa as listed in Table 5-4.

Here it is clear that the strain rate effects make it so that the model barely ventures into the plasticity region.

To illustrate the effects at different load levels, a dynamic load deflection curve is introduced. This curve works by taking the peak load of the impulse and plotting it together with the corresponding maximum deflection.

To illustrate this approach, it is first done with the case without strain rate effects and compared to the elastic results in Figure 5-6.

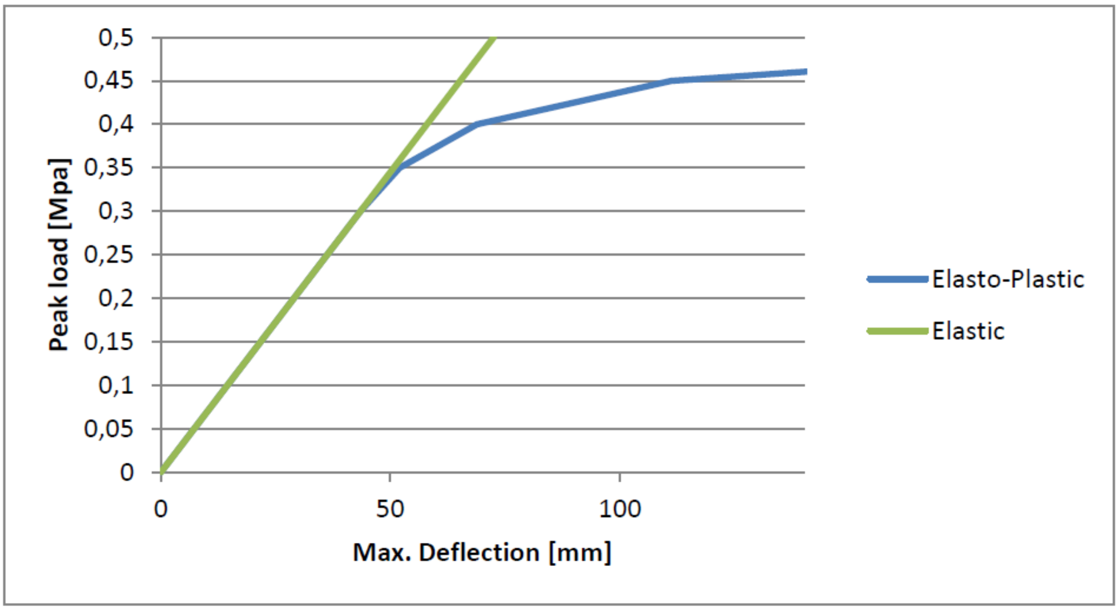

Figure 5-6: Plasticity versus linear elasticity

Here it can be seen that the paths start to diverge at approximately the yield strength of 0.385 MPa, where the deflection greatly increase for the Elasto-Plastic response.

Including the strain rate effects give the red path in Figure 5-7, where it can be seen that the strain rate effects have a significant influence on the response. This influence only grows as the plasticity affects the response more.

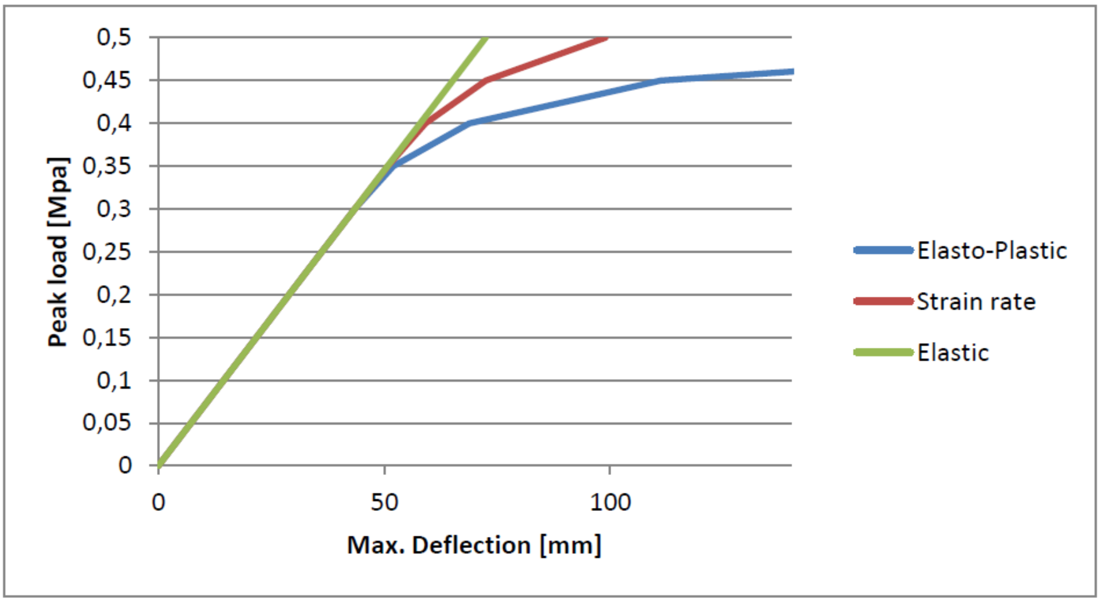

Figure 5-7: The impact of strain rate effects on the Elasto-Plastic response

To compare with the response from the full strain rate effect model, similar plots are constructed using the modified plasticity models. Here the dynamic yield stresses of Table 5-4 are used. These yield stresses are calculated following the recommended strain rates from

[L14], and how well they fit the full response will determine the validity of these recommendations.

As mentioned earlier, according to the cross section classification and the fact that the model experience plastic deflections, it should have a strain rate of $1s^{-1}$. Thus it should be expected that this strain rate will have the best fit with the full strain rate model.

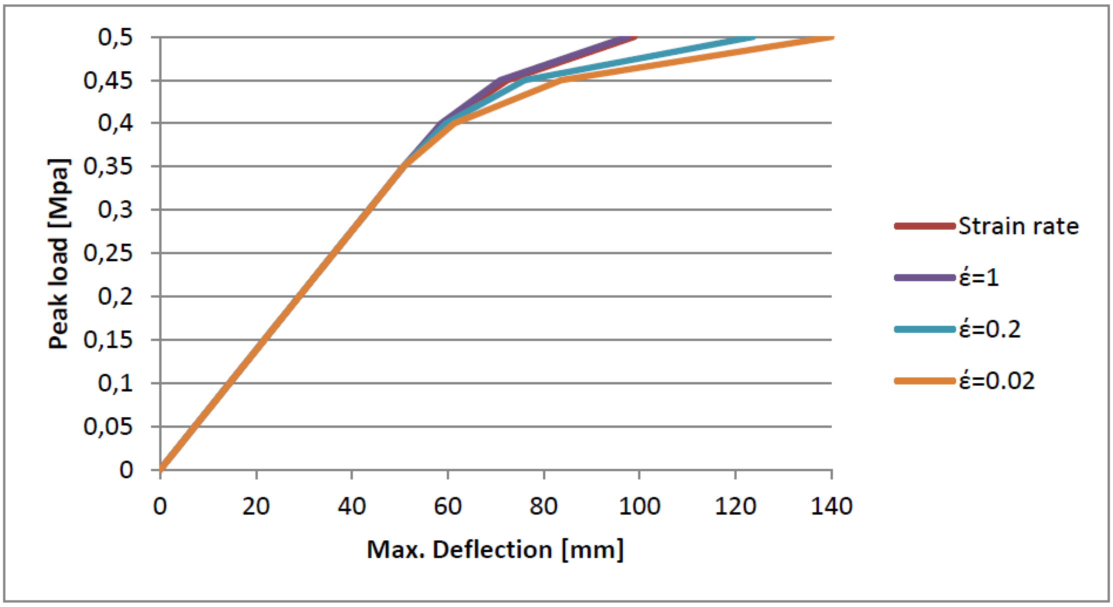

Figure 5-8: Full strain rate model versus modified plasticity models with different yield stresses.

The paths in Figure 5-8 show clearly that the modified plasticity model with a strain rate of $1s^{-1}$ shows the best fit with the full strain rate model. The modified plasticity model does only generate a response close to the full model, but a response that is nearly identical.

The other models show larger plastic deflections, which is to be expected as they have lower yield stresses.

If the peak load is increased even further to 0.55 MPa, the results for the strain rate model and the modified plasticity model starts to diverge. Here, the strain rate model yields a maximum deflection of 150mm while the modified plasticity model yields 167mm.

So it can be concluded that for high amounts of plasticity, the modified plasticity model is insufficient for modeling the strain rate effects on the response. However, it should be noted that while the results diverge, the modified model yields larger deflections and can thus be considered a conservative approach at high levels of plasticity.

5.3 Strain rate effects on dynamic buckling response

As it was observed on Figure 4-15, at a pressure of 0.42 MPa a large response of approximately 1200mm is produced when imperfections are combined with plasticity. Adding the strain rate model in ANSYS LS-DYNA yields the response shown in Figure 5-9. Here it is clear that the strain rate effects have a drastic effect on the response as it is almost halved.

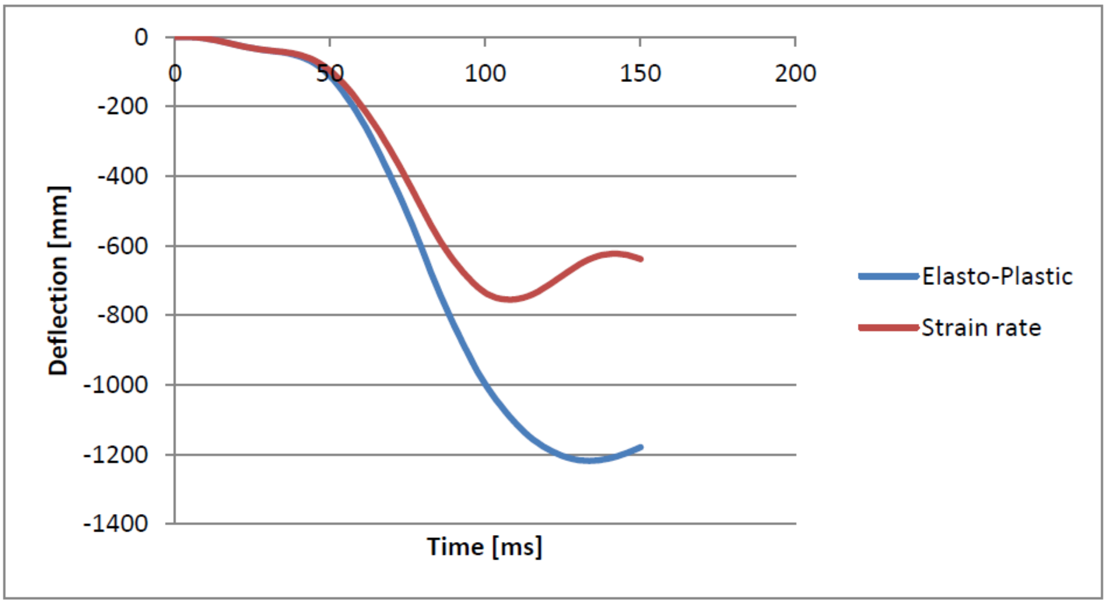

Figure 5-9: Strain rate effects on Elasto-Plastic dynamic buckling response.

Like in Chapter 5.2 dynamic load deflection curves will be developed to illustrate the influence of nonlinearity on the response.

Firstly, to get an idea of when the dynamic buckling occurs, curves are plotted with linear elasticity and geometrically nonlinear elasticity on Figure 5-10.

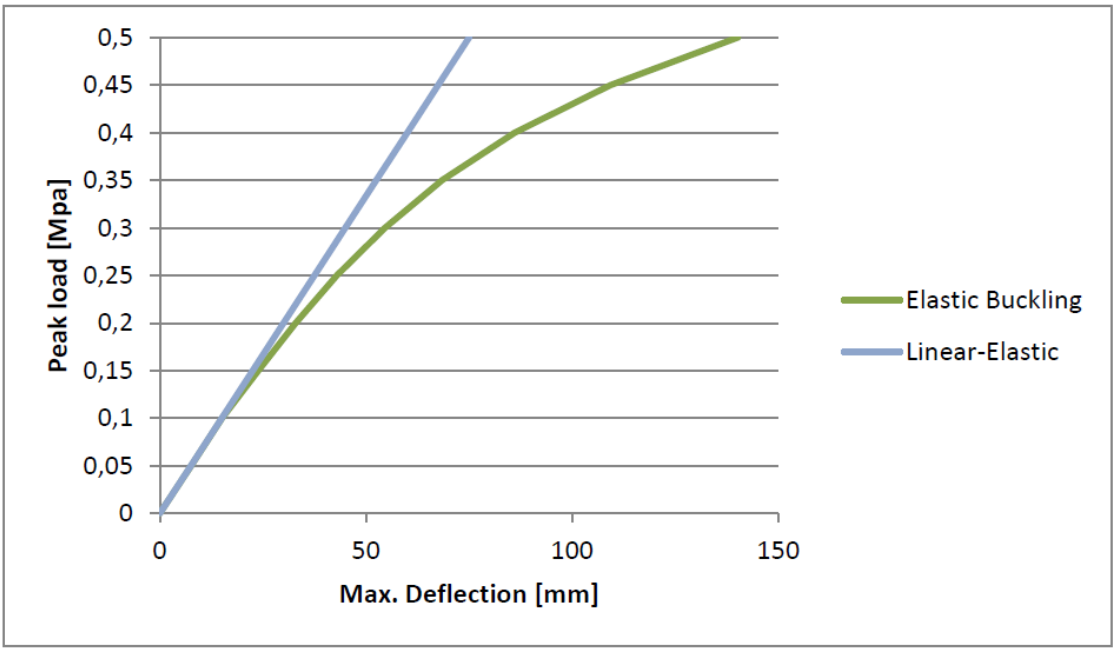

Figure 5-10: Elastic buckling versus linear elasticity.

The dynamic buckling is observed to start at load levels of 0.15-0.2 MPa which is not far from the static buckling load of 0.22 MPa. At a load of 0.5 MPa the elastic buckling gives a deflection nearly twice that of the linear elastic response.

Next the inelastic buckling, where both imperfections and plasticity are included, will be illustrated with a load deflection curve on Figure 5-11. Here is compared with the elastic buckling response, where it is observed that the combination of dynamic buckling and plasticity generates a drastic increase in the maximum deflection. At a load of 0.4 MPa it already reaches a deflection of a 1000mm, which is roughly 12 times that of the elastic deflection.

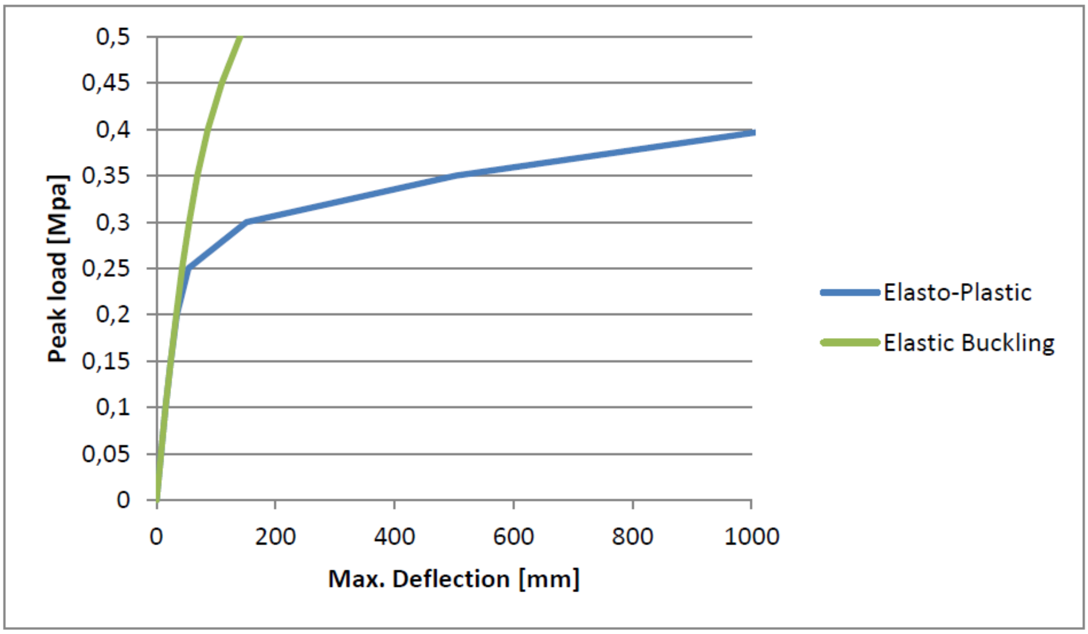

Figure 5-11: Elastic buckling versus Elasto-Plastic buckling

Like it was shown in Figure 5-9, including strain rate effects in the model can drastically reduce the maximum deflection, and to examine how much, Figure 5-12 has been produced.

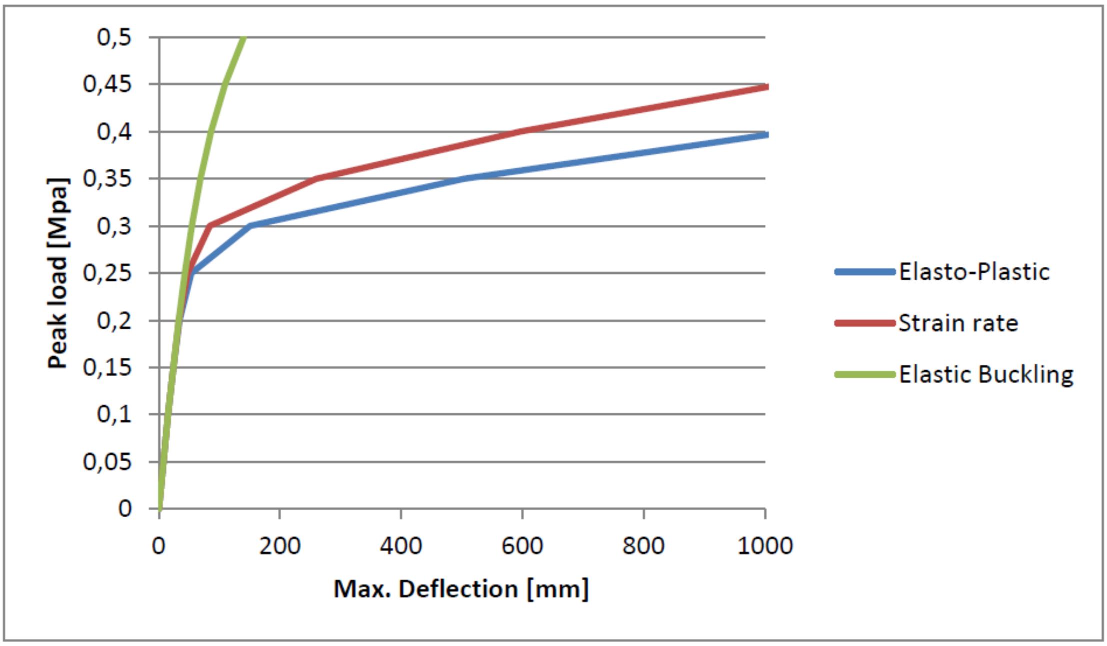

Figure 5-12: Impact of strain rate effects on Elasto-Plastic buckling response

Here it can be seen that the strain rate effects roughly halves the response, but the maximum response is still much larger than elastic buckling or responses without imperfections.

Once again, the analyses will be carried out with the modified plasticity models as well, to observe how well they hold up against the full strain rate model. The results are displayed on Figure 5-13.

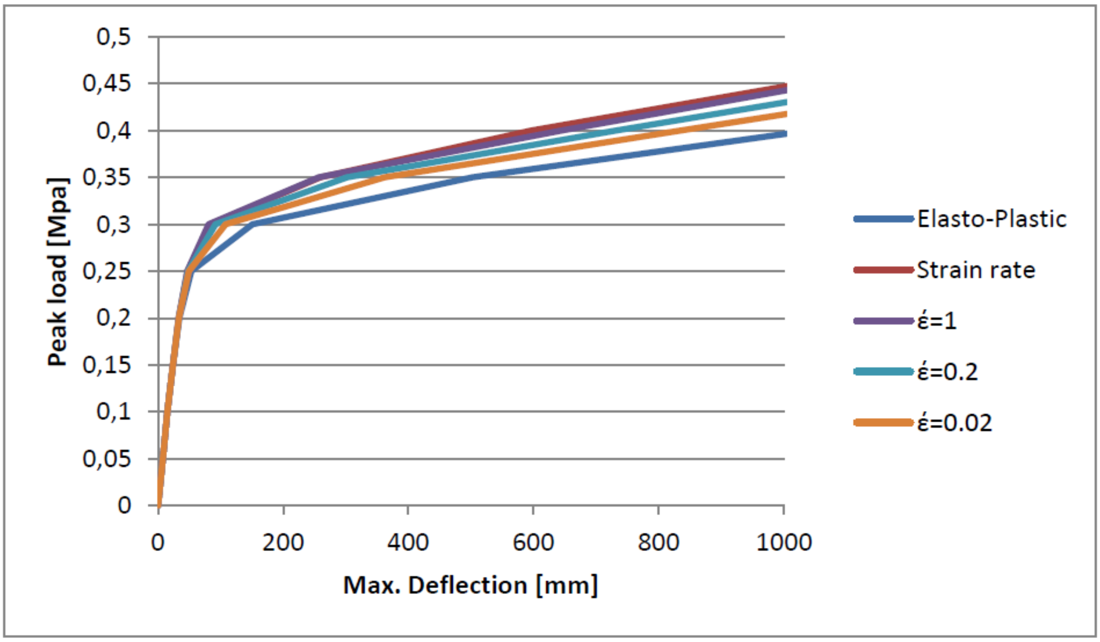

Figure 5-13: Full strain rate model with imperfections versus modified plasticity models with different yield stresses.

Like in Figure 5-8, the modified plasticity with a strain rate of $1s^{-1}$ matches well with the full strain rate model. It is observed that divergence happen at an earlier load level (it is too small to be observed on the figure, but at the load of level of 0.4MPa there is a difference of 50mm) than in Figure 5-8, but this is likely a consequence of the dynamic buckling. Because of the buckling, the cross section deforms and loses strength, thus making plasticity occur at lower load levels.

5.4 Partial conclusion

Strain rate effects were implemented in the ANSYS LS-DYNA model, using the Cowper-Symonds model, and it was found that the inclusion of strain rate effects could reduce the plastic response considerably. A modified plasticity model was introduced where the initial yield stress was manually increased, and it was found to produce responses close to that of the full strain rate model. It was also determined that the recommended strain rates in standards, based on cross section classes, produced matching results through the modified plasticity results.

Further investigation into the plastic strain development in transient analyses ought to be done and then followed by observations on the influence of strain rate effects on the plastic strain levels. In this process element death ought to be included to simulate rupture of the structure when certain plastic strain limits are reached.

6 MODELING OF PLASTIC STRAINS

The question of when a structure fails, i.e. lose its structural integrity, has always been a source of debate as predicting it has proven to very difficult. One of the most common ways to estimate this point of failure has been to introduce the concept of a failure plastic strain, an ultimate strain that signals the failure of the structure.

However plastic strains have proven themselves problematic to model in numerical models such as the Finite Element method. The challenges involved include the ever returning problem of singularities in a FEM model as well as convergence problems.

Because of this research in the matter has been conducted in works such as [L11] and [L13]. The purpose of this chapter is to investigate the development of plastic strain in the shell element I-profile model introduced in this thesis. The FEM model results will be compared to approaches in standards and also compared with a solid element model. Additionally, a proposal for converting the shell plastic strains into a converging strain introduced in [L11] will be applied to the I-profile and the results evaluated.

6.1 Approaches in standards

In this subsection, approaches in the steel Eurocode [L2], COWI [L4], the manual for the program RONJA [L5] and the offshore oriented design code NORSOK [L6]. The NORSOK approach is also the one used in the DNV standard [L7].

All standards approaches assume fully developed plastic hinges.

6.1.1 DS/EN 1993-1-1

In the Eurocode, development of plastic hinges is tied to the cross section class, and only class 1 and 2 cross sections are actually allowed to have plasticity. And among those two, only class 1 cross sections are assumed to have the rotational capacity to fully develop yield hinges. This limitation tie in with the assumption that no local or lateral buckling will occur during the formation of the yield hinge.

The Eurocode allows an ultimate strain of for class 1 cross sections of:

$$\varepsilon_u = 10\varepsilon_y \tag{6-1}$$

The length of the plastic hinge is based on the moment capacity on the cross section. The hinge occurs when the plastic moment capacity M_{pl} is reached at any point in the beam. The plasticity is then assumed to happen where the bending moments are in between the plastic moment capacity and the elastic moment capacity. This is because the plastic moment capacity carries the assumption that the cross section is fully plastic, i.e. fully developed plastic hinge, while the elastic capacity is equal to first fiber yield. This concept is illustrated on Figure 6-8.

The calculations are then aimed at finding the total deflection when the plastic hinge is formed by using trigonometric relations.

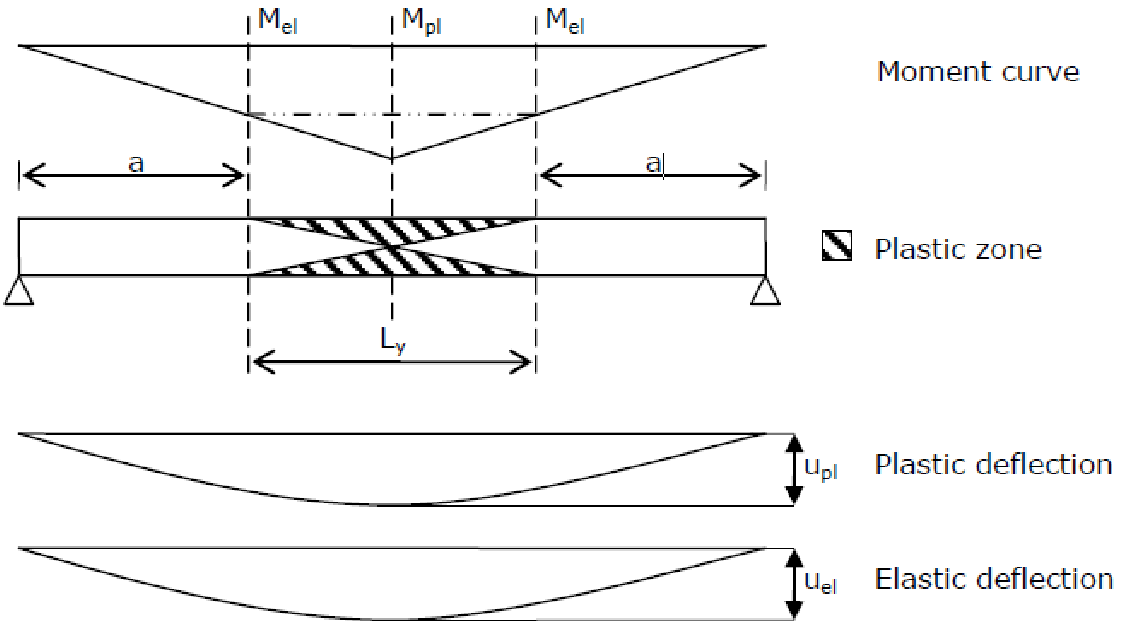

Figure 6-1: Illustration of the principle behind determining the plastic hinge length [L13].

As shown on Figure 6-8, the length of the plastic hinge is equal to:

$$L_{ph} = L - 2a \tag{6-2}$$

Where a is the distance from support to plastic hinge

The distance a is found by using simple statics to find the moment curve.

The plastic rotation in the hinge is given by:

$$\phi_{pl} = \frac{L_{ph}}{2z}\varepsilon_u = \frac{L_{ph}}{h_{tot}}\varepsilon_u \tag{6-3}$$

The corresponding plastic deflection is

$$u_{pl} = \frac{\phi_{pl}}{2}\frac{L_{ph}}{2} \tag{6-4}$$

The total deflection is found by adding the elastic contribution

$$u_t = u_{el} + u_{pl} \tag{6-5}$$

Substituting in the Bernoulli-Euler expression for elastic deflection and Equation (6-3) and (6-4) yields the following expression for the total deflection:

$$u_t = \frac{\frac{L_{ph}}{2z}\varepsilon_u}{2}\frac{L_{ph}}{2} + \frac{5}{384}\frac{PL^4}{EI} \tag{6-6}$$

Where P is the yield load

With this the total deflection as a function of the ultimate strain can be plotted as shown in Figure 6-2.

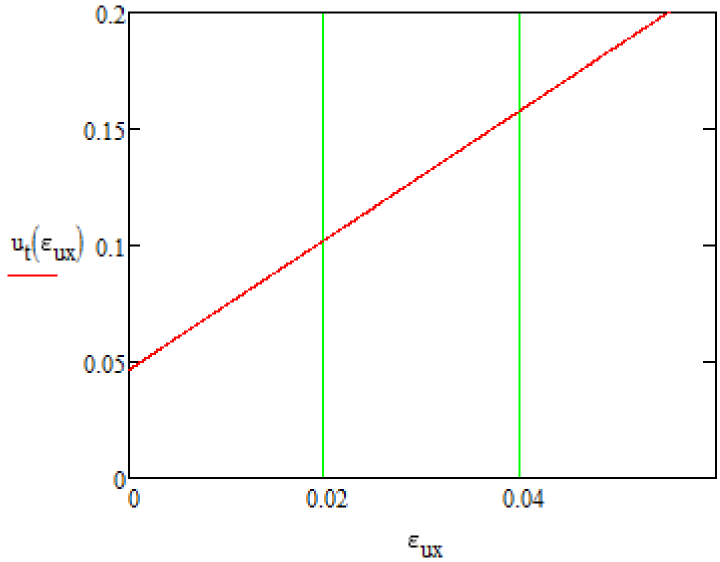

Figure 6-2: Displacement as a function of plastic strain (Eurocode)

From this figure the plastic strain can be determined based on the total deflection.

6.1.2 COWI

Rather than relying on cross section classes, COWI simply assumes that the structure is allowed to have a plastic hinge. The ultimate strain used in the COWI guidelines is set to 15% for materials with a yield stress around 355MPa. The max allowable strain, the critical strain, is however only allowed to be half the ultimate strain:

$$\varepsilon_{cr} = \frac{1}{2}\varepsilon_u \tag{6-7}$$

The approach proposed by COWI uses the same principles for the plastic hinge length as the Eurocode approach. It does however, have an upper limit on the plastic hinge length. That limit is equal to the height of the cross section for open profiles and 1.5 times the height for closed cross sections:

$$L_{ph.open} \leq 1.0 \cdot h_{tot} \quad ; \quad L_{ph.closed} \leq 1.5 \cdot h_{tot} \tag{6-8}$$

The COWI approach includes 15% (based on the ultimate strain) strain hardening by increasing the plastic moment capacity as shown below:

$$M_{pl} = W_{pl}f_y + W_{el}0.15f_y \tag{6-9}$$

The plastic rotation in the hinge is given by:

$$\phi_{pl} = \frac{2\varepsilon_{cr}L_{ph}}{h_{tot}} = \frac{\varepsilon_u L_{ph}}{h_{tot}} \tag{6-10}$$

And the plastic deflection is:

$$u_{pl} = \varepsilon_{cr}L_{ph} = \frac{1}{2}\varepsilon_u L_{ph} \tag{6-11}$$

Thus the total deflection is:

$$u_t = \frac{1}{2}\varepsilon_u L_{ph} + u_{el} \tag{6-12}$$

Plotting the relation between total deflection and plastic strain gives the graph in Figure 6-3.

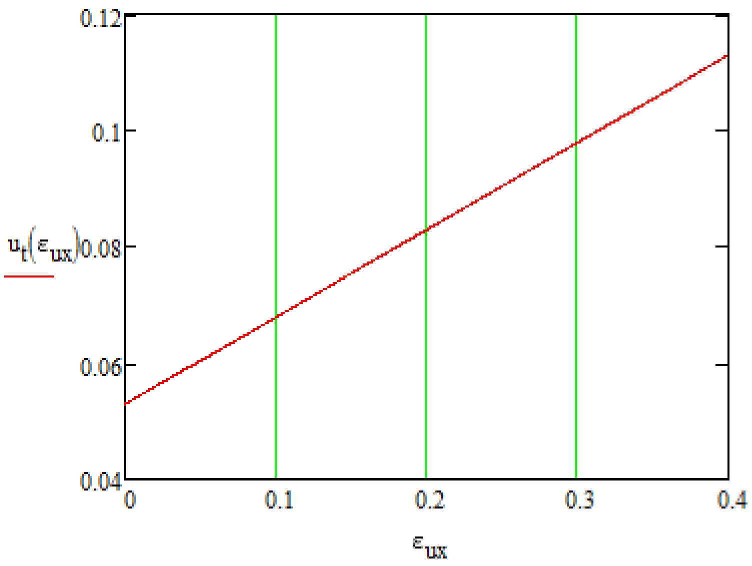

Figure 6-3: Displacement as a function of plastic strain (COWI)

Like in Chapter 6.1.1, can be used to determine the plastic strain based on a given deflection.

6.1.3 RONJA

The program RONJA (Rambøll Offshore Nonlinear Jacket Analysis) developed by Rambøll also has its own approach to the calculation of plastic strain and development of plastic hinges.

RONJA gives two approaches to the development of plastic strain, one with and one without strain hardening.

The strain limit in RONJA varies, depending on the situation from the ultimate strain of 15% to 5% to the critical strain defined in Chapter 6.1.4. For this project the material limit of 15% is used to make it comparable.

The plastic hinge length for the case without strain hardening is identical to the upper limit for COWI method i.e. equal to the height for I-profiles. As it is independent of the plastic strain, the relation between deflection and plastic strain is linear.

If strain hardening is included, the plastic hinge length is given by the following expression:

$$L_{ph} = \frac{3}{4}L\left(1 - \frac{1}{1 + \frac{E\varepsilon_u}{f_y}H\frac{W_{el}f_y}{M_{pl}}}\right) \tag{6-13}$$

Because this formulation is dependent on the plastic strain, the relation between deflection and plastic strain is nonlinear.

In RONJA, the critical strain is allowed to be twice the ultimate strain:

$$\varepsilon_{cr} = 2\varepsilon_u \tag{6-14}$$

With this, the rotation becomes

$$\phi_{pl} = \frac{\varepsilon_{cr}L_{ph}}{h_{tot}} = \frac{2\varepsilon_u L_{ph}}{h_{tot}} \tag{6-15}$$

And the corresponding plastic deflection:

$$u_{pl} = \phi_{pl}\frac{h_{tot}}{2} = \varepsilon_u L_{ph} \tag{6-16}$$

The total deflection is then:

$$u_t = \varepsilon_u L_{ph} + u_{el} \tag{6-17}$$

Like with the Eurocode and COWI approaches, this gives a linear relation between total deflection and plastic strain, for the case without strain hardening, as depicted in Figure 6-4

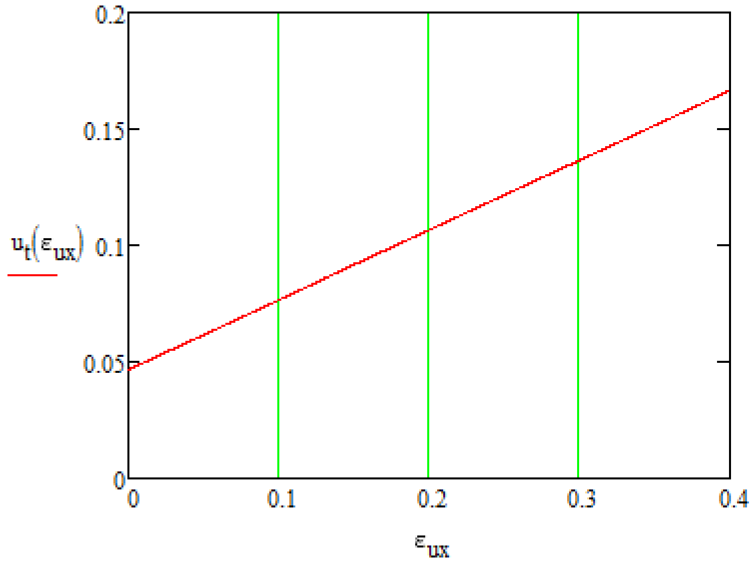

Figure 6-4: Displacement as a function of plastic strain (RONJA without strain hardening)

If the definition for the plastic hinge length becomes as in Equation (6-13), the relation between total deflection and plastic strain becomes nonlinear as shown on Figure 6-5.

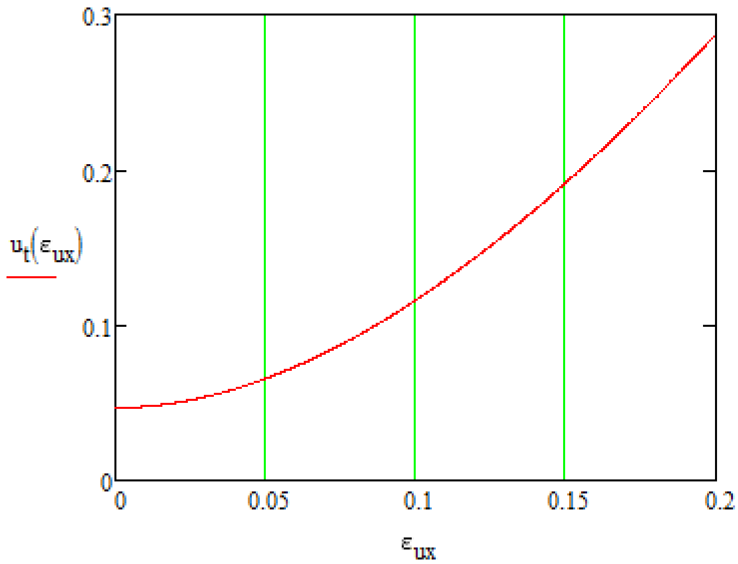

Figure 6-5: Displacement as a function of plastic strain (RONJA with strain hardening)

In both cases, the plastic strain is, like in the previous methods, by applying the total deflection of the beam and reading the corresponding plastic strain.

6.1.4 NORSOK

The ULTIGUIDE [L9], which is part of the foundation for offshore standards like NORSOK, states that as long as there are no cracks present in the structure, it can develop the strain levels necessary to generate a fully developed plastic hinge

For ductile steel the NORSOK code recommends a material strain limit of 15-20%, which is similar to the strain limits given by COWI and RONJA. While the material limit is well suited for beams with good ductility, for beams with welded connections a nominal strain of 5% is recommended in [L9].

NORSOK defines the critical strain as:

$$\varepsilon_{cr} = 0.02 + 0.65\frac{t_f}{L_{ph}} \tag{6-18}$$

This can be rewritten into the following expression so that the plastic hinge length becomes a function of the critical strain:

$$L_{ph}(\varepsilon_{cr}) = \frac{0.65t_f}{\varepsilon_{cr} - 0.02} \tag{6-19}$$

Additionally, the NORSOK standard gives a lower limit on the plastic hinge of 5 times the flange thickness.

NORSOK approaches calculation of plastic strain differently by directly defining the deformation as which tensile rupture will occur [L6]:

$$w_{cr} = h\frac{c_1}{2c_f}\left(\sqrt{1 + \frac{4c_w c_f \varepsilon_u}{c_1}} - 1\right) \tag{6-20}$$

Where

c_1 is a constraint factor which is 1 for a simply supported beam

c_f is a axial flexibility factor given by

$c_f = \left(\frac{\sqrt{c}}{1+\sqrt{c}}\right)^2$

c_w is a displacement factor given by

$$c_w = \frac{1}{c_1}\left[c_{lp}\left(1 - \frac{1}{3}c_{lp}\right) + 4\left(1 - \frac{W_{el}}{W_{pl}}\right)\frac{\varepsilon_y}{\varepsilon_u}\right]\left(\frac{\kappa L}{h}\right)^2 \tag{6-21}$$

The factor c is the non dimensional spring stiffness expressed by:

$$c = \frac{4c_1 K {w_c}^2}{A} \tag{6-22}$$

Where

w_c is the characteristic deformation:

$$w_c = \frac{1.2W_{pl}}{A} \tag{6-23}$$

K is the equivalent axial stiffness defined by:

$$\frac{1}{K} = \frac{1}{K_{node}} + \frac{L}{2EA} \tag{6-24}$$

K_{node} is the axial stiffness of the end node with the considered beam removed. For a simply supported beam it becomes the axial stiffness of the beam. The principle behind the axial stiffness can be seen on Figure 6-6.

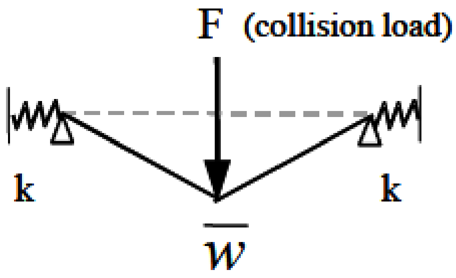

Figure 6-6: Collision load sketch [L6]

c_{lp} is the plastic zone length factor

$$c_{lp} = \frac{\left(\frac{\varepsilon_u}{\varepsilon_y} - 1\right)\frac{W_{el}}{W_{pl}}H}{\left(\frac{\varepsilon_u}{\varepsilon_y} - 1\right)\frac{W_{el}}{W_{pl}}H + 1} \tag{6-25}$$

κL is the smallest distance to the point of collision on Figure 6-6. For a distributed load, the point of collision can be assumed to be in the middle so $\kappa L = 0.5L$

Plotting Equation (6-19) and Equation (6-20) together gives Figure 6-7.

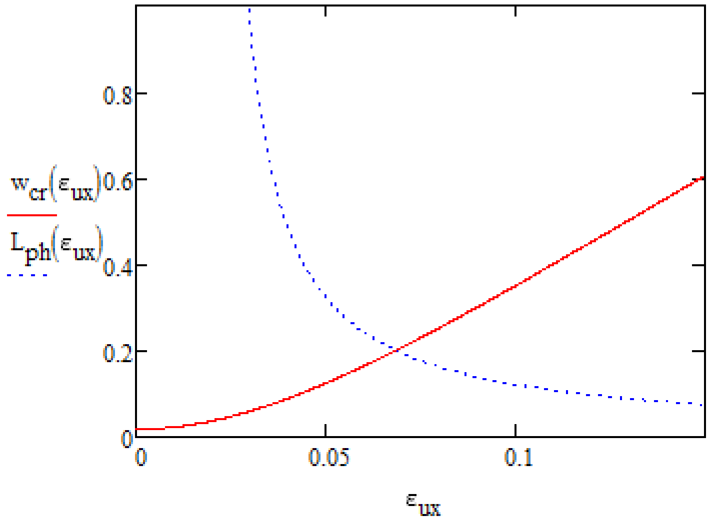

Figure 6-7: Displacement and plastic hinge length as a function of plastic strain (NORSOK)

To determine the plastic strain, the total deflection is found on the graph and the corresponding plastic strain is read. After the plastic strain is determined, the corresponding plastic hinge length can be found.

6.2 Plastic strain in ANSYS

The ANSYS analysis is performed by doing a nonlinear static analysis of the I-profile model presented in earlier chapters. The chosen load level is the one where the plastic hinge is fully formed, i.e plastic strains exists throughout the cross section. This gives a contour plot of the plastic strains like in Figure 6-8. Though the model does not appear to have a fully formed plastic hinge, this is because the smallest plastic strains are masked because they lie in the interval 0-0.54*10^{-3}(se contour band in Figure 6-8).

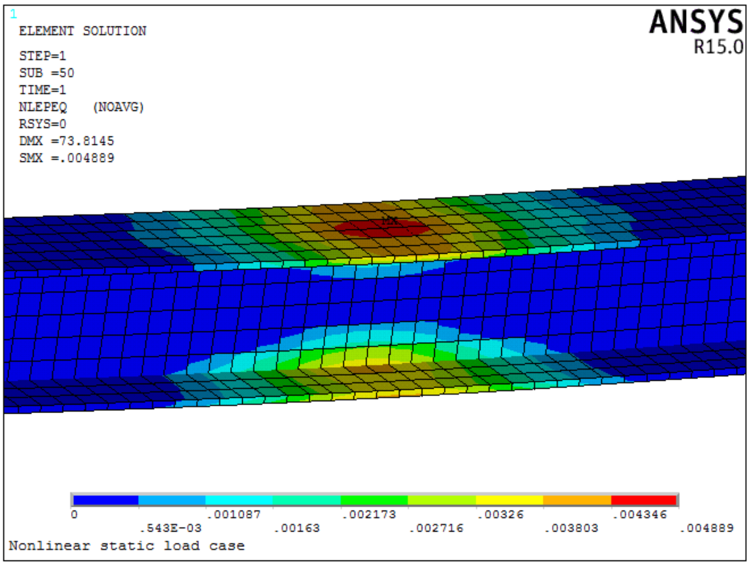

Figure 6-8: Plastic hinge in shell model.

Doing convergence on the shell model for the deflection, plastic strain and plastic hinge length gives the results listed in Table 6-1

Element size [mm]	Deflection [mm]	Plastic strain [%]	Plastic hinge length [mm]
150	63.79	0.3521	1800
100	69.01	0.283	1800
50	73.8	0.4889	1800
30	74.77	0.5772	1770

Table 6-1: Convergence of plastic hinge for shell model

It is clear that while the hinge length converges quickly to 1770mm, and the deflection converges slowly to roughly 75mm, the plastic strain does not appear to converge.

To compare with the shell model, a solid model with comparable boundary conditions is made and converged similarly. The solid model converges to a plastic strain of 0.64% and a plastic hinge length of 1800mm.

Because the deflection of the shell model is 75mm, this deflection will be used as the total deflection in the norm calculations.

The resulting plastic strains and plastic hinge lengths are listed together with the ANSYS results in Table 6-2.

	Strain limit [%]	Plastic strain [%]	Plastic hinge length [mm]
ANSYS (shell)	15.0	0.5772	1770
ANSYS (solid)	15.0	0.6449	1800
Eurocode	0.167	1.0	2086
COWI	15.0	15.0	300
RONJA	15.0	9.5	300
RONJA (with strain hardening)	15.0	6.2	457
NORSOK	15.0	3.55	629

Table 6-2: Comparison of plastic hinge results

For the ANSYS results it can be seen that there are disparities in the plastic strains, while the plastic hinge length appears to converge nicely.

It is clear that internally, the Eurocode approach exceeds its own strain limit of 10 times the elastic yield strain, while the COWI plastic strain borders the material limit of 15%.

For the RONJA methods, plastic strain is kept within the material limit, while it is observed that the method without strain hardening gives a higher plastic strain. This is likely because of the difference in the plastic hinge length, where the method without strain hardening is simply given as the cross section height, while the method with strain hardening yields a higher value for the hinge length. Because of the smaller hinge length, the plastic strain is focused on a smaller area, so it is expected that it should give a higher plastic strain.

Disparities in plastic hinge length also explain why the Eurocode gives a plastic strain much lower than the other hand calculation methods. With this in mind, the Eurocode matches somewhat with the ANSYS results as it has comparable plastic hinge length and the closest plastic strain.

Generally it can be seen that methods where the plastic hinge length is determined yields much higher values than methods with an upper limit of the cross sectional height. This might be related to the fact the chosen cross section has width that is equal to the height, while the approaches in standards are more intended for profiles with a cross sectional height that is somewhat larger than the width.

6.2.1 Weighting methods

In this subsection, a conversion method, where the plastic strains of the shell model are weighted, will be applied to the I-profile model and the results evaluated.

The plastic strains in the solid and shell models are not far apart so weighting the plastic strains in the shell model can be argued to be negligible. Nonetheless the weighting will be carried out in order to test its functionality for the case of an I-profile. The weighting method used is the following expression:

$$\varepsilon_{weighted} = \frac{\sum(\varepsilon_{pl} \cdot l_e)}{l_{ph}} \tag{6-26}$$

The basic idea is that the total plastic strain in the plastic hinge ($\sum(\varepsilon_{pl} \cdot l_e)$) will converge early, despite the model not describing the plastic hinge completely. Then by dividing with the plastic hinge length, the plastic strains will be distributed like on Figure 6-9.

Figure 6-9: Illustration of the concept behind the weighting method

The results for the conversion are listed in Table 6-3.

Element size [mm]	$\sum(\varepsilon_{pl} \cdot l_e)$ [mm]	$\varepsilon_{weighted}$ [%]
150	7.785	0.4325
100	13.89	0.7717
50	33.785	1.8769
30	38.07	2.1508

Table 6-3: Weighted plastic strains.

It is seen that the weighted plastic strains do not appear to converge any faster than the original plastic strains. This method was originally developed for a structure consisting of only shell elements experiencing out of plane forces and displacements and assumes that the plastic hinge length is roughly equal to the cross sectional height. The I-profile model has the majority of the plastic hinge described by shell elements loaded and deformed in plane, and the plastic hinge length is significantly higher than the assumed length.

The fact that the majority of the plastic hinge is described by shell elements loaded and deformed in plane may also be the reason why the plastic strains are much closer to the solid model results, than the model in [L11]. Another factor is likely the fact that the method assumes that the hinge length is equal to the element thickness in [L11], which for an I-profile would be the cross sectional height. Since the ANSYS results, both shell and solid, gives a plastic hinge length that is much larger, the assumption cannot be said to be valid.

6.3 Partial conclusion

It was found that plastic hinge length varies wildly depending on the approach used. The Eurocode approach gives plastic hinge lengths comparable to ANSYS results, while the other methods give hinge lengths between 1 to 2 times the height of the cross section. This is also reflected in them giving higher plastic strains than ANSYS, thus making them more conservative.

The shell and solid models gave results for plastic strains that are not too far apart, though the solid model results are higher by around 10%. The convergence method used was found to produce unreliable results.

Further modeling for profiles with different width to height ratios and different hardening models ought to be performed to see whether the trends in this thesis are consistent. Additionally, gradual rupture by means of element death ought to be implemented to pursue more accurate rupture mechanics.

7 POST BUCKLING ANALYSIS OF PLATE

Slender plates often tend to experience local buckling before yielding becomes an issue. Because of this there is great interest in developing methods to describe the post buckling state that takes place after local buckling occurs. Without such methods, analyses are limited by the critical local buckling load, and in systems such as offshore modules, this would mean that the critical buckling load becomes the plates bearing capacity.

Finite Element programs can simulate the post buckling state with any combination of boundary conditions, but are time consuming to setup and often require intricate knowledge of the Finite Element method to obtain reliable results. In the case of structures where the plate is only one part of a larger system, the analysis becomes even more time consuming.

Formulations exist, such as the Eurocode approach presented in Chapter 3.3, that predicts the post critical bearing capacity, the load at which yielding occurs, with reasonable accuracy. However these formulations do not describe the post buckling equilibrium path and the development of deformations and stresses.

In very slender plates in particularly this issue becomes more pronounced, as illustrated on Figure 3-26 in Chapter 3.3, even the post critical bearing capacity formulations become inaccurate.

Because of these issues, there have been many studies dedicated to solving this problem and establishing analytical or semi analytical methods for describing the post buckling behavior of plates.

This chapter is a study of different methods developed throughout the years, where they will be evaluated based on accuracy, complexity and versatility. There exist studies for many different boundary conditions ranging from simply supported plates to clamped plates to stiffened plates and varying load combinations as well.

This study will focus on the case of simply supported plates in pure uniaxial compression as presented earlier in Chapter 2.2. The study is dedicated mostly to approaches to the static post buckling case, as they are the most numerous, but will also look into solutions to the dynamic post buckling case.

Williams & Walker [L17] and Ferreira & Virtuoso [L19] both offer solutions to the static post buckling and also offer examples with results. They will be introduced and evaluated in Chapter 7.1 and 7.2 and the results compared with ANSYS models using the boundary conditions introduced in Chapter 3.3.

In chapter 7.3 other suggestions to solve the static post buckling case will be reviewed, such as Byklum & Amdahl [L20], while in Chapter 7.4 solutions to the dynamic post buckling case, such as Petry & Fahlbusch [L22] will be reviewed similarly.

7.1 D.G. Williams and A.C Walker

In the paper 'Explicit solutions for the design of initially deformed plates subject to compression' simplified explicit solutions for plates subjected to compressive force are presented.

The solution is given by the following equations:

$$\eta^{\frac{1}{2}} = A\varphi + B\varphi^3 \tag{7-1}$$

Where

η is

$$\left(\frac{w}{t}\right)^2 - \left(\frac{w_0}{t}\right)^2$$

W is total out of plane displacement

w_0 is the initial imperfection

t is the thickness of the plate

A and B are coefficients based on numerical analyses

$$\varphi = \left(\frac{P}{P_{cr}} - 1 + \frac{w_0}{w}\right)^{\frac{1}{2}}$$

The ratio between loads is equal to the ratio between stresses so:

$$\frac{P}{P_{cr}} = \frac{\sigma_{xav}}{\sigma_{xcr}}$$

Similar expressions are given for the axial shortening, membrane stresses and moments.

The central part of this method is the coefficients A and B. These coefficients are derived by combining a numerical method like FEM with a perturbation method where parameters are expanded in a power series. This allows simple calculations of the otherwise complex nonlinear problem that is post buckling behavior. The drawback is that new sets of coefficients need to be derived for each specific set of boundary conditions and geometric relations. Additionally a set of coefficients are needed for each parameter such as deflection and membrane stress.

The following example will be used to illustrate how the method works.

If we take a simply supported quadratic plate in pure uniaxial compression with the following geometry: a width a and height b of 99.8mm and a thickness t of 0.7mm. The linear elastic material parameters are the standard $E = 210000MPa$ and poisons ratio of 0.3. Lastly the imperfection is assumed to be equal to the thickness eg. 0.7mm.

The critical buckling load is given by:

$$N_{cr} = \frac{\pi^2 D}{a^2}\left(m + \frac{1}{m}\frac{a^2}{b^2}\right)^2 = 2609N$$

Where m=1 as the plate is quadratic.

The corresponding critical stress is $\frac{2609N}{99.8mm \cdot 0.7mm} 37.35MPa$

Computing the nonlinear buckling analysis in ANSYS gives the load-deflection curve shown in Figure 7-1.

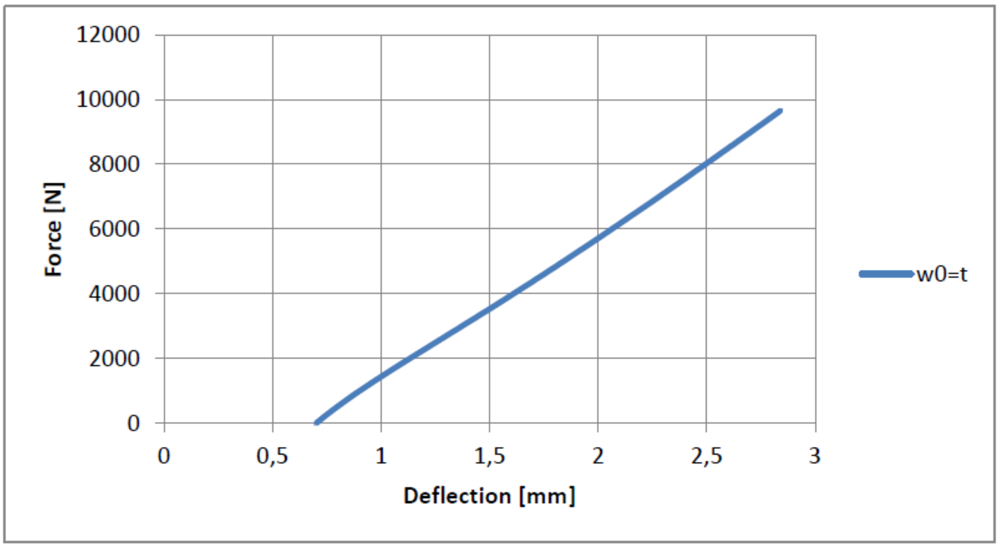

Figure 7-1: Load deflection curve of example

If we take a load of 4000N, we get a corresponding deflection of 1.59mm.

To calculate the deflection by the papers method, first the average compressive stress needs to be computed:

$$\sigma_{xav} = \frac{4000N}{99.8mm \cdot 0.7mm} = 57.3MPa$$

The ratio between applied and critical load is then found:

$$\frac{P}{P_{cr}} = \frac{\sigma_{xav}}{\sigma_{xcr}} = \frac{57.3MPa}{37.35MPa} = 1.533$$

The out of plane is found through Equation (7-1). The ratio $\frac{w}{t}$ is unknown so an iterative approach is needed where the ratio will be estimated until both the left hand side and the right hand side of the equation is approximately equal. For a quadratic plate in pure compression, the coefficients are $A = 2.157$ and $B = 0.010$.

First guess is $\frac{w}{t} = 2$

This gives a deflection of $w = 2t = 1.4mm$

The parameter φ is then $\varphi = \left(1.533 - 1 + \frac{0.7mm}{1.4mm}\right)^{\frac{1}{2}} = 1.016$

The left hand side: $\left\{(2)^2 - \left(\frac{0.7mm}{0.7mm}\right)^2\right\}^{\frac{1}{2}} = 1.732$

The right hand side: $2.157 \cdot (1.016) + 0.010 \cdot (1.016)^3 = 2.203$

$$1.732 \neq 2.203$$

Next is $\frac{w}{t} = 2.2$. This gives

$$1.96 \neq 2.153$$

Next is $\frac{w}{t} = 2.3$. This gives

$$2.071 \neq 2.131$$

And lastly is $\frac{w}{t} = 2.35$. This gives

$$2.127 \approx 2.121$$

The corresponding out of plane deflection is $w = 2.35t = 1.645mm$

Compared to the ANSYS result of 1.59mm, it is rather close.

7.1.1 ROSMANIT & BAKKER

In 2008 ROSMANIT & BAKKER [L18] made a paper focused on the post buckling behavior of square plates. They gathered a number of existing analytical formulations and attempted to simplify them for easier use.

These solutions include one where small deflections are assumed and the post-buckling behavior is governed by Marguerre's equations. Additionally a large deflection solution is presented which is a modified version of the solution proposed by Williams & Walker [L17].

The small-deflection solution is defined by:

$$\frac{F}{F_{cr}} = \frac{\sigma_{xav}}{\sigma_{cr}} = \left(1 - \frac{w_0}{w}\right) + A_F\eta \qquad with \;\; A_F = \frac{A}{K}\frac{E^*}{E} \tag{7-2}$$

$$\frac{u}{u_{cr}} = \frac{\varepsilon_{xav}}{\varepsilon_{cr}} = \left(1 - \frac{w_0}{w}\right) + A_u\eta \quad with \;\; A_F = \frac{A}{K} \tag{7-3}$$

$$\frac{\sigma_{xA}}{\sigma_{cr}} = \left(1 - \frac{w_0}{w}\right) + A_{\sigma xA}\eta \qquad with \;\; A_F = \frac{\frac{A}{K}\frac{E^*}{E}}{\frac{\partial\sigma_{xav}}{\partial\sigma_{xA}}} \tag{7-4}$$

Where the subscript A refer to location A on Figure 7-2. The remaining nomenclature is identical to Williams & Walker.

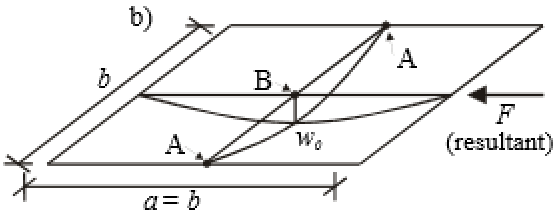

Figure 7-2: Initial imperfection, load, measures and locations of points A and B [L18]

The coefficients for the solution are given in Table 7-1.

K	A	$\frac{E^*}{E}$	$\frac{\partial\sigma_{xav}}{\partial\sigma_{xA}}$
4	2.31	0.408	0.26

Table 7-1: Rhode coefficients [L18]

They found that the large deflection solution proposed by Williams & Walker could be rewritten so that it would be of the same form as Equation (7-2) - (7-4), with the only difference being the addition of the term $B\eta^2$ on the right hand side. This results in the original coefficients being modified so we get the following coefficients for the deflection of a quadratic plate.

	A	B
Original	2.157	0.010
Modified	0.2149	$0.4283 \cdot 10^{-3}$

Table 7-2: Williams & Walker coefficients

With this modification the results can now be obtained directly, rather than through iterations.

To compare these solutions to an ANSYS model, the same example as in Chapter 7.1, will be used. The comparison will be made by plotting the equilibrium paths, which are normalized by the critical load and thickness.

To test the sensitivity to imperfections, analyses are carried out with three different levels of imperfection: a small imperfection of 0.01 times the thickness, a medium imperfection equal to the thickness and finally a large one equal to twice the thickness. The results are depicted on Figure 7-3.

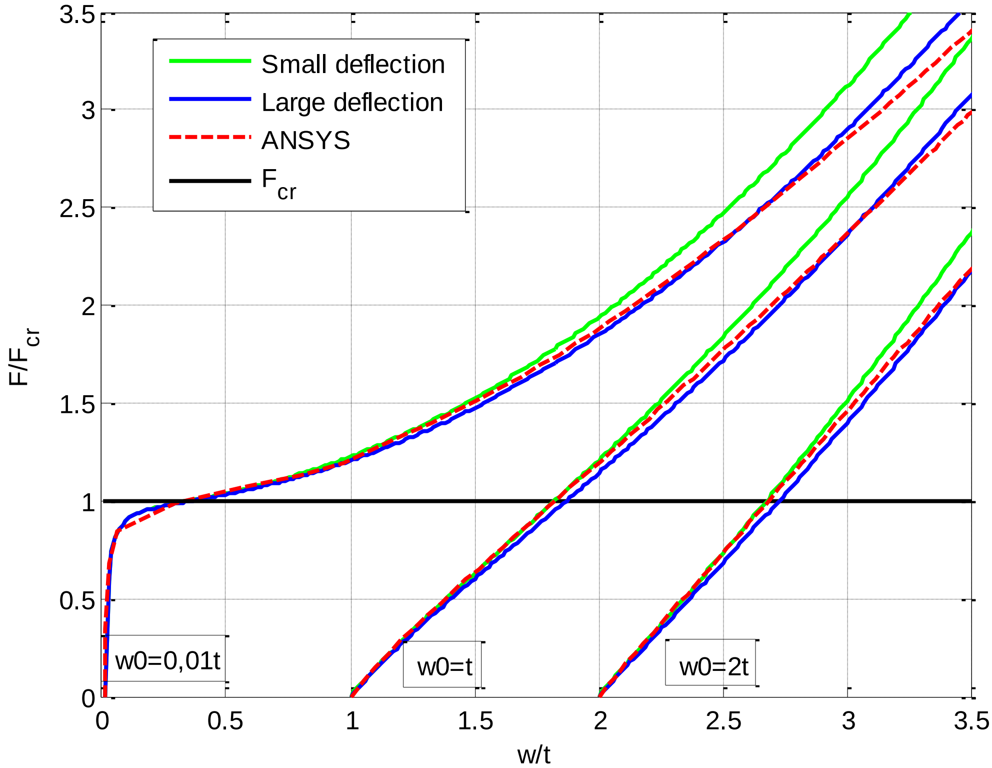

Figure 7-3: Load deflection curves for the theories and with different imperfections

As one would expect, the solution assuming small deflections give the most inaccurate results. Nevertheless, these deviations only reach a significant level at approximately 2 times the critical load at low imperfections and 1.5 times the critical load at higher imperfections. This matches well with expectations as the higher imperfection causes larger deflections which conflict with the assumption of small deflections.

The large deflection fares much better and yield accurate results up to as much as 3 times the critical load, nonetheless it still ends up deviating from the Finite Element results.

In conclusion the proposed method yields good results, and since loads higher than 3 times the critical load is unlikely to happen in most scenarios, the results are sufficiently accurate. However it still contains the major drawback of being reliant on the coefficients which are, as mentioned earlier, completely dependent on the boundary conditions of the plate. As the coefficient would have to be derived again for each new set of boundary conditions it will be challenging to establish a general formulation that at least take geometric variations into account.

7.2 Ferreira & Virtuoso

The paper made by Ferreira & Virtuoso introduces a semi analytical method to solve the case of a simple supported plate with uniaxial compression. The method includes solutions to the Airy stress function that satisfies Marguerre's equations for not only the case of isotropic plates, but also orthotropic plates.

The constitutive relation applied is linear elasticity, though the constitutive matrix varies depending on whether the material is isotropic or orthotropic.

The general procedure is sketched in Figure 7-4, where the out of plane displacements are written as double Fourier series.

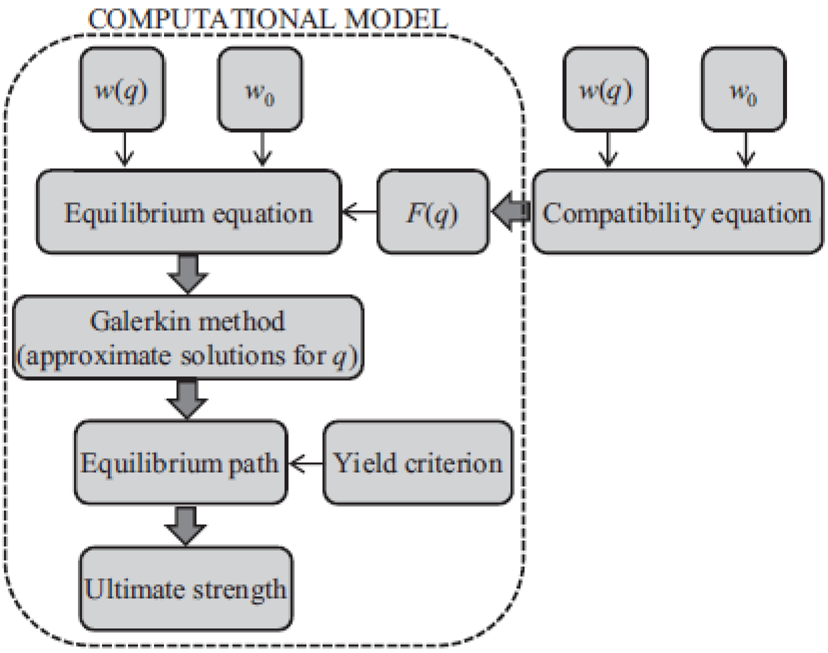

Figure 7-4: Overview of the semi analytical model [L19]

Unlike ROSMANIT & BAKKER, this method is valid for any rectangular plate as long as the plate thickness is constant. This is also highlighted in an example included in the paper with the dimensions shown in Figure 7-5. The example plate is considered to be normal steel with the same material parameters as the example from Chapter 7.1 and with a yield stress of 355 MPa. The initial imperfection is assumed to be $\frac{b}{400} = 4.5mm$.

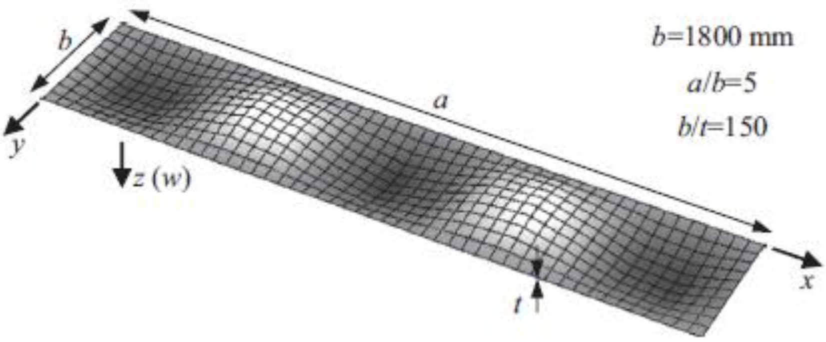

Figure 7-5: Example plate. Figure shows first buckling mode [L19].

By setting the initial imperfection to zero it is possible to obtain critical buckling load and by doing that Ferreira & Virtuoso obtain a critical buckling stress of 33.7MPa. Computing the analytical solution yields a critical buckling stress of 33.74MPa, so there is very little difference between the two results.

Doing a nonlinear buckling analysis gives the load deflection curves shown in Figure 7-6, where the results are normalized with respect to the yield stress and plate thickness.

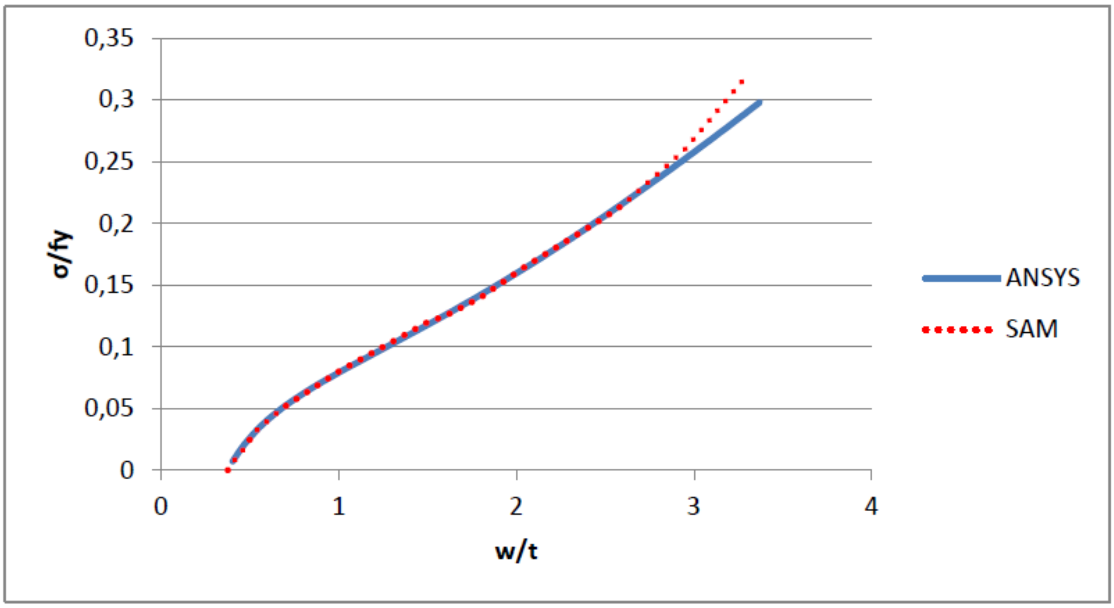

Figure 7-6: Comparison of post buckling behavior. SAM=Semi Analytical Method

The semi analytical method matches well until the average compressive stress reaches 25 % of the yield stress which is $0.25 \cdot 355MPa = 88.75MPa$. This stress is approximately 2.6 times the critical buckling stress and is a comparable level of accuracy to the modified large deflection method proposed by ROSMANIT & BAKKER. This similarity may be because they share the same large deflection theory as their foundation.

The method can be also be used to determine the post critical bearing capacity as all in plane normal and shear stresses are known. The post critical bearing capacity is defined as the load where the plate starts to yield so the Von Mise yield criterion is used to determine it:

$$\sigma_v = \sqrt{(\sigma_x)^2 + (\sigma_y)^2 - \sigma_x\sigma_y + (\tau_{xy})^2} \tag{7-5}$$

For the example, the post critical bearing capacity is found to be 115 MPa using the semi analytical method combined with the Von Mise yield criterion.

Doing a nonlinear buckling analysis with bilinear isotropic hardening included yields a post critical bearing capacity of $2.457*10^6$N.

The corresponding stress is $\frac{2.357 \cdot 10^6 N}{1800mm \cdot 12mm} = 113.75MPa$. They are seen to be in very good alignment.

For completeness sake, the post critical bearing capacity from the Eurocode approach is included as well. This results in a post critical bearing capacity of $2.204*10^6$N.

The corresponding stress is $\frac{2.204 \cdot 10^6 N}{1800mm \cdot 12mm} = 102.02MPa$.

It is seen to yield lower results than the ANSYS model, which is in alignment with the results from Chapter 3.3 considering that the example plate is a very slender plate with the nondimensional slenderness given by:

$$\lambda = \sqrt{\frac{f_y}{\sigma_{cr}}} = \sqrt{\frac{355MPa}{33.74MPa}} = 3.244$$

According to Figure 3-26, a slenderness of this level yields a bearing capacity that is approximately 10% lower than the Finite Element model.

7.3 Other solutions to the static post buckling case

In 2002 Byklum & Amdahl [L20] proposed a computational model to calculate the post buckling of stiffened and unstiffened rectangular panels. Like Ferreira & Virtuoso, the solution proposed also uses Airy's stress function combined with Marguerre's equations, linear elasticity and large deflection theory as a foundation. Additionally the deflection function for the simply supported case is also described using a double Fourier series.

One of the unique features of the method is the approach to the loading. A piecewise load path with linear pieces is applied in order to reduce to number of load parameters to one. This gives the following expression for the external loads:

$$P_i(\Lambda) = P_i^{(s-1)} + \Lambda\left[P_i^{(s)} - P_i^{(s-1)}\right] \tag{7-6}$$

Where Λ is the load parameter

One of the strengths of the method is that it can simulate behavior like passing limit points and turning points. This is illustrated in an example where a simply supported rectangular plate is subjected to uniaxial compression. The resulting equilibrium path is shown in Figure 7-7.

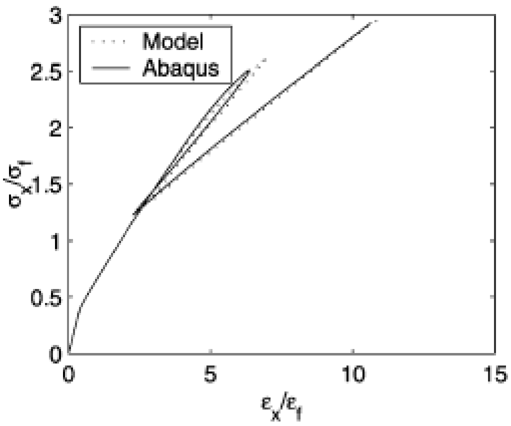

Figure 7-7: Results for equilibrium paths with snap-back from [L20]

Here it can be seen that the equilibrium path makes a sudden change at a certain load level. This is the snap-back phenomena were the buckling suddenly snaps from one mode to another. It can be provoked by giving an initial imperfection that is significantly different from the expected buckling mode, which will eventually lead to the plate forcefully snapping into the proper buckling mode. This phenomenon happens at very high load levels, with the example having it occur at around 2.5 times the yield stress, so it does not have much practical relevance. It is however a good example of the methods ability to simulate unstable phenomena.

Another method of interest is a two-strip model proposed by Bakker & Rosmanit & Hofmeyer [L21] that can be used to describe simply supported rectangular plates with uni- or biaxial compressive forces. Using the same large deflection theoretical assumptions as the previous models the authors found that the results are comparable to other analytical solutions.

7.4 Solutions to the dynamic post buckling case

In 2000, Petry & Fahlbusch [L22] proposed a solution method aimed at establishing a model for simulating the dynamic buckling of a rectangular plate exposed to an impulse load. In this context, the concept of a dynamic load factor (DLF) was used. In classical literature the DLF has typically been defined as the relation between the critical buckling load and the impulse amplitude of the failure load:

$$DLF_{crit} = \frac{N_F^{dyn}}{N_{crit}} \tag{7-7}$$

In their paper Petry & Fahlbusch suggests an alternate definition of the DLF, where the dynamic load is then compared to the static failure load as the loading capacity can be several times that of the critical buckling load:

$$DLF = \frac{N_F^{dyn}}{N_F^{stat}} \tag{7-8}$$

Through the application of classical elastic large deflection plate theory they establish the following equation of motion [L22]:

$$\rho h \ddot{w} = N_x \frac{\partial^2 w}{\partial x^2} + N_y \frac{\partial^2 w}{\partial y^2} + 2N_{xy} \frac{\partial^2 w}{\partial x \partial y} - K(\Delta\Delta w - \Delta\Delta w_o) + q_z \tag{7-9}$$

Where

w is the out of plane displacement

N_x, N_y and N_{xy} are the external loads as illustrated on FIG b)

K is the flexural rigidity

Δ is the Laplacian operator

q_z is the surface pressure (ignored in the final solution)

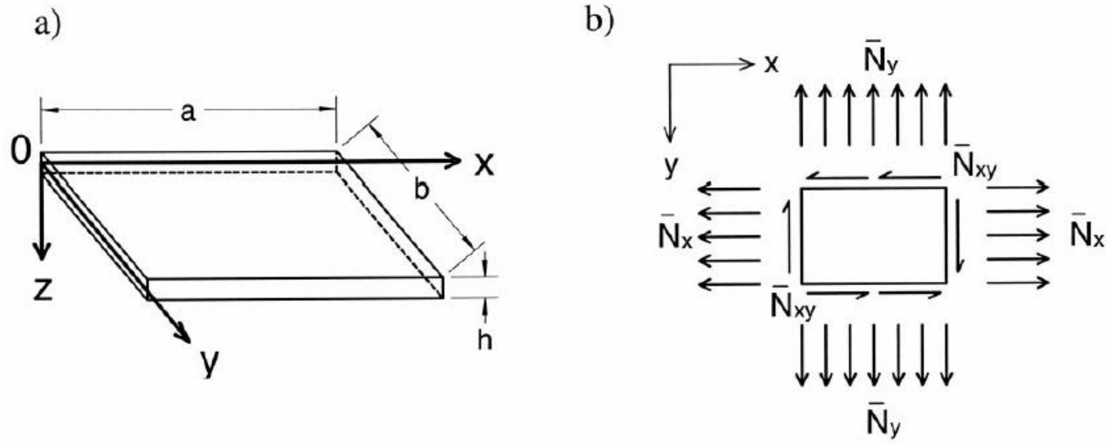

Figure 7-8: (a) Plate dimensions and coordinates; (b) definition of the average membrane forces [L22]

The equation of motion is solved through the usage of double Fourier series, Airy's stress function and numerical integration schemes such as Runge Kutta's 4th order method. By ignoring the acceleration related parts of the equation of motion, the solution becomes capable of modeling the static post buckling behavior, though the authors do not show any examples of this possibility.

Another possible method that can emulate elastic dynamic buckling comes from Lodz University of Technology in Poland [L23]. This method can give critical loads, natural frequencies, post buckling behavior and dynamic buckling. Using large deflection theory it can simulate the behavior of one of more plates with static or impulse loads. It is also capable of modeling orthotropic materials [L24], but it still limited to elastic material behavior. Figure 7-9 illustrates two adjacent plates.

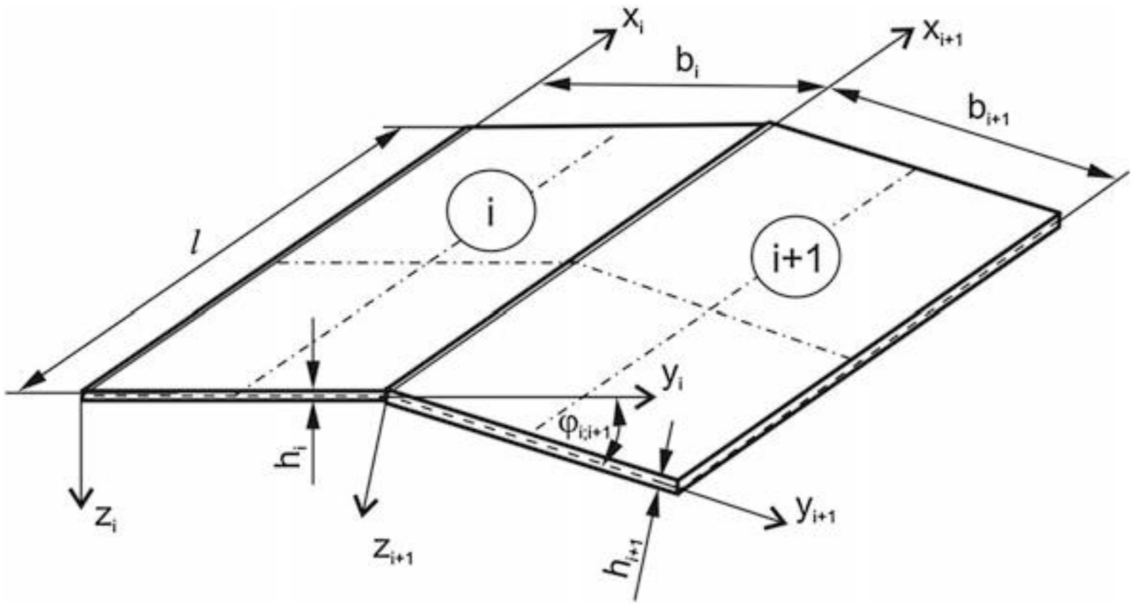

Figure 7-9: Geometrical dimensions and local coordinates for adjacent plates

Using this theory they get the following equation for the post buckling case:

$$\left(1-\frac{\lambda}{\lambda_s}\right)\xi_s + a_{ijs}\xi_i\xi_j + b_{ssss}\xi_s^3 = \frac{\lambda}{\lambda_s}\xi_s^*; \quad (s = 1, \ldots., N) \tag{7-10}$$

Where

λ is the load factor

λ_s is the critical load factor

ξ is the unknown displacement

a_{ijs} and b_{sss} are coefficient describing the boundary conditions

ξ^* is the initial imperfection

The corresponding equation of motion is the same but with an acceleration term timed with the inverse of the natural frequency squared.

$$\frac{1}{\omega_s^2}\ddot{\xi} + \left(1-\frac{\lambda}{\lambda_s}\right)\xi_s + a_{ijs}\xi_i\xi_j + b_{ssss}\xi_s^3 = \frac{\lambda}{\lambda_s}\xi_s^*; \quad (s = 1,2, \ldots., N) \tag{7-11}$$

This difference is identical to the one in the method proposed by Petry & Fahlbusch where the static post buckling behavior could also be obtained by neglecting the acceleration term.

In [L23], an example is made with a quadratic plate that is simply supported and exposed to uniaxial compression as a sinusoidal impulse load. In this example their numerical analytical method (MAN) is compared to a Finite Element model and the Petry-Fahlbusch model.

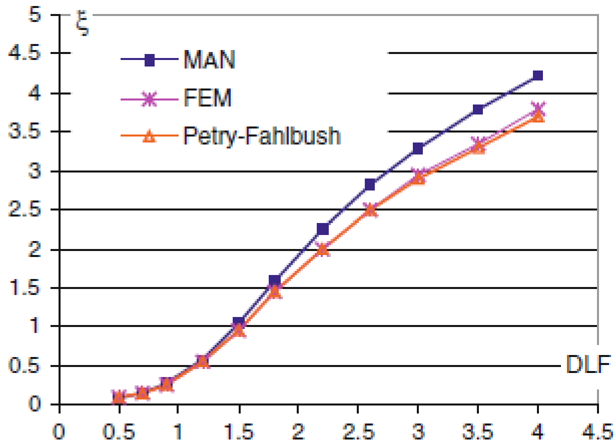

Figure 7-10: Comparison of dynamic buckling for quadratic plate in uniaxial compression.

The results are depicted in Figure 7-10, where DLF is the dynamic load factor, which in this case is defined as the ratio between the impulse amplitude and the critical load. The value ξ is the out of plane displacement normalized by the plate thickness.

Here it can be seen that the Petry-Fahlbusch model matches very well with Finite Element results, while the numerical method only matches decently. It deviates at higher load levels but otherwise keep the same general behavior as the Finite Element results. The author speculates that the discrepancy compared to the Petry-Fahlbusch model comes from the factor that they use a relatively large number of terms in the Fourier series.

The numerical method has been tested in other papers such as Kubiak [L25], where a series of plates are modeled together to create a beam with an open cross section exposed to compression. Here, the author found that the numerical method and Finite Element method matched well.

7.5 Partial conclusion

Different methods for static and dynamic postbuckling behavior of flat plates with initial imperfections have been reviewed. All methods have been found to be comparable to Finite Element results for loads up to two times the critical load. The method proposed by Petry & Fahlbusch stands out as it matches Finite Element results up to four times the critical load. The method discussed by Kubiak, can potentially reach the same levels of accuracy if it includes longer Fourier series.

Kubiak's method in particular ought to be investigated further as it includes the possibility of connecting multiple plates together to create more complex structures. By using this feature it can be used to construct thin-walled beam structures and systems of plates. Because of this, it ought to be investigated how accurate the method is for increasingly complex plated structures.

8 CONCLUSION

This thesis has investigated the structural response of offshore structures subjected to accidental explosion loads. This has been done by introducing two simple models that are representative of relevant load conditions and supports on an offshore module. These two models are a simply supported plate subjected to uniaxial compressive forces and a simply supported beam subjected to an evenly distributed impulse load. Both models has been made in the commercial Finite Element software ANSYS.

The plate model has been researched in regards to the local buckling response arising from the compressive forces, while the beam has been analyzed for the development of local strain and the combined dynamic response of plasticity, lateral buckling and strain rate effects.

It has been found that for local strain development in I-profile beams, there are differences between models modeled with shell elements and models modeled with solid elements. This difference was found to be roughly 10 %. A method for conversion introduced in a former paper on the subject, to establish convergence in a shell element model and plastic strain comparable to solid element models, has been tested and found to be incapable of achieving reliable results.

Transient analyses of the I-profile subjected to a linearized triangular impulse load were carried out with a pressure level that induced plasticity, where the response was for different combinations of elasticity, plasticity and imperfections. It was found that including plasticity in the response increase the midspan response magnitude significantly while adding imperfections, which enables lateral buckling to occur, to the elastic model increased the response by similar amounts. Combining plasticity and lateral buckling gave a response many times larger than the linear elastic response, highlighting the differences these phenomena cause.

These analyses were also implemented in the explicit solver, ANSYS LS-DYNA, which is a subset of ANSYS, and it was found that it could achieve comparable results to the implicit solver while drastically reducing computation time.

Using the ANSYS LS-DYNA module, analyses including the Cowper-Symonds strain rate model were made to measure the influence of strain rate effects on the maximum response. It was found that because the strain rate effects effectively increase the yield stress, the effects of plasticity were greatly reduced and the response of full nonlinear model was almost halved. A modified plasticity model was introduced, were strain rate effects were included by an increase of the initial yield stress based on hand calculations, and the response of this model was found to be comparable to the full strain rate model as long as the load levels remained within reasonable limits.

A number of methods for modeling post buckling behavior were reviewed, and it was found that though some had practical limitations, like being only valid for quadratic plates, they all showed good agreement with results generated by the plate model setup in ANSYS. Additionally methods capable of simulating dynamic buckling as well were also reviewed and matched well with ANSYS, though one showed divergence in results at loads above 2 times the critical load. Common for all the methods, both static and dynamic, was that none demonstrated the capability to model plasticity, although some were capable of sufficiently predict the post critical bearing capacity.

8.1 Further work

In this thesis, an I-profile with equal width and height was used for analyses of the local plastic strain. As discussed in Chapter 6.2, this may not match entirely with assumptions made in standard approaches to the plastic hinge length. Because of this, it ought to be investigated whether the results remain the same for profiles with different height to width ratios, or if numerical results end up more in alignment with hand calculations.

Other aspects that could have merit in researching, is the usage of different hardening models. Standards make no mention of specific hardening models in the context of their approaches to plastic strain calculation. In the current thesis only a bilinear isotropic hardening model has been used, but it could be compared to other common models like kinematic hardening or multilinear hardening models.

Lastly, the implementation of 'element death' ought to be investigated and compared to Finite Element models without. Element death is the act of deactivating an element in the mesh when it reaches a certain limit like an ultimate plastic strain, and then continue calculations without it. A variant also exist for shell elements, where instead of removing entire elements, instead a single layer of the shell element is removed. With this feature, gradual rupture of the structure can be simulated.

All these suggestions for further work on the development of plastic strain also ought to looked into for the dynamic case. In particular, the finite element modeling such as plastic hinge development and element death is of interest in the dynamic case. Making the loading dynamic allows for the implementation of the strain rate effects into these considerations and their effects on the plastic strains.

In this study a number of solutions to the static post buckling behavior have been reviewed, so a next step would be to implement one of them in a programming language like Matlab. From there on, possibilities for implementing a solution so that it can work together with existing plate formulations so a level of standardization can be achieved. One solution that is particularly interesting in this regard is the method used in Lodz University of Technology which can simulate both static and dynamic buckling behavior. What makes this method worthwhile to investigate further is its ability to piece together a series of plates to create a more complex structure like thin-walled beam.

Also of interest is looking into upgrading one or more of the methods, so that they also can simulate nonlinear material behavior such as plasticity. If that is possible the method with plasticity ought to be subjected to the same local plastic strain investigations as the Finite Element method has earlier in this thesis and other works.

9 REFERENCES

Literature

[L1] B. Bonnerup, B. C. Jensen; Stålkonstruktioner efter DS/EN 1993; Nyt Teknisk Forlag; 1. udgave; 2009

[L2] DS/EN Eurocode 1993-1-1, General rules and rules for building, 2009

[L3] DS/EN Eurocode 1993-1-5, Plated structural elements, 2009

[L4] COWI consult; Guidelines for structural design against dropped objects; Rev. 3; 1993-11-16

[L5] RONJA manual, Section 6, Plastic Deformations and strains; ver. 4.2

[L6] Standards Norway; NORSOK N-004; rev 2; 2004-10

[L7] DNV-RP-C204, Design against accidental load, October 2010

[L8] DNV-RP-C208, Determination of structural capacity by non-linear FE methods, June 2013

[L9] DNV, SINTEF, BOMEL; ULTIGUIDE; 1999-04

[L10] MAERSK; General Jacket Design and Re-assessment Conditions; rev 1.3; 2000-07-25

[L11] Hans Jákup Hansen; Offshore Structures Response on Blast Loads; M.Sc. Thesis, AAUE; 2002-06.

[L12] ANSYS Help, Version 15.0

[L13] Plastic Strain Study, Internal Rambøll Report, Doc. No. 340.001, Rev A, dated 2009-08-21

[L14] Plasticity in beams exposed to explosions, Internal Rambøll Report, Doc. No. 340.002, Rev A, dated 2009-04-24

[L15] Timoshenko & Gere, Theory of elastic stability, Second Edition, 1961

[L16] M.J.M Van de Burg, Plate buckling in design codes, TU Delft, 2011

[L17] D.G. Williams; A.C Walker, Explicit solutions for the design of initially deformed plates subject to compression, Proc. Instn Civ. Engrs. Part 2, pages 763-787, 1975

[L18] Miroslav ROSMANIT; Monique C.M. BAKKER, Elastic post-buckling behavior of uniformly compressed plates, Tecknické university Ostrava, 2008

[L19] Pedro Salvado Ferreira; Francisco B.E. Virtuoso, Semi-analytical models for the post-buckling analysis and ultimate strength prediction of isotropic and orthotropic plates under uniaxial compression with the unloaded edges free from stresses, University of Lisbon, April 2014

[L20] Eirik Byklum; Jørgen Amdahl, A simplified method for elastic large deflection analysis of plates and stiffened panels due to local buckling, Norwegian University of Science and Technology, May 2002

[L21] M.C.M. Bakker; M. Rosmanit, H. Hofmeyer, Elastic post-buckling analysis of compressed plates using a two-strip model, Technische Universiteit Eindhoven, April 2007

[L22] D. Petry; G. Fahlbusch, Dynamic buckling of thin isotropic plates subjected to in-plane impact, Universität Bundeswehr München, August 2000

[L23] Tomasz Kubiak, Static and Dynamic Buckling of Thin-Walled Plate Structures, Lodz University of Technology, 2013

[L24] Tomasz Kubiak, Dynamic buckling of thin-walled composite plates with varying widthwise material properties , Lodz University of Technology, 2005

[L25] Tomasz Kubiak, Estimation of dynamic buckling for composite columns with open cross-section , Lodz University of Technology, July 2011

Websites

[W1] http://911debunkers.blogspot.dk/2011/06/other-collapses-in-perspective_04.html

[W2] http://www.steelconstruction.info/Design_of_beams_in_composite_bridges

[W3] https://support.ansys.com/AnsysCustomerPortal/en_us/Downloads/Extension+Library/15.0+ACT+Library/Workbench+LS-DYNA_R150_v2

[W4] http://www.substech.com/dokuwiki/doku.php?id=fracture_toughness